True Muonium on the Light Front

by

Henry Lamm

A Dissertation Presented in Partial Fulfillment
of the Requirements for the Degree
Doctor of Philosophy

Approved March 2016 by the
Graduate Supervisory Committee:

Richard Lebed, Chair
Andrei Belitsky
Ricardo Alarcon
Damien Easson

ARIZONA STATE UNIVERSITY

May 2016

ABSTRACT

The muon problem of flavor physics presents a rich opportunity to study beyond standard model physics. The as yet undiscovered bound state $(\mu^+\mu^-)$, called true muonium, presents a unique opportunity to investigate the muon problem. The near-future experimental searches for true muonium will produce it relativistically, preventing the easy application of non-relativistic quantum mechanics. In this thesis, quantum field theory methods based on light-front quantization are used to solve an effective Hamiltonian for true muonium in the Fock space of $|\mu^+\mu^-\rangle$, $|\mu^+\mu^-\gamma\rangle$, $|e^+e^-\rangle$, $|e^+e^-\gamma\rangle$, $|\tau^+\tau^-\rangle$, and $|\tau^+\tau^-\gamma\rangle$. To facilitate these calculations a new parallel code, True Muonium Solver With Front-Form Techniques (TMSWIFT), has been developed. Using this code, numerical results for the wave functions, energy levels, and decay constants of true muonium have been obtained for a range of coupling constants α. Work is also presented for deriving the effective interaction arising from the $|\gamma\gamma\rangle$ sector's inclusion into the model.

To Bernadine Samson:

I have never found the right combination of words to express how indebted I am,

so perhaps the sheer volume of this tome can serve as a beginning.

ACKNOWLEDGMENTS

Nothing could ever repay you for your endless accommodation of my pointless digresses, wild misunderstandings of basic physics, and my insane propositions.

Oh Nadia Zatsepin, you define polymath. The combination of brutal honesty and classiness that you embody is without rival.

To Subir Sabharwal, the truly humbling experience of meeting an intellect of your caliber gave me a profound perspective on my own limitations and the value of rigor.

Jeff Hyde, I must testify that I am incapable of being as thoughtful and judicious in my words as you, but everyday I aspire to it.

For Francis Duplessis, your adjudication of utility and meaningfulness in topics always brought clarity to my meanderings.

No one represents to me the creed of "Grind until you get it" as much as Yao Ji. Your intensity of focus and mathematical skill is a model for any physicist.

Russell TerBeek, should the world ever fall into chaos, I know your encyclopedic knowledge with be form the basis of a new renaissance.

Fy ffrind, Owen Littlejohns. Where you find the limitless energy to work and play so hard motivates me to leave my office chair.

Learning that the loudest voice (especially my own) need not be correct one isn't easy, but I thank Lauren Ice for trying everyday to teach that lesson.

Bryce Fielding Davis, there is little about you I know as fact, but this I do: never has a moment with you been dull.

Last but not least, Elizabeth Lee. Your confidence and optimism that with hard work all of one's dreams are attainable comforted me in times of uncertainty.

TABLE OF CONTENTS

LIST OF TABLES

LIST OF FIGURES

Chapter 1

INTRODUCTION AND MOTIVATION: CREATING A LAMPPOST

1.1 The Muon Problem

Flavor physics has a *muon problem.* Several muon observables disagree to varying
levels with Standard Model calculations. Despite these experimental anomalies, the
theoretical paradigm that best describes the muon has been, "Who ordered that?"
This sentiment, expressed by I.I. Rabi, reflects the principle that besides their cou-
pling to the Higgs boson (which determines their mass and lifetime), charged leptons
in the Standard Model interact identically. This long-standing assumption is referred
to as *lepton universality* [1] . Aside from the neutrino sector, the first crack in lepton
universality was the experimental measurement of the anomalous magnetic moment
of the muon, $a_\mu = (g-2)_\mu$[4], which differed from the theoretical result by $\approx 2\sigma$. A re-
fined result from the E821 experiment in 2006 decreased the experimental uncertainty
further [5] but increased the discrepancy with theory. Meanwhile, improvements in
the hadronic sector have reduced the theoretical uncertainty but the anomaly per-
sists [6, 7, 8]. The current theoretical and experimental state of the a_μ anomaly is
well-reviewed by Blum et al. in [9]. Minor theoretical improvements have occurred
since then, and the current discrepancy is[5, 10]:

$$\Delta a_\mu = a_{\mu,\text{exp}} - a_{\mu,\text{theor}} = 288(63)(49) \times 10^{-11}, \tag{1.1}$$

---

[1]Deep down, theorists understand that lepton universality isn't the final word because massive
neutrino lead to incredibly small loop-suppressed effects. The important point is that the Standard
Model assumes lepton universality, so any breaking (including the known neutrino effects) must
come from beyond it

where the first error is experimental and the second is theoretical, and is dominated by the hadronic contributions. Upcoming experiments beginning in 2017 at Fermilab and J-PARC intend to decrease the uncertainty in the experimental results by at least a factor of 4[11]. A persisting discrepancy could be as large as 4σ. Further reduction in theoretical uncertainty is also likely to come from lattice calculations, which could push the anomaly to 5σ. In the years since the a_μ measurements, a number of beyond standard model (BSM) solutions have been proposed and constrained by both spectroscopic and high-energy experiments[12, 13, 14].

Concurrently with this anomaly, there was a desire to improve upon the existing measurements of the proton charge radius, r_P. From several electronic experiments, the value was $r_{P,\text{CODATA}} = 0.8758(77)$ fm[15]. Under these auspices, a more precise measurement of the proton charge radius was undertaken by the CREMA collaboration at PSI by studying the Lamb shift, the $2p - 2s$ splitting, of muonic hydrogen (μH). The larger mass of the muon ($m_\mu = 105.6583715 \pm 0.0000035$ MeV) implied that any mass-dependent energy shifts like the nuclear corrections would be enhanced in a muonic systems by the factor $m_\mu/m_e \approx 207$. CREMA measured the proton charge radius more precisely by a factor of 10. The result was, to everyone's surprise, 4% smaller than the previous CODATA average using all electronic experiments: $r_{P,\mu P} = 0.84087(39)$ [16, 17].

A persistent search for a Standard Model explanation of this discrepancy has so far failed, leading to a number of BSM solutions [18, 19, 20, 20, 21, 22, 23, 24, 25, 26, 27, 14, 28, 29, 30, 31, 32, 33] where the a_μ anomaly is often a critical co-constraint on models. Near-term experiments are planned to investigate sources of this discrepancy [34]. Improved measurements of electron-proton scattering and hydrogen spectroscopy will decrease the uncertainty in the CODATA result. In the muonic sector, experiments will measure the Lamb shift of muonic deuterium and helium,

which provide critical data on nuclear effects. Finally, muon-proton scattering will be performed to provide full complementarity between the muonic and electronic observables.

Since any BSM resolution to the muon problem will require modifications to the Standard Model at high energies, new anomalies and measurements observed at the LHC in the muonic sector[35, 36] must be taken into account. The consensus view of the muon problem can perhaps best be summarized, "troubling, but not definitive" signs of cracks in the Standard Model. A definitive resolution to the muon problem will require not just looking, as the old adage goes, under the lamppost, but will necessitate creating new lampposts. One such lamppost being "built" is true muonium.

1.2   True Muonium

Given the surprises already found, it is time to reconsider other potential observables in the muonic sector. A particularly strong candidate for shedding light on the muon problem is the bound state $(\mu^+\mu^-)$, called "true muonium"[37]. Other bound states have limited new-physics reach due to small reduced masses $\mu \approx m_e$ ($e\bar{e}, eH, e\bar{\mu}$) or nuclear-structure uncertainties ($eH, \mu H$). In contrast, true muonium's $\mu = m_\mu/2$ and leptonic nature make this heavier sibling of positronium an ideal probe, through the Lamb shift or hyperfine splitting[18, 3, 38, 33]. Muonic observables like a_μ or the Lamb shift of (μP) are limited in their BSM reach because they can only probe certain new physics operators at leading order. In contrast, measurements in true muonium are affected by most new physics scenarios. This fact occurs by virtue of the annihilation channel, where normally suppressed operators in the exchange channel can contribute at leading order.

Beyond spectroscopy, measuring rare decays would also constrain new physics.

The leading-order SM decay rate of the 1^3S_1 state to mono-energetic muon neutrinos is known to be $\Gamma(1^3S_1 \to \nu_\mu \bar{\nu}_\mu) \approx 10^{-11}\Gamma_{e^+e^-}$. While this rate is small, it is within the realm of detected rare processes in mesonic decays, due to the $\propto m_\ell^5$ scaling. Related to the measurement of neutrino decays is the larger subject of invisible decays. For positronium, Badertscher et al. have shown that strong constraints on a variety of BSM (e.g. extra dimensions, axions, mirror matter, fractional charges, and other low-mass dark matter models) can be made[39]. In true muonium, these rates are all enhanced due to mass scaling and therefore better constraints are possible with lower statistics.

To date, though, true muonium has not been directly observed. The non-trivial technical difficulties lies in creating coincident low-energy muon pairs and detecting the atom during its short lifetime ($\tau \approx 1$ ps) [2] . Not withstanding these problems, numerous proposed methods of production have been discussed over the years [40, 41, 42, 43, 44, 45, 46, 47, 48, 49].

These considerations have motivated the Heavy Photon Search (HPS)[50] experiment to search for true muonium beginning in 2016[48]. The DImeson Relativistic Atom Complex (DIRAC) [51] has discussed the possibility of its observation in an upgraded run[52] where further statistics could be used extract its Lamb shift[53]. In the longer term, the intention of Fermilab to develop a muon facility for neutrino physics as well as a test bed for a future muon-muon collider presents an opportunity for high-precision measurements of true muonium.

---

[2]The difficulty in producing low energy muons is two-fold: the muon's weak decay lifetime ($\tau \approx 2.2\mu$s) quickly degrades the beam's muon flux. Further complicating production is that for a given energy, the pion cross-section is much larger than then muon due both to its lower mass ($m_\pi = 135$ MeV and its larger coupling ($\alpha_{QCD} \approx 0.3$).

1.3 The Light Front

At least in the short term, any detection will involve relativistic true muonium. An accurate treatment is complicated because defining wave functions in standard quantum field theory are difficult and are not boost invariant. Consequently, prediction of the production and decay rates of true muonium are based on the non-relativistic wave functions, which introduces uncertainties. Reducing these uncertainty and improving computation methods for non-perturbative wave functions of true muonium directly from quantum field theory are the motivation for this thesis. In non-relativistic quantum mechanics (NRQM), there is a straight forward way to compute the bound-state spectrum and wave functions, by computing the eigenstates of the Hamiltonian. Phenomenological considerations have inspired non-relativistic potential models, which are used for the heavy quarkonium[54, 55, 56, 57]. Alas, for strongly-coupled systems, deriving a potential is often impossible, and further complicating the matter is that potentials lose their meaning in a relativistic theory. A number of systems exist where consideration of these problems is required: light-quark bound states, positronium, and our main concern here: relativistic true muonium.

For these systems, relativistic and non-perturbative methods are necessary. There are existing covariant methods: lattice gauge field theory[58, 59, 60, 61, 62, 63, 64, 65, 66, 67], Dyson-Schwinger[68, 69, 70, 71, 72] and Bethe-Salpeter equations[73, 74, 75, 76, 77, 78], and non-relativistic effective-field theory[79, 80]. While these methods are covariant, the Hamiltonian operator in textbook quantum field theory is given by $H = \sqrt{P^2 + M^2}$. This non-analytic nature affects each of these methods. Lattice field theory relies upon extracting the states from long-time operator correlations and therefore has difficulty determining the predictions of QCD bound states[81, 82, 83]. This issue is particularly noticable in the exotic sector, where lattice QCD has yet to

5

definitively explain the XYZ states[84]. Lattice gauge theory's reliance upon Monte Carlo methods also lead to numerical complications at small quark mass m_q[85, 86], and extracting wave functions is highly non-trivial[87]. Dyson-Schwinger and Bethe-Salpeter equations run into difficulties from gauge invariance[88], two-time issues[89], and obtaining the correct non-relativistic limit[90]. Effective field-theory methods require the matching of perturbative expansions and therefore miss important non-perturbative effects. Most troubling, the vacuum of any quantum field theory in the instant form is complicated by creating and annihilation of virtual particles, implying that the particle number of a state is not conserved. In strongly-coupled theories like QCD, this complicated vacuum is a major impediment to understanding confinement[91].

Instead of following the textbook quantization on a fixed time slice $t = 0$, quantizing with respect to light-front time $x^+ \equiv t + z$ (called *front form*) [92] allows one to develop a Hamiltonian formalism [2], where an analogue of the Schrödinger equation for the eigenstates becomes an infinite but denumerable set of coupled integral equations. The infinite set arises from the need to sum over all Fock states, which can be defined in front-form field theory. An additional feature of using the front-form is that the wave functions are boost-invariant. This trait makes the front-form the ideal technique for computing relativistic true muonium. In order to obtain numerical results, one may then truncate the equations by limiting the set of component Fock states included in the calculation and discretizing momenta, turning the problem into a finite one solvable on a computer, which is called Discretized Light-Cone Quantization (DLCQ) [93]. With DLCQ, it is possible to compute the entire spectrum of a strongly-coupled quantum field theory in the non-perturbative regime. In this thesis will be presented some results for strongly-coupled QED ($\alpha > \alpha_{QED} \approx 1/137$) with multiple flavors.

6

1.4   Outline of the Present Work

This work is structured as follows. Chapter 2 begins with an overview of quantum field theory on the light front. In Chapter 3, the model of true muonium used in calculations is presented. Treatment of divergences and regularization of the model are discussed. These improvements on [1, 94, 95] have allowed for the infinite limit to be taken for the first time. In Chapter 4 energy spectra and decay constant results for the true muonium model are presented that can be measured at future experiments. Analytical work in deriving the $|\gamma\gamma\rangle$ effective interaction is shown in Chapter 5. The work is concluded in Chapter 6 with a summary and remarks about the future.

Chapter 2

QUANTUM FIELD THEORY ON THE LIGHT FRONT

2.1   Historical Development of Light Front Field Theory

Non-relativistic quantum mechanics is Galilean invariant. This symmetry has the
interesting property that only one *initial surface* [1] can be defined for a theory, the
surface $x^0 = t = 0$. This constraint implies that only a single decomposition of the
Galilean generators into *kinematical* and *dynamical* generators exists. A kinematical
generator is one that leaves the state invariant, while a dynamical one alters the state.
In the case of non-relativistic quantum mechanics, the set of 3 translations and 6 ro-
tations leaves the state unchanged, while the remaining operator, the Hamiltonian–by
definition is the generator of time translation– is dynamical. Obviously, in a relativis-
tic theory, this separation of the temporal generator from the spatial generators isn't
so simple.

  Relativistic theories are invariant under the Poincaré group. Enforcing relativistic
causality decreases the family of world lines that can exist, and therefore the number
of initial surfaces possible is increased. Dirac[92] was the first to point out that there
are several classes of inequivalent initial surfaces. He further showed that different
initial surfaces have different numbers of kinematical generators. The three surfaces
Dirac discussed were (1) the standard instant form ($x^0 = 0$), (2) the point form
($x^\mu x_\mu = a^2 > 0$) whose surface is a hyperboloid, and of greatest interest to us here,
(3) the front form ($x^0 - x^3 = 0$), whose surface is the light cone $x^\mu x_\mu = 0$. Beyond
these three, it was eventually shown that only two other classes of surfaces exist: (4)

---

[1]An *initial surface* is a surface that intersects each world line once and only once

another hyperboloid with $x_0^2 - x_1^2 - x_2^2 = a^2 > 0$ and (5) $x_0^2 - x_3^2 = a^2 > 0$[96]. The instant-form and point-form both have six kinematical generators, while forms (4) and (5) have only four kinematical generators. The front-form is unique in having the maximal number of kinematic generators, seven. This property is the first of a number of novel features that suggests that front-form physics may be more tractable to relativistic bound-state physics when a Hamiltonian method is preferred.

Although Hamiltonian physics forms the basis of textbook NRQM, it was long ago recognized that in instant-form QFT, the use of action-based methods developed by Schwinger[97, 98], Feynman[99, 100, 101, 102], and Tomonaga[103, 104] were better suited for solving problems in which relativistic, perturbative calculations are desired. This led to a seismic shift in physics. At present, though, the question of how best to solve strongly-coupled relativistic problems like hadron structure and relativistic true muonium isn't known. It is with this perspective that many researchers have studied front-form QFT, in hopes that it would lead to a simplification in studying bound systems.

Almost 20 years later, renewed interest in Hamiltonian methods in field theory arose. Weinberg, interested in the *infinite-momentum frame* where a state's momentum component $p_z \to \infty$, discovered in the case of the ϕ^3 theory that creating or annihilating particles from the vacuum was forbidden[105]. This observation would eventually lead to an understanding that the vacuum of a front-form field theory is trivial (i.e. empty of ordinary particles), and that Fock states are well-defined. A few years later, the front-form perturbation theory rules were derived by Kogut and Soper[106]. Because of the inequivalent nature of the instant-form surface and the front-form, it was a crucial, but highly non-trivial, matter to show that the traditional instant-form Feynman rules give equivalent results to those from the front-form rules[107, 108, 109, 110, 111, 112, 113].

9

Perhaps the greatest success so far of the front-form methods has been the development of methods for studying non-Abelian gauge theories. In QCD, these methods have been used to obtain results for exclusive processes by Lepage and Brodsky[114] where equivalent instant-form expressions didn't exist. Analytical results using light-front techniques have also reproduced the correct leading-order Lamb shift and hyperfine splitting for QED bound states[115, 116, 117, 118]. The Yukawa theory has been used to understand the differences between instant-form and front-form approaches and how they can be reconciled[119, 120, 121, 122, 123]. The Standard model has also been formulated in light-front quantization[124].

The greatest promise of using the front form lays in its ability to address non-perturbative field theory. Because a closed-form Hamiltonian can be constructed front-form physics admits a Schrödinger-like equation that can be expressed in an infinite-dimension Fock space. This construction can be used to apply the techniques of non-relativistic quantum mechanics to quantum field theory. To make these problems tractable, the Fock space is truncated to a finite number of states based on particle content. If the Fock states are furthermore discretized in momentum Fourier modes on a lattice, it is called Discretized Light Cone Quantization (DLCQ). This method was pioneered by Pauli and Brodsky, working on 1+1 dimensional Yukawa theory[93].

The special feature of super-renormalizability of field theories in 1+1 has been particularly amendable to DLCQ, and these theories have been investigated in depth. Sawicki used the method to solve scalar QED_{1+1}[125, 126], Harindranath and Vary investigated the structure of the vacuum and bound states of ϕ_{1+1}^3 and ϕ_{1+1}^4 models[127, 128, 129]. Pushing further, Hornbostel et al. presented results for the meson and baryon eigenstates of QCD_{1+1}[130], while Hiller studied more field theoretical properties of the light-front in the Wick-Cutkosky model. The Schwinger model, which ad-

mits analytical solutions in both instant form and front form, was first studied by Eller et al. in 1986[131], and since has become an important testbed for developing improvements that can then be used in other theories[132, 133, 134, 135, 136, 137, 138, 139]. Since DLCQ produces the wave functions and the energy levels, Hiller was able to compute the R-ratio in QED_{1+1}[140]. In one dimension, it has also been applied to solving t'Hooft's model of Large-N QCD[141], adjoint QCD[142, 143, 144], and supersymmetric models[145, 146, 147, 148, 149, 150, 151, 152, 153, 154, 155]. Although spontaneous symmetry breaking is manifested in a distinctly different way, it is also possible to study in DLCQ[156, 157, 158] Finally, research has been undertaken using DLCQ to test Maldecena's AdS/CFT conjecture in 1+1 theories[159, 153].

Extending DLCQ beyond 1+1 dimensions is complicated in two ways: first, higher-dimensional theories require regularization and renormalization. Second, the number of Fock states grows so rapidly that tractable numerical calculations allow only a small number of states to be included. Despite these difficulties, DLCQ was applied first to positronium by Tang et al.[160]. In that work, the effective Hamiltonian matrix equation was derived for a model including only the $|e^+e^-\rangle$ and $|e^+e^-\gamma\rangle$ Fock states. Variational methods were applied to this effective model and produced upper limits on the triplet state. Further developments in understanding the connection between light-front and instant-form techniques were studied by Kaluza and Pauli, reproducing the expected results for the hyperfine splitting and Bohr states in the limit of $\alpha \to 0$[161]. Krautgärtner et al., implementing the *Coulomb counterterm* techniques developed by Wölz[162], solved the effective matrix equation for positronium[163]. They found that it was possible to reproduce the correct Bohr spectrum as well as the leading relativistic hyperfine splitting even for large α. Concerned with the effect of zero modes, Kalloniatis and Pauli undertook numerical simulations based upon perturbative solutions to the zero-mode constraint equations[164].

11

Krautgärtner further developed these techniques and began to analytically study the two-photon exchange interaction and its relationship to the observed divergences in his dissertation[165]. Wölz, in his dissertation, applied DLCQ to QCD by including the $|q\bar{q}gg\rangle$ Fock state[166]. Numerical limitations at the time prevented implementation of the counterterm techniques being concurrently developed, so that slow convergence in the number of discretization points and strong dependence on the momentum cutoff precluded these results from suggesting any conclusive statements. Synthesizing all these techniques, Trittmann computed the first results for positronium with the inclusion of the annihilation $e^+e^- \to \gamma$ channel[1, 94, 95]. Utilizing the good quantum number J_z, he was able to split the problem and investigate the breaking of rotational invariance inherent in light-front form in the effective equation. Cutoff dependence and inadequate computational resources were the major limits to Trittmann's work. This thesis is a direct extension of these methods to the coupled system of true muonium, positronium, and true tauonium.

Beyond DLCQ, other numerical methods have been developed upon the light front. Basis light-front quantization (BLFQ), instead of discretizing the momenta in Fourier modes chooses harmonic oscillator modes in the transverse direction. This method hopes to decrease the number of basis states needed by more accurately representing the wave function. BLFQ has shown initial success in solving bound-state problems in QED[167, 168, 169, 170, 171, 172, 173] and QCD[174]. Using Monte Carlo methods developed for instant-form lattice gauge theory, transverse lattice theory has investigated simple models of QCD in 3+1 dimensions[175, 176, 177, 178]. Tube-based, collinear QCD and other effective Hamiltonian methods also exist[179, 180, 181]. In recent years, the AdS/QCD conjecture has been extended to light-front field theory to produce the low-energy meson and baryon spectra[182, 183, 184, 185, 186, 187, 188, 189, 190, 191].

2.2 Poincaré Generators and Hamiltonian Dynamics

Having discussed the historical developments in light-front quantization, in this section is developed the actual light-front eigenvalue equation. For definitions of this notation, the reader is referred to Appendix A. The Poincaré generators of a theory can be constructed from its stress tensor $T^{\mu\nu}$. On the light front, they are given by the vector P^μ and the tensor $J^{\mu\nu}$ defined by

$$P^\mu = \frac{1}{2}\int \mathrm{d}^2x_\perp \mathrm{d}x^- T^{+\mu}, \quad \text{and} \quad J^{\mu\nu}\frac{1}{2}\int \mathrm{d}^2x_\perp \mathrm{d}x^- (x^\mu T^{+\nu} - x^\nu T^{+\mu}). \tag{2.1}$$

P^μ represent the translations in light-front coordinates, P^- is the (dynamical) generator of time-translations, i.e., the Hamiltonian. The other three translations, P^+, P^i are kinematical generators. The three other kinematical operators correspond to the boosts: one along the longitudinal x^+-direction, $K^+ = -\frac{1}{2}J^{+-}$, and the two along the $\boldsymbol{x}^\perp$ directions, $E^i = -\frac{1}{2}J^{+i}$. The final kinematic operator is the rotation about the x^+ axis, $J^+ = J^{12}$. The remaining two operators, $F^i = J^{-i}$, are dynamical.

Intuitively, the largest change in kinematical symmetries between instant form and front form is that explicit rotational invariance has been traded for explicit boost-invariance. Although the total angular momentum operator J^2 is no longer kinematical, the preservation of kinematical J^+ allows for an angular momentum based classification of states that is useful in bound-state physics.

Formally, P^- is the Hamiltonian of front-form time translations, but for non-perturbative bound-state calculations, researchers have found that the so-called Light-cone Hamiltonian,

$$H_{\mathrm{LC}} = P^- P^+ - \boldsymbol{P}_\perp^2, \tag{2.2}$$

is more useful. Here, $P^+ \equiv P^0 + P^3$ is the longitudinal momentum component conjugate to the light-front longitudinal direction x^-, and the transverse momentum is $\boldsymbol{P}_\perp$. For an eigenvalue M^2 of the operator H_{LC} corresponding to a state $|\Psi\rangle$, the

light-front Hamiltonian eigenvalue equation is not nonanalytic (cf. the instant-form expression $\sqrt{M^2 + \boldsymbol{P}^2}$):

$$P^- \left|\Psi\right\rangle = \frac{M^2 + \boldsymbol{P}_\perp^2}{P^+} \left|\Psi\right\rangle . \tag{2.3}$$

In additional to the P^μ and J_z operators, the total spin operators S^2 and S_z still commute in front form, meaning that a particular state $\left|\Psi\right\rangle$ can be completely specified as

$$\left|\Psi; M, P^+, \boldsymbol{P}_\perp, S^2, S_z; h\right\rangle , \tag{2.4}$$

where h indicates any discrete or non-spacetime quantum numbers, such as parity or lepton number. Splitting the Fock space into subsets based on these discrete quantum numbers will allow for smaller Hamiltonian matrices that are computationally less difficult.

The numerical values of longitudinal momenta P^+ for all physical particles are nonnegative, since $P^0 = E > P^3$. This is the source of the statement that creation of virtual particles traveling "backwards" with respect to the light-front longitudinal direction is prohibited. Therefore, empty space cannot produce collections of virtual particles in front form. The dramatic implication is that the ground state of the free theory is also the ground state of the full interacting theory up to *zero modes* (field configurations with $P^+ = 0$, and the Fock-state expansion built upon the free vacuum provides a rigorous "parton" component description of the full interacting state.

Expressing the state $\left|\Psi\right\rangle$ in terms of its Fock components $\left|\mu_n\right\rangle$, where n in general is denumerably infinite. Each particular component $\left|\mu_n\right\rangle$ contains a fixed number N_n of constituent quanta, the ith of which has rest mass m_i and momentum k_i^μ (out of the total momentum P^μ). It is important to emphasize that not all possible Fock states contribute to a given state. For example, there is no connection between the $\left|\ell^+\ell^-\right\rangle$ and $\left|\ell^+\ell^-\ell^+\right\rangle$. The kinematics may alternatively be described in terms of longitudinal

boost-invariant quantities $x_i \equiv k_i^+/P^+$ ($0 \leq x_i \leq 1$) and $\boldsymbol{k}_{\perp i}$, and helicities λ_i, so that

$$\sum_{i=1}^{N_n} x_i = 1, \quad \sum_{i=1}^{N_n} \boldsymbol{k}_{\perp i} = \boldsymbol{P}_\perp, \tag{2.5}$$

and, working in the *intrinsic frame*, in which $\boldsymbol{P}_\perp = 0$, the Hamiltonian simplifies and the four-momentum of a single particle is given by

$$k_i^\mu = \left(x_i P^+, \boldsymbol{k}_{\perp i}, \frac{m_i^2 + \boldsymbol{k}_{\perp i}^2}{x_i P^+} \right). \tag{2.6}$$

Using the completeness of the states $|\mu_n\rangle$, the decomposition then reads

$$|\Psi\rangle \equiv \sum_n \int [\mathrm{d}\mu_n] |\mu_n\rangle \langle \mu_n | \Psi; M, P^+, \boldsymbol{P}_\perp, S^2, S_z; h\rangle$$

$$\equiv \sum_n \int [\mathrm{d}\mu_n] |\mu_n\rangle \Psi_{n|h}(\mu), \tag{2.7}$$

where the measure notation indicates an integration over values of all constituent x_i, $\boldsymbol{k}_\perp$, subject to the constraints of Eq. (2.5). The functions $\Psi_{n|h}(\mu)$, where now h and μ are shorthand for all the intrinsic and kinematic quantum numbers, respectively, of the Fock state n, are called the *component wave functions* of the state and are the central objects of interest in light-front calculations.

The Hamiltonian expression Eq. (2.3) then becomes

$$\frac{M^2 + \boldsymbol{P}_\perp^2}{P^+} \Psi_{n|h}(x_i, \boldsymbol{k}_{\perp i}, \lambda_i) =$$

$$\sum_{n'} \int [\mathrm{d}\mu_{n'}] \langle \mu_n : x_i, \boldsymbol{k}_{\perp i}, \lambda_i | P^- | \mu_{n'} : x_i', \boldsymbol{k}_{\perp i}', \lambda_i' \rangle \Psi_{n'|h}(x_i', \boldsymbol{k}_{\perp i}', \lambda_i'),$$

$$\tag{2.8}$$

which is an exact infinite-dimensional integral equation for the component wave functions $\Psi_{n|h}(\mu)$. Although this expression has been derived from a full QFT with no approximations, it may be identified as the Schrödinger equation on the light-front.

For a gauge theory like QED, the light-cone gauge $A^+ = 0$ is the most natural choice of gauge fixing because it eliminates the spatial non-transverse modes. Using

the equations of motion, one may then eliminate the A^- component in favor of the other fields in the theory; this inversion is subtle due to the existence of zero modes of A^+. The result is a fairly complicated but closed-form exact Hamiltonian that may be used to develop front-form Feynman rules [2, 114].

The Hamiltonian can be described by the sum of a kinetic operator T and various types of interactions: *seagulls* S [and their normal-ordered *contractions* C], which do not change particle number, *vertices* V, which change particle number by one, and *forks* F, which change particle number by two:

$$H_{\mathrm{LC}} = T + V + S + C + F \,. \tag{2.9}$$

The exact form of each operator has been worked out and can be found in Appendix C. The connection of the lowest Fock states by these interactions for true muonium is summarized in Table 2.1 for two flavors.

Why, given that instant-form field theory has only one interaction, does the front-form Hamiltonian have multiple interactions classified into five types? The answer rests in two different issues: time-ordering and gauge fixing. Since Hamiltonian methods require a fixed time slice, the use of time-ordered interactions is required. In this time-ordered front-form theory, topologically equivalent diagrams are not interchangeable (this can be restated as different time orderings are not added into a single diagram, as in the instant form). Instead, changing the ordering of interactions in time changes the diagram. This feature will be critical to understanding the calculation of the $|\gamma\gamma\rangle$ process, where multiple interactions exist. For example, consider the two vertex diagrams in Fig. 2.1, where time propagates left to right. These are *dynamical* interactions, so called because all particles in them are fully dynamical. In instant form, these diagrams are given by the same interaction. In front form, these are given by different, albeit related, operators. The other possible interactions, like

Sector	n	0	1	2	3	4	5	6	7	8
$\lvert\gamma\rangle$	0	•	V	V	·	F	F	·	·	·
$\lvert e^+e^-\rangle$	1	V	•	S	S	V	·	F	·	F
$\lvert\mu^+\mu^-\rangle$	2	V	S	•	S	·	V	·	F	F
$\lvert\gamma\gamma\rangle$	3	·	S	S	•	V	V	·	·	·
$\lvert e^+e^-\gamma\rangle$	4	F	V	·	V	•	S	V	·	V
$\lvert\mu^+\mu^-\gamma\rangle$	5	F	·	V	V	S	•	·	V	V
$\lvert e^+e^-e^+e^-\rangle$	6	·	F	·	·	V	·	•	·	S
$\lvert\mu^+\mu^-\mu^+\mu^-\rangle$	7	·	·	F	·	·	V	·	•	S
$\lvert\mu^+\mu^-e^+e^-\rangle$	8	·	F	F	·	V	V	S	S	•

Table 2.1: The Hamiltonian matrix for two-flavor QED, where n labels Fock states. The vertex, seagull and fork interactions are denoted by V, S, F respectively. Diagonal matrix elements are indicated by •, and vanishing matrix elements by a ·.

pair annihilation and an anti-particle emitting a photon, are also different but related.

The choice of the light-cone gauge, $A^+ = 0$, introduces the complication of *instantaneous* interactions, which are commonly separated into the seagull, forks, and contractions. In deriving the Hamiltonian of a front-form theory, terms proportional to $1/\partial^+$ arise. Formally, these terms require a careful treatment otherwise the equivalence to the instant form could broken. In light-cone gauge, for any dynamical interaction built from two vertex interactions, an equivalent interaction where the exchanged particle propagates instantaneously must be included. An example of each type of instantaneous interaction is found in Fig. 2.2. Notationally, an instantaneous particle propagator is indicated by a vertical line with a slash through its center. Mathematically, instantaneous interactions have no direct dependence upon
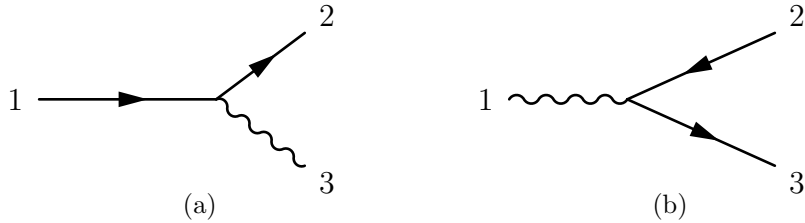
Figure 2.1: Two Vertex Diagrams: (a) $V_{\ell \to \ell\gamma}$, Which Involves an Emitted Photon, and (b) $V_{\gamma \to \ell^- \ell^+}$, Representing Pair Production.

the momentum of the instantaneous particle.

Proceeding further, the work in this thesis will focus on the two-equal-mass valence particles interacting via the effective potential V_{eff} that is an approximation derived from the exact Hamiltonian interactions. Using the method of iterated resolved explained in Appendix F, it is possible to write the effective integral equation as only over $|\ell^+ \ell^-\rangle$ states explicitly, and is described by

$$
\left(M^2 - \frac{m^2 + \boldsymbol{k}_\perp^2}{x(1-x)} \right) \Psi_{n|h}(x, \boldsymbol{k}_\perp; \lambda_1, \lambda_2)
$$
$$
= \sum_{\lambda_1', \lambda_2'} \int_D \mathrm{d}x' \mathrm{d}^2 \boldsymbol{k}_\perp' \langle x, \boldsymbol{k}_\perp; \lambda_1, \lambda_2 | V_{\text{eff}} | x, \boldsymbol{k}_\perp; \lambda_1', \lambda_2', \rangle \Psi_{n|h}(x', \boldsymbol{k}_\perp'; \lambda_1', \lambda_2').
$$

$$(2.10)$$

where D a restricted domain of integration which allows for the problem to be properly regulated. While the problem is now cast so only $|\ell^+ \ell^-\rangle$ components of the wave function need be considered, the other components have been interated into the V_{eff} and can be extracted from the remaining components after the Hamiltonian has been diagonalized. How this V_{eff} is derived is discussed in general in Appendix F and Chapter 3 will discuss how the non-perturbative propagator for the exchange and annihilation channels need in this work are obtained.
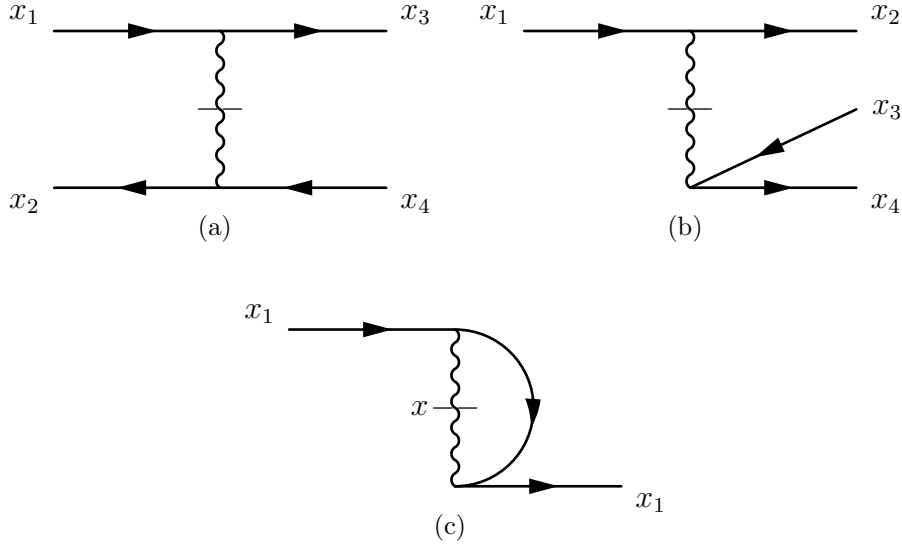
Figure 2.2: Examples of instantaneous interactions: (a) the scattering-channel seagull interaction between particle and antiparticle, $S^{(s)}_{\ell^+\ell^- \to \ell^+\ell^-}$, (b) a fork interaction $F_{\ell^- \to \ell^+\ell^-\ell^-}$, and (c) A contraction interaction $C^{\gamma}_{\ell^-}$ that represents an instantaneous photon correction to the self-energy of the particle.

2.3   Issues of Front-Form Theories

The rosy picture so far painted would lead one to wonder why all theorist don't do calculations in front-form. Several complications unique to the front-form exist, and at present the question of their relative difficulty to overcome compared to instant form is unclear.

The first issue is related to rotational invariance. As discussed above, the front-form trades rotational invariance of a state for boost-invariance. If an all-orders calculation could be performed, the physical results will regain rotational invariance. For truncated calculations, either in Fock state or α, the breaking of rotational invariance is commonplace. This breaking can be mitigated by the inclusion of higher-order corrections, or it can be repaired by the implementation of counterterms.

Instant-form physics has a non-trivial vacuum, where it is imagined that pair production is occurring constantly and the particle-number of the vacuum is undefined. In contrast, the front-form vacuum is the Fock-state vacuum, completely devoid of particles. How these seemingly incompatible pictures can be reconciled is through zero modes. For this thesis, zero modes will be understood as eigenvectors of the Hamiltonian with $P^+ = 0$ occurring from complicated limits and constraints imposed by the theory. While they can modify the energy levels of a theory, they haven never been found to have any significant effect in QED and therefore have been assumed to be negligible for bound-state calculations[192, 193, 164, 194].

Perhaps the most difficult problem with front-form dynamics is renormalization. In instant form, divergences are nicely separated into infrared ($p^2 \to 0$) and ultraviolet ($p^2 \to \infty$) terms. The splitting of the momentum into p^+ and $\boldsymbol{p}_\perp$ by the symmetries on the light front can be best seen in the energy $p^- = \frac{m^2 + \boldsymbol{p}_\perp^2}{p^+}$. Without full rotational invariance as a symmetry, divergences can occur for $\boldsymbol{p}_\perp^2 \to 0, \infty$, and separately $p^+ \to 0, \infty$. The end result is that, while the front form has an enhanced number of kinematic operators, the number of counterterms needed to restore the broken dynamical symmetries is unfortunately increased. The effect of $1/p^+ \to 0$ divergences is that naive regularization using a principal value prescription doesn't work, but this can be overcome by a careful treatment that was developed by Leibbrant and Mandelstam[195, 196, 197] and expanded to non-Abelian theories by Bassetto[198].

Also distinct from instant form, the more natural truncation is in Fock states. Unlike the instant-form truncation in α, this approach can potentially break gauge symmetry. A good introduction to these ideas and how they can be applied to weak-coupling QCD can be found in [199]. In perturbative calculations, the issue of renormalization can be tackled with only a minor additional effort, using the standard Pauli-Villars techniques or dimensional regularization. Mustaki et al. in [200] inves-

tigated renormalization for QED and reproduced a number of classic perturbative results.

For nonperturbative questions, though, more elaborate methods are required. Much time has been spent in developing workable Pauli-Villars techniques[201, 202, 203, 204], and while these seem usable in principle, they require a dramatic increase in the number of Fock states since multiple Pauli-Villars particles are then required for each physical particle. Attempts to use Fock-state-dependent renormalization counterterms have been developed[205, 206, 207, 208, 209, 210] but these need to be partially derived analytically and for large Fock-state problems, the methods seems daunting. Instead of making an explicit Fock-state truncation, some authors have endeavored to expand in coherent states[211, 212, 213, 214, 215, 216]. A related method is to use coupled-cluster methods from NRQM[217, 218]. The final prominent method for nonperturbative problems is to use flow equations to perform unitary transformations of the Hamiltonian to such a form that higher-order Fock states are decoupled[219, 220, 221, 222, 223, 224, 225]. These equations have the benefit that they can be automated onto a computer. For all methods, the major impediment is that the computational resources needed for even simple problems like positronium with these methods is quite large. In this work, we will side-step the formal issue of renormalization entirely, and focus on producing only regularized results.

Chapter 3

THE $\ell^+\ell^-$ MODEL

In this thesis the model considered is the charge-zero, lepton family number-zero states in the truncated Fock space of

$$|\Psi\rangle = \psi_{\mu^+\mu^-}|\mu^+\mu^-\rangle + \psi_{e^+e^-}|e^+e^-\rangle + \psi_{\tau^+\tau^-}|\tau^+\tau^-\rangle + \psi_\gamma|\gamma\rangle$$
$$+ \psi_{\mu^+\mu^-\gamma}|\mu^+\mu^-\gamma\rangle + \psi_{e^+e^-\gamma}|e^+e^-\gamma\rangle + \psi_{\tau^+\tau^-\gamma}|\tau^+\tau^-\gamma\rangle. \quad (3.1)$$

Solving for the eigenstates of H_{LC} [Eq. (2.10)] with this limited Fock space nonetheless gives the bound states of positronium (e^+e^-), true muonium ($\mu^+\mu^-$), and true tauonium ($\tau^+\tau^-$), as well as associated continuum states (up to effects from neglected higher-order Fock states). The wave functions are in the form of Eq. (3.1), with helicity states for only $|\mu^+\mu^-\rangle$, $|e^+e^-\rangle$, and $|\tau^+\tau^-\rangle$ components. The $|\gamma\rangle$ and $\left|\ell\bar{\ell}\gamma\right\rangle$ components are folded into V_{eff} by means of the method of iterated resolvents[226, 1] which are discussed in more detail in Appendix F. Using iterated resolvents, the Hamiltonian equation can be constructed only between $|\ell^+\ell^-\rangle$ states. The truncations and approximations used to arrive at the final effective Hamiltonian studied in this work lead to an equation that, while regularized, is not properly renormalized. This outstanding problem is beyond the scope of this work.

Following the treatment in Appendix F, the construction of the effective model of true muonium includes only the single-exchange and single-annihilation photon intermediate states. Higher Fock states only couple to the $|\ell^+\ell^-\rangle$ state through these interactions and their associated instantaneous diagrams (which together should be neglected to preserve gauge invariance).

3.1   Exchange Channel

In this model, it is possible to discuss the exchange and annihilation channels separately as effective interactions since they are decoupled in this Fock space. In this section, the derivation of the propagator for the exchange interaction is fleshed out. The schematic equation to solve for this two-state system is

$$
M^2|\Psi\rangle = H_{LC}|\Psi\rangle = \begin{pmatrix} T+S & V \\ V & T+S \end{pmatrix} \begin{pmatrix} \psi_{\ell^+\ell^-} \\ \psi_{\ell^+\ell^-\gamma} \end{pmatrix},
\tag{3.2}
$$

where we have suppressed the individual flavor wavefunctions, because in this Fock space, flavor mixing is forbidden. Formally, we can solve this equation in block form to get an eigenvalue equation only in the $\psi_{\ell^+\ell^-}$ sector by

$$
H_{LC}|\Psi\rangle = (T + S + VG_{\text{NP}}V)|\psi_{\ell^+\ell^-}\rangle,
\tag{3.3}
$$

where the interaction elements T, S, and V are given by the Feynman rules, and the non-perturbative propagator is given by

$$
G_{\text{NP}}(\omega) = \sum_n \langle \ell^+\ell^-\gamma|\psi_{\ell^+\ell^-\gamma,n}\rangle \frac{1}{\omega - H_{LC}} \langle \psi_{\ell^+\ell^-\gamma,n}|\ell^{+'}\ell^{-'}\gamma'\rangle.
\tag{3.4}
$$

In this propagator, we have introduced a *redundancy parameter* ω. To solve this equations exactly, we would solve the Hamiltonian equation along with the constraint $M^2(\omega) = \omega$ for each eigenvalue. This is prohibitively difficult, so we will introduce further simplifications that where first formalized by Pauli[227]. In addition to ω, the denominator depends on the entire H_{LC}, which couples to the $|\ell^+\ell^-\gamma\rangle$ state. From the method of iterated resolvents, we know that in full QED, this is an infinite tower of interactions, but that truncation can be made to just the leading order of "in-medium perturbation theory" discussed in Appendix F where in the denominator H_{LC} can be replaced by the eigenvalues $M^2_{\ell^+\ell^-\gamma,n}$ that are dominated by $|\psi_{\ell^+\ell^-\gamma}\rangle$. At

23

this point, there are two functions: ω, $M^2_{\ell^+\ell^-\gamma,n}$ in the denominator that are unknown and need definitions to make the problem tractable. First, using notation of *spectator interactions*, [1] the eigenvalues $M^2_{\ell^+\ell^-\gamma,n}$ can be approximated by states that are an $|\ell^+\ell^-\rangle$ bound state freely propagating with a single photon. These eigenvalues would be given by

$$M^2_{\ell^+\ell^-\gamma,n} = \frac{M^2_{\ell^+\ell^-,n} + \boldsymbol{q}^2_\perp}{y} + \frac{\boldsymbol{q}^2_\perp}{1-y}, \tag{3.5}$$

where the four-momentum $q^\mu = (yP^+, y\boldsymbol{P}_\perp + \boldsymbol{q}_\perp, q_g^-)$ is the momentum of the photon. Note that, since we work in the frame $\boldsymbol{P}_\perp = 0$, $\boldsymbol{q}_\perp$ is a measure of relative momentum of the photon versus the fermions. The intuition behind these approximation is that, to leading order, the states of $|\ell^+\ell^-\gamma\rangle$ are product states $|\ell^+\ell^-_m\rangle \otimes |\gamma_s\rangle$. Given this approximation, the bound states form the lowest energy levels of bands of eigenvalues in which a single photon is added with an arbitrary momentum. States where the fermions are free would be heavier, and therefore contribute less to the propagator.

Having defined an approximation of $M^2_{\ell^+\ell^-\gamma}$, the remaining issue is how to treat ω. Given the definition of $\omega = M^2(\omega) = M^2_{\ell^+\ell^-,n}$, we can insert the approximation of $M^2_{\ell^+\ell^-\gamma,n}$ into Eq. 3.4, arriving at

$$G_{\mathrm{NP}}(\omega) = \sum_n \langle \ell^+\ell^-\gamma | \psi_{\ell^+\ell^-\gamma,n} \rangle \frac{1}{M^2_{\ell^+\ell^-,n} - \frac{M^2_{\ell^+\ell^-,n}+\boldsymbol{q}^2_\perp}{y} + \frac{\boldsymbol{q}^2_\perp}{1-y}} \langle \psi_{\ell^+\ell^-\gamma,n} | \ell^{+'}\ell^{-'}\gamma' \rangle. \tag{3.6}$$

Proceeding further, two major approximations common to many-body physics are made. The first is to assume to degeneracy of the spectrum to the lowest state, $M^2_{\ell^+\ell^-,n} \equiv M^2$. Given the Bohr spectrum, we can see that the band of energy states

---

[1] While H_{LC} in the denominator of the propagator includes all possible interactions that state couples to, there is a natural decomposition into *spectator interactions* where the interactions on the state are unaffected by a spectator particle, and *non-spectator interactions* where there is an interaction between the particles and the effective degrees of freedom desired. For example, the $|\ell^+\ell^-\gamma\rangle$ state can interact by passing a second photon between the fermions. The first photon only effects the dynamics by restricting the momentum range, therefore this interaction appears identical to the one in the $|\ell^+\ell^-\rangle$ state. In contrast, the interaction where the free photon pair produces two more fermions has no analogy to an $|\ell^+\ell^-\rangle$ process, and therefore is termed a non-spectator interaction.

we are compressing is from $M^2_{\ell,\infty} = (2m_\ell)^2$ down to $M^2_{\ell^+\ell^-,0} = (2m_{\ell^+\ell^-})^2(1 - \frac{\alpha}{8})^2$.

From this equation, it is seen that the smaller α, the better this approximation is.

G_{NP} can then be expressed as

$$G_{\mathrm{NP}} = \frac{-y(1-y)}{y^2 M^2 + \boldsymbol{q}^2_\perp} \sum_n \langle \ell^+\ell^-\gamma | \psi_{\ell^+\ell^-\gamma,n} \rangle \langle \psi_{\ell^+\ell^-\gamma,n} | \ell^{+'}\ell^{-'}\gamma' \rangle. \tag{3.7}$$

The assumption of degeneracy has allowed for factoring the functional dependence of the propagator out, and with this, the assumption of closure can by applied. Closure is the statement that summing over all states equals the identity matrix, i.e. $\sum_n |n\rangle\langle n| = 1$. Therefore a sum over the states in the propagator results in a delta function, i.e.,

$$\sum_n \langle \ell^+\ell^-\gamma | \psi_{\ell^+\ell^-\gamma,n} \rangle \langle \psi_{\ell^+\ell^-\gamma,n} | \ell^{+'}\ell^{-'}\gamma' \rangle = \langle \ell^+\ell^-\gamma | \ell^{+'}\ell^{-'}\gamma' \rangle. \tag{3.8}$$

If G_{NP} defined with these assumptions is compared to the free, perturbative propagator,

$$G_{\ell^+\ell^-\gamma,\mathrm{free}} = \frac{1}{P^+(k^- - k'^- - q^-)} = \frac{-y}{y^2(2m)^2 + \boldsymbol{q}^2_\perp}, \tag{3.9}$$

it can be seen that in the double limit of $y \ll 1$ (the photon contains a small fraction of the energy) and $M^2 \approx (2m)^2$ (weakly interacting states), the two propagators agree.

All that remains to do to completely fix the non-perturbative propagator is to specify a functional form for M^2. Given that we have a truncated Fock space, gauge invariance has been broken at some level. The particular functional form of M^2 is chosen to restore this invariance at leading order. Computing the interactions shown in Fig. 3.1, but instead of $G_{\ell^+\ell^-\gamma,\mathrm{free}}$, G_{NP} is used, a collinear singularity is introduced by the mismatch between the instantaneous diagram and the two dynamical ones. For only one unique form does M^2 property cancel this singularity, the so called

25

symmetric mass which is the average of the incoming and outgoing $|\ell^+\ell^-\rangle$ states,

$$M_{\text{sym}}^2 = \frac{1}{2}\left(\frac{m_\ell^2 + \boldsymbol{k}_\perp^2}{x(1-x)} + \frac{m_{\ell'}^2 + \boldsymbol{k}_\perp'^2}{x'(1-x')}\right) \tag{3.10}$$

So, consistency of the effective theory has completely constrained the form of the non-perturbative propagator[226]. As was emphasized by Pauli[226], although a number of simplifications have been made, it is possible to systematically improve the approximation. One obvious way would be to implement an iterated solver that takes $M_{\ell^+\ell^-,i}^2$ obtained in iteration i and then use them instead as the $M_{\ell^+\ell^-,n}$ eigenstates, bypassing the assumption of degeneracy entirely. This can be used to obtain the exact non-perturbative propagator, which is related to Eq. (3.7) by

$$G_{\text{NP}}(\omega) = G_{\text{NP}}\Bigg(\langle \ell^+\ell^-\gamma|\ell^{+'}\ell^{-'}\gamma'\rangle$$

$$-\sum_n \langle \ell^+\ell^-\gamma|\psi_{\ell^+\ell^-\gamma,n}\rangle \frac{M_{\ell^+\ell^-,n}^2 - M^2}{-G_{\text{NP}}^{-1} + (M_{\ell^+\ell^-,n}^2 - M^2)}\langle \psi_{\ell^+\ell^-\gamma,n}|\ell^{+'}\ell^{-'}\gamma'\rangle\Bigg).$$

$$\tag{3.11}$$
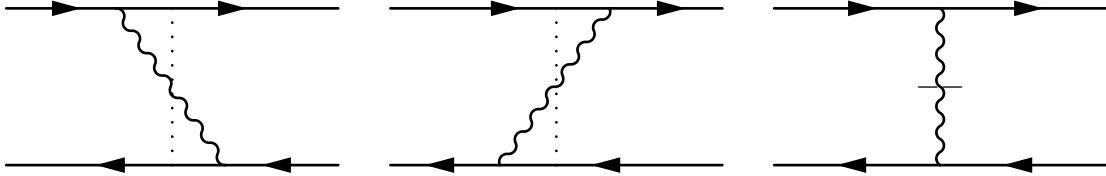
Figure 3.1: The three diagrams that contribute to the effective interaction in the exchange channel.

3.2   Hamiltonian Matrix Elements for General J_z

Breaking of rotational invariance by the anisotropy of light-front coordinates and the model's truncation manifests itself in the spectra by the observation of non-degeneracy of J_z states. To explore this phenomenon, in addition to allowing for

smaller matrices, it is beneficial to integrate out the φ dependence of the wave functions and exchange it for the discrete quantum number J_z. The independent φ dependences are classified with respect to L_z, but this isn't a good quantum number for the whole state. To do this, we consider a set of two-particle states

$$\Psi_{n|h}(x_i, \boldsymbol{k}_{\perp i}, \lambda_i) = \sum_{L_z} \psi_{n|h}(x, k_\perp, \lambda_1, \lambda_2) e^{iL_z\varphi}. \tag{3.12}$$

Using this expression for the wave function, we can construct the matrix elements for a fixed J_z state as a Fourier transform. Even though L_z isn't a good quantum number, the decomposition $L_z = J_z - S_z$ remains valid, therefore this exchange can be performed in the integrals. This results in states of well defined J_z but different S_z components mixing with each other. For the states considered in this model, it can be shown that exchange channel effective interactions' dependence upon φ can be expressed in the form of

$$\langle \mu_n : x, k_\perp, \varphi, \lambda_i | V_{\text{eff}} | \mu_{n'} : x', k'_\perp, \varphi', \lambda'_i \rangle = E_n(x, k_\perp, \varphi, x', k'_\perp, \varphi'; \lambda_i, \lambda'_j)$$
$$= \frac{F_n(x, k_\perp, , x', k'_\perp, ; \lambda_i, \lambda'_j)}{a - 2k_\perp k'_\perp \cos(\varphi - \varphi')}, \tag{3.13}$$

where the E_n are found in Table D.2. For these elements, it is possible to analytically compute the fixed J_z elements by decomposing $e^{\pm ix}$ into $\cos(x) \pm i \sin(x)$ terms. The terms proportional to $\sin(\varphi - \varphi')$ in the Fourier transforms integrate to zero, leaving

$$G_n(x, k_\perp, x', k'_\perp; \lambda_i, \lambda'_j, J_z)$$
$$= F_n(x, k_\perp, x', k'_\perp; \lambda_i, \lambda'_j) \frac{1}{(2\pi)^2} \int_0^{2\pi} \mathrm{d}\varphi \int_0^{2\pi} \mathrm{d}\varphi' \frac{\cos(-[J_z - S_z]\varphi + [J'_z - S'_z]\varphi')}{a - 2k_\perp k'_\perp \cos(\varphi - \varphi')}$$
$$= F_n(x, k_\perp, x', k'_\perp; \lambda_i, \lambda'_j) \times 2\pi(-A)^{-|n|+1} \left(\frac{B}{k_\perp k'_\perp}\right)^{|n|}$$
$$= F_n(x, k_\perp, x', k'_\perp; \lambda_i, \lambda'_j) \times Int(|n|), \tag{3.14}$$

27

where n incorporates the quantized eigenvalue of J_z, and the definitions found in Trittmann[1] have been used:

$$A = (a^2 - 4k_\perp^2 k_\perp'^2)^{-\frac{1}{2}} \quad \text{and} \quad B = \frac{1}{2}(1 - aA). \tag{3.15}$$

The G_n's have been collected into Table D.3 and represent the matrix elements utilized in TMSWIFT.

3.3   Annihilation Channel
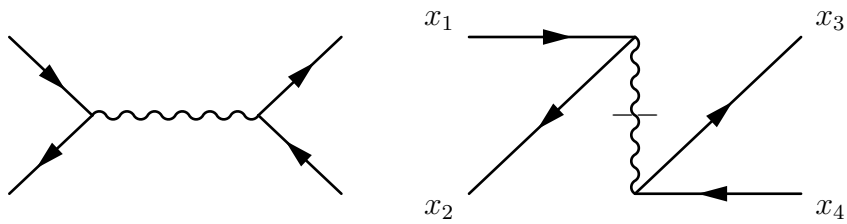
Figure 3.2: Dynamical and instantaneous diagrams for the annihilation channel.

In contrast to the exchange channel, the annihilation channel has a number of simplifications that can be taken advantage of. First, if the logic of the previous sections is applied, the non-perturbative propagator given by

$$G_{\text{NP},\gamma} = \frac{1}{M_{\text{sym}}^2 - M_\gamma^2} \langle \gamma | \gamma' \rangle \tag{3.16}$$

is simple because the mass eigenvalues $M_\gamma^2 = 0$ in the photon sector. With this constraint, correctly canceling the instantaneous diagram requires only using the symmetric mass term, leading to the expression $G_{\text{NP},\gamma} = 1/M_{\text{sym}}^2$. In the annihilation channel, the possibility of $m_\ell \neq m_{\ell'}$ is the origin of flavor mixing in this model. The actual matrix elements can be derived, with care taken to note the kinematic constraints,

$$\boldsymbol{k}_{\perp,\gamma} = \boldsymbol{k}_{\perp,\ell^-} + \boldsymbol{k}_{\perp,\ell^+} = 0, \quad \text{and} \quad x_\gamma = 1. \tag{3.17}$$

28

The annihilation vertex interaction $V_{\gamma \to \ell^+ \ell^-}$ can then follow the procedure developed for the exchange channel, and be broken into three components based upon the particle helicity factors. Exploiting the symmetry of $\langle \ell^+ \ell^- |V|\gamma \rangle = \langle \gamma |V| \ell^+ \ell^- \rangle^*$ and applying the method of exchanging $\varphi \to J_z$, we can obtain the I_n matrix elements in Table D.4. With a denominator that has no dependence upon φ, this dynamic interaction is non-zero only for the case where $J_z = \pm 1$.

In the case of the seagull diagram, the simple kinematics result in only a single, constant matrix element:

$$\langle \ell^+ \ell^- |S| \ell^+ \ell^- \rangle = \frac{4\alpha}{\pi} \delta^{\lambda_2}_{-\lambda_1} \delta^{\lambda'_2}_{-\lambda'_1}. \tag{3.18}$$

Inspecting the helicity factors, we see that this interaction can only occur between $S_z, S'_z = 0$.

3.4   Regularization

The appearance of reciprocal powers of momenta in Eq. (2.3), which is the ultimate origin of the singularities at $x = 0$ or 1 in Eq. (2.10), requires a careful regularization of numerical integrals. The domain D in Eq. (2.10) is defined by introducing a cutoff Λ on the parton transverse momentum $\boldsymbol{k}_\perp$; in the equal-mass case, we choose for each flavor [114]

$$\frac{m_\ell^2 + \boldsymbol{k}_\perp^2}{x(1-x)} \leq \Lambda_\ell^2 + 4m_\ell^2 . \tag{3.19}$$

Instituting a momentum-space cutoff has the added effect of minimizing the influence of multiparticle Fock states. In principle, each sector of the theory (in our case, notably $\mu^+ \mu^-$ and $e^+ e^-$) can have an independent cutoff, but such choices must be motivated by the physical scales of the problem, and in any case the final results must eventually be insensitive to such particular choices.

It has been shown[163, 1, 228] that strong dependence in $^1S_0$ states on Λ arises

from the matrix element between antiparallel-helicity states called G_2:

$$G_2(x, k_\perp; x', k'_\perp) = \left[m_\ell^2 \left(\frac{1}{xx'} + \frac{1}{(1-x)(1-x')} \right) + \frac{k_\perp^2}{x(1-x)} + \frac{k'^2_\perp}{x'(1-x')} \right] Int(|n|)$$
$$+ k_\perp k'_\perp \left[\frac{Int(|1-n|)}{xx'} + \frac{Int(|1+n|)}{(1-x)(1-x')} \right] \tag{3.20}$$

In the limit of $k_\perp \equiv |\boldsymbol{k}_\perp|$ or $k'_\perp \equiv |\boldsymbol{k}'_\perp| \to \infty$, this interaction approaches

$$\lim_{k_\perp \to \infty} G_2 = -\frac{\alpha}{\pi} \frac{2}{x + x' - 2xx'} \tag{3.21}$$

for $J_z = 0$ which, in the absence of the dependence of $|\psi_{\ell^+\ell^-}\rangle$ upon $k_\perp$, would result is a δ function-like behavior in configuration space. Ref. [163] chose to regularize this singularity by deleting a term equivalent in the notation here to

$$G_{2,\text{div}}(x, k_\perp; x', k'_\perp) = \left[\frac{k_\perp^2}{x(1-x)} + \frac{k'^2_\perp}{x'(1-x')} \right] Int(|n|) \tag{3.22}$$

Instead, a superior subtraction scheme is obtained by only removing its limit as $k_\perp$ or $k'_\perp \to \infty$ (Eq. 3.21),

$$G_{2,\text{REG}} = G_2 + \left\{ \frac{\alpha}{\pi} \frac{2}{x + x' - 2xx'} \delta_{J_z,0} \right\} \tag{3.23}$$

which retains part of the term (including x and x' dependence). This scheme removes the strong Λ dependence of $^1S_0$ states in both QED[228, 229] and QCD[174] models. It is important to note that the $\boldsymbol{k}_\perp$-dependence of $|\psi_{\ell^+\ell^-}\rangle$ varies with α, and therefore it should be anticipated that the strength of this apparent divergence should depend on α. This will be explored in Chapter 4.

Chapter 4

SPECTRA AND DECAY CONSTANTS

Having developed the general ideas of light-front calculations in Chapter 2 and the exact formalism of the effective light-front Hamiltonian in Chapter3, in this chapter will be presented results for true muonium bound states obtained from numerical calculations. The general points of how the numerical implementation works are discussed in Appendix E. To produce these results, two codes were utilized.

The first is a modified version of MESONIX, a code developed by Trittmann[1]. Improvements to his code included implementing more efficient numerical integrators for the Coulomb trick [see Appendix E], different discretization schemes, the improved regularization discussed in Chapter 3, and allowing for a second flavor of leptons to interact. This code was written in C and could only run in serial mode.

As will be discussed, while MESONIX was able to produce useful results, it was limited in its reach by the numerical resources available for a serial code. In the effort to modernize DLCQ, a new code TMSWIFT (True Muonium Solver With Front-Form Techniques) was developed. This code was developed in C++ and utilizes the parallel matrix and vector package PETSc[230, 231] as well as the parallel eigenvalue solver package SLEPc[232]. This new code has broader capabilities than MESONIX for a number of reasons. TMSWIFT allows for an arbitrary number of particle flavors, each with different $m_\ell, \Lambda_\ell, N_\mu$, and N_θ. Further, in order to overcome the issues that arise from sampling continuum e^+e^- contributions to true muonium, a number of different discretizations are available to test. Like MESONIX, TMSWIFT allows for different values of J_z and α. With TMSWIFT's parallel capabilities, the size of accessible Hamiltonians has been greatly increased, and the time to obtain solutions

dramatically decreased. TMSWIFT is currently available at[233].

4.1 Cutoff Dependence

In front form, the most common renormalization scheme for two-body systems is the covariant cutoff approach of Lepage and Brodsky [114], which as stated is also used in throughout this work. To remind the reader, it is given by

$$\frac{m_\ell^2 + \boldsymbol{k}_\perp^2}{x(1-x)} \leq \Lambda_\ell^2 + 4m_\ell^2 \,. \tag{4.1}$$

Unfortunately, in any but the simplest models, this formulation does even not properly regularize the Hamiltonian as new sectors are added. More recent attempts to utilize other renormalization schemes include Pauli-Villars [201, 202] and Hamiltonian flow [221, 222] techniques, and methods with sector-dependent counterterms [205, 208].

For the purposes of this thesis, the simplest possible renormalization scheme is taken by defining covariant cutoffs via Eq. (4.1) for each flavor of lepton. Identifying Λ_ℓ as a maximum off-shell momentum for the parton of mass m_ℓ, physical considerations lead one to expect that Λ_ℓ values should form a tower, with the heaviest components having the smallest cutoff.

4.1.1 Two-Flavor Cutoff Dependence

In the two-flavor true muonium case, choices such as $\Lambda_e^2 = \Lambda_\mu^2 + 4(m_\mu^2 - m_e^2)$ are natural, and this is the scheme adopted for the multiple-flavor studies unless indicated otherwise. In particular, Λ_e should be chosen significantly larger than Λ_μ, or else the phase space for $|e\bar{e}\rangle$ continuum states contributing to true muonium is inappropriately truncated, leading to numerical instabilities due to undersampling of physically significant amplitudes. This physically appropriate choice nevertheless

Figure 4.1: Mass eigenvalues of $n = 1$ true muonium states with $J_z = 0$ ($1\,^3S_1^0$ in top pair, $1\,^1S_0^0$ in bottom pair) as a function of cutoff Λ_μ for $\Lambda_e^2 = \Lambda_\mu^2 + 4(m_\mu^2 - m_e^2)$, $\alpha = 0.3$, $m_e = \frac{1}{2}m_\mu$, $N = 25$. Λ_μ is given in units of the muon Bohr momentum $\alpha m_\mu/2$. The ($\circ$) points indicate the full result precisely following the methods of Ref. [1], and the ($\blacksquare$) points indicate the result after the implementation of a subtraction (described in the text) of the amplitude responsible for poor ultraviolet behavior in $^1S_0$ channels.

leads to interesting numerical issues, as will be discussed.

To investigate the effect of this choice of cutoffs, Λ_e is fixed by the procedure described above and Λ_μ is varied between $1 \leq \Lambda_\mu \leq 65$ (in units of muon Bohr momentum $\alpha m_\mu/2$). Results for the $n = 1, 2$ eigenstates with $m_e = \frac{1}{2}m_\mu$ can be seen in Figs. 4.1 and 4.2, respectively, which can be compared to Figs. 2.8 and 2.9 of Ref. [1], where the same study was performed for positronium. For an exact analogue to the results of Ref. [1], one should compare the lines in Fig. 4.1 with open-circle points directly to their analogues in the earlier work. Since rotational invariance is obscured in the front form, states studied in the numerical simulations are labeled by adding the J_z label, as in $n\,^{2S+1}L_J^{J_z}$.

33
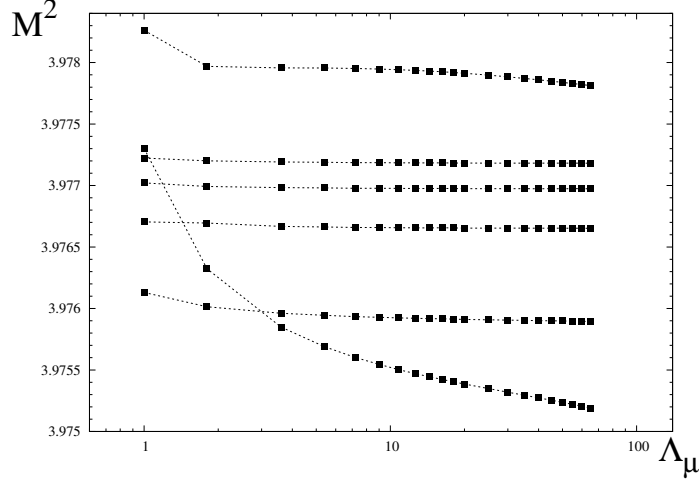
Figure 4.2: Mass eigenvalues of $n = 2$ true muonium states with $J_z = 0$ (top to bottom: $2\,^3S_1^0$, $2\,^3P_2^0$, $2\,^1P_1^0$, $2\,^3P_1^0$, $2\,^3P_0^0$, $2\,^1S_0^0$) as a function of cutoff Λ_μ. The numerical inputs and units of $\Lambda_{e,\mu}$ are the same as in Fig. 4.1. The amplitude subtraction described in the text has been performed for all states here.

The most striking feature of the initial (open-circle points) results in Fig. 4.1 is the strong dependence on the cutoff Λ_μ of the 1^1S_0 mass eigenvalue compared to that of 1^3S_1 (A similar effect occurs for the 2^1S_0 mass eigenvalue, as seen in Fig. 4.2). One may initially wonder whether this effect is due to an inappropriate handling of lepton mass renormalization. The full shift of the bound-state mass due to one-loop lepton-mass renormalization in front form is given by [163]

$$
\begin{aligned}
\Delta M^2 \;=\;& \frac{\alpha}{2\pi} m^2 \left[3\ln\left(\frac{\Lambda^2 + m^2}{m^2} \right) - \frac{\Lambda^2}{\Lambda^2 + m^2} \right] \\
& \times \left(\frac{1}{x} + \frac{1}{1-x} \right) .
\end{aligned}
\tag{4.2}
$$

This expression is obtained from the sum of loop and contraction diagrams; as is well known (*e.g.*, see [2]), the individual loop diagrams that give the renormalization constants Z_2 or Z_1 in light-front form carry momentum dependence, but the Ward identity guarantees that their sum does not, allowing one to adopt an on-shell renor-

malization scheme in which the input α and m values are given by the physical ones. Since the higher-order corrections not given here must necessarily subtract the $\ln \Lambda$ divergence of Eq. (4.2) but generally produce additional corrections, one may choose to regularize the divergence in a variety of ways. The work of Refs. [163, 1, 174] advocates simply taking $\Delta M^2 = 0$. To gauge the effect of other choices, two choices of subtraction are considered. The first is subtracting from the bracketed term of Eq. (4.2) only the $\ln(\Lambda^2/m^2)$ portion; the second is to subtract the $O[(m^2)^0]$ correction as well. In the latter case, the bound-state eigenvalues M^2 change by less than 1 part in 10^4 by the time Λ_μ is as small as $2m_\mu$. Therefore, the simple choice of $\Delta M^2 = 0$ seems acceptable and will be used for the remainder of this thesis.

It should be noted that the derivation of Eq. (4.2) neglects one diagram, in which the leptons exchange an "instantaneous" photon in the presence of a spectator photon, because it is non-diagonal in the single-lepton spins and momenta, and therefore gives rise to a self-mass correction of the atom that is not just a single-lepton mass renormalization. Certainly, this effect could be included as an $O(\alpha^2)$ perturbative correction, but is neglected as well.

It is hard to imagine why lepton mass renormalization would treat the $^1S_0$ states so differently from the others. This phenomenon was noted as early as Ref. [163]. Since the subsequent work of Ref. [1] improved the numerical quality of the $C = -1$ $^3S_1$ states by the inclusion of the Fock state $|\gamma\rangle$, one might expect the inclusion of $|\gamma\gamma\rangle$ to improve the $C = +1$ $^1S_0$ states. Further work in light-front Yukawa theories have also identified the Fock-space truncation as the origin of divergences in specific states[119, 122, 234, 235, 121].

The effect of the regularization scheme [Eq. (3.23)] developed in Chapter 3 is shown as lines in Figs. 4.1,4.2 with filled square points, and demonstrates a great improvement in the stabilization of the Λ dependence of $^1S_0$ states, with fairly minimal
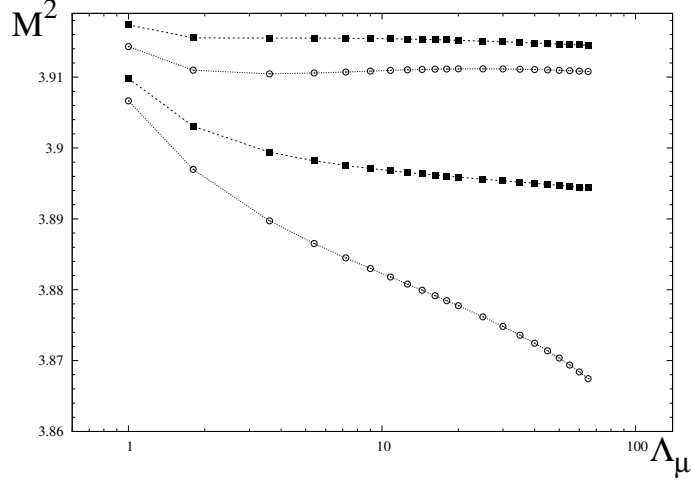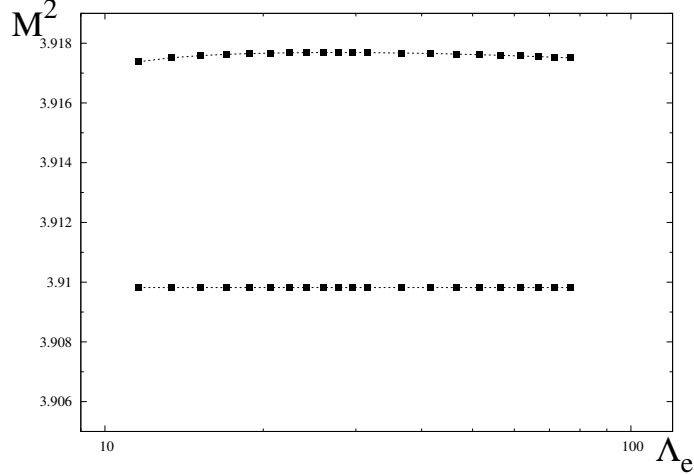
Figure 4.3: Mass eigenvalues of $n = 1$ true muonium states with $J_z = 0$ ($1\,{}^3S_1^0$ at top, $1\,{}^1S_0^0$ at bottom) as a function of cutoff Λ_e in units of the muon Bohr momentum $\alpha m_\mu / 2$, with $\Lambda_\mu = 1$ in these units, $\alpha = 0.3$, $m_e = \frac{1}{2}m_\mu$, $N = 25$.

changes to that of other states. The subtraction for the 2^1S_0 state is not shown in Fig. 4.2, but it amounts to a decrease in the Λ_μ dependence by over a factor of 10.

The sensitivity of the results to varying Λ_e is seen in Fig. 4.3, where the mass eigenvalues of the 1^1S_0 and 1^3S_1 states are reported as functions of Λ_e in units of the muon Bohr momentum $\alpha m_\mu / 2$. That is, $\Lambda_e \simeq 11.6$ corresponds to the value used in Fig. 4.1 and Fig. 4.2. The results are quite insensitive to larger Λ_e, which means that allowing for greater off-shell momentum in the $|e^+e^-\rangle$ sector than in the simple prescription has little impact on the true muonium spectrum. On the other hand, decreasing Λ_e^2 below $\Lambda_\mu^2 + 4(m_\mu^2 - m_e^2)$ (not depicted here) reveals strong fluctuations in the dependence of mass eigenvalues upon Λ_e, which can be attributed to an undersampling of the continuum $|e^+e^-\rangle$ states with invariant mass below the full true muonium bound-state mass.

36

4.1.2 $\Lambda \to \infty$ Limit

Having studied a number of features of the regularization schemes chosen for the model studied, in this part the infinite-Λ limit is studied. As show in the previous section, the regularization of G_2 results in a removal of the strong Λ dependence of all the states. With this choice, it has been found that for the choice $N_\mu = N_\theta = N$, the invariant masses M_n^2 can be well-fit to a function of the form

$$M^2(N, \Lambda) = M_\infty^2(1 + be^{-cN})(1 + de^{-f\Lambda}) \qquad (4.3)$$

for a specific value of α. An example of this fit to a set of data for the triplet state for $\alpha = 0.2$ is shown in Fig. 4.4. The full results for a variety of α for the singlet and triplet state are presented later in Table 4.2. Calculations indicate that the sign of both b and d changes as α is varied. Part of this interesting behavior can be understood as follows. The effective interaction potential has a particular fixed $\boldsymbol{k}_\perp$ dependence, but it is known from non-relativistic quantum mechanics that the wave function's large $\boldsymbol{k}_\perp$ tail is modified as α is varied. For the Coulomb potential with $\alpha \ll 1$, the tail of the wave function approaches $\boldsymbol{k}_\perp^{-4}$[163]. Increasing α has the effect of also increasing the power of the tail. Our results indicate that that this power for $\alpha = 0.3$ is $\approx \boldsymbol{k}_\perp^{-2.5}$.

4.2 Wavefunctions

The motivation of this thesis was to produce the wave functions of true muonium in a boost-invariant way. In Fig. 4.5, the probability density components of a three-flavor calculation of true muonium for a particular set of parameters is shown that was produced using TMSWIFT. With the full wave functions obtained, it is possible to compute important observables, like the production cross section, that are inaccessible from the invariant mass alone. As an example of the additional information that is
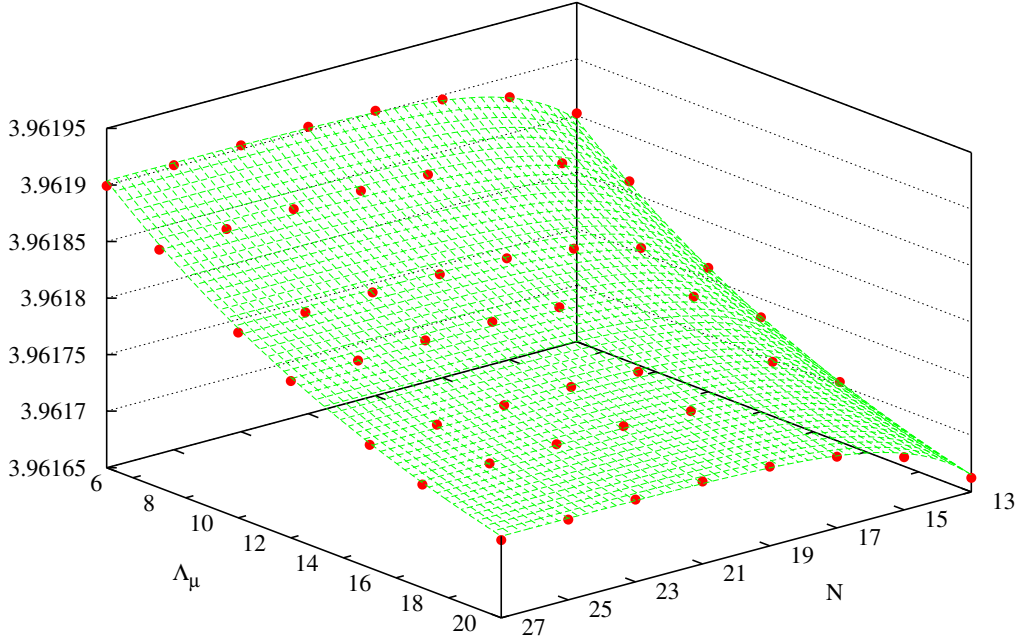
Figure 4.4: Simulations of $1^3S_1^0$ for varying values of Λ_μ and N with $\alpha = 0.2$

accessible from the wave functions, in a later section the decay constants of the singlet and triplet state will be computed.

4.3   Mass Spectrum

Using the modified MESONIX code as discussed above, the entire bound-state spectrum of true muonium and positronium was computed including valence Fock states of both $|\mu^+\mu^-\rangle$ and $|e^+e^-\rangle$ for $J_z = -3, -2, \ldots, +3$ (*e.g.*, Fig. 4.6), taking $\alpha = 0.3$, $m_e = \frac{1}{2}m_\mu$, $\Lambda_\mu = 10\alpha m_\mu/2 \simeq 1.5m_\mu$, and $\Lambda_e = [\Lambda_\mu^2 + 4(m_\mu^2 - m_e^2)]^{1/2} \simeq 15.3\alpha m_\mu/2 \simeq 2.3m_\mu$.
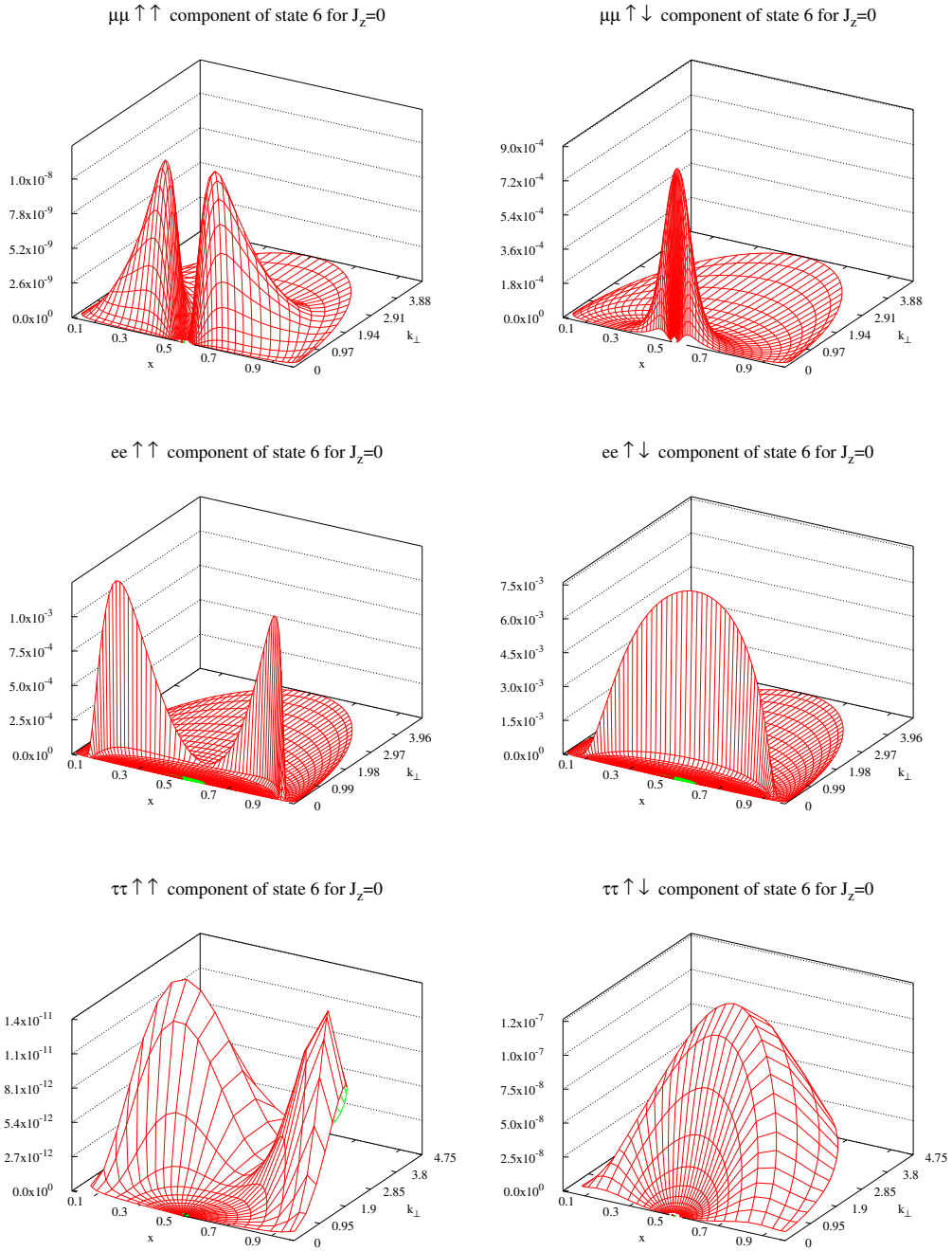
Figure 4.5: The $1^3S_1^0$ probability density of (left) $\uparrow\downarrow$ e^+e^-, (center) $\uparrow\downarrow$ $\mu^+\mu^-$, and (right) $\uparrow\downarrow$ $\tau^+\tau^-$ components of true muonium with $J_z = 0$, as functions of x and $k_\perp$, for $\alpha = 0.3$, $m_e = \frac{1}{2}m_\mu$, $m_\tau = 2m_\mu$, $\Lambda_i = 10\alpha m_i/2$, $N_\mu = N_\tau = 37$, and $N_e = 71$.

From Fig. 4.6, the true muonium spectrum is seen to be nearly identical to that found in [1]. The shifts caused by the inclusion of the e^+e^- sector are smaller than can be resolved in this plot (See Fig. 4.7 for the scale of these contributions). Likewise, the positronium spectrum indicates multiplets with the expected multiplicities and ordering.

4.4   Effect of the $|e^+e^-\rangle$ Sector

Proper inclusion of the front-form Fock states $|e^+e^-\rangle$ and $|e^+e^-\gamma\rangle$ should replicate the physics in instant form due to the inclusion of instant-form diagrams with an e^+e^- pair and a γ, such as vacuum polarization due to electrons in the single-photon annihilation channel (called VP-e-A in Ref. [236]). The importance of including both $|e^+e^-\rangle$ and $|e^+e^-\gamma\rangle$ states in the simulations is twofold.

First, the dominant decay channel for true muonium in $^3S_1$ states is e^+e^- production, while the dominant decay channel for $^1S_0$ ($C = +1$) states is $\gamma\gamma$. Note that the well-known leading-order result for the $^3S_1$-$^1S_0$ hyperfine splitting, $\Delta E = \frac{7}{12}m_\mu\alpha^4$ for true muonium, has been derived analytically in front form [116, 117], so that other physical effects sensitive to small $\mu^+\mu^-$ separation such as $\mu^+\mu^- \to \gamma \to e^+e^-$ should also be considered.

While including the $|e^+e^-\rangle$ state into calculations requires essentially nothing but duplicating the $|\mu^+\mu^-\rangle$ states as $|e^+e^-\rangle$, properly including a $|\gamma\gamma\rangle$ state would require computing many new matrix elements, developing new counterterms to regularize singular integrals, and properly renormalizing the photon mass terms that arise on the light front. The start of this work is discussed in Chapter 5.

Second, Jentschura et $al.$ [236] showed in instant form that VP-e-A is the second-largest correction to the hyperfine splitting in true muonium. The only correction that is larger in instant form arises from vertex corrections, which are partly incorpo-
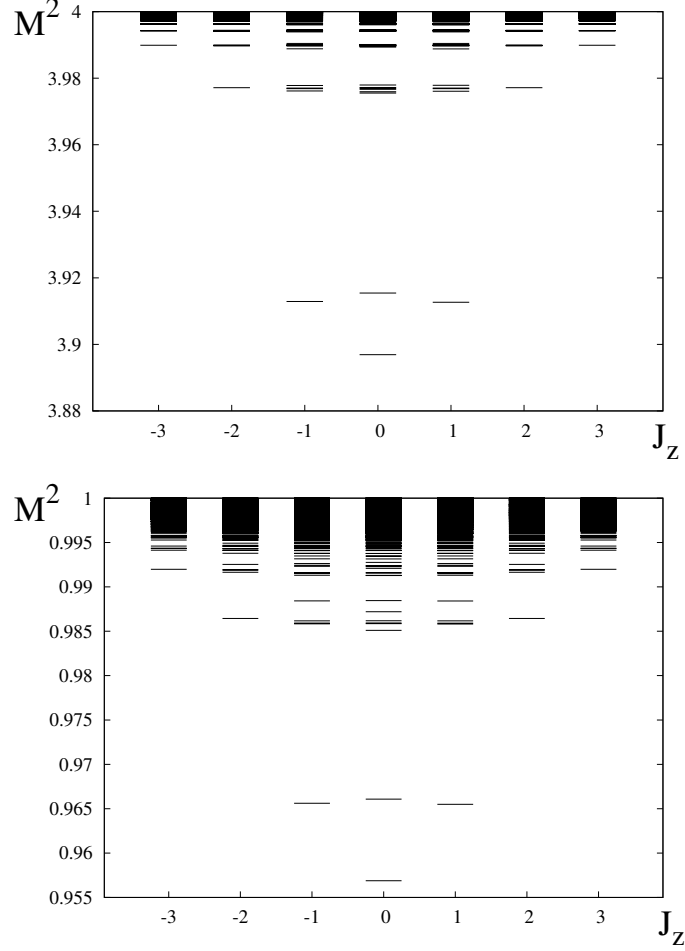
Figure 4.6: Spectrum of (top) true muonium and (bottom) positronium with $J_z = -3, -2, \ldots, +3$. The spectra are calculated using $\alpha = 0.3$, $m_e = \frac{1}{2}m_\mu$, $\Lambda_\mu = 10\alpha m_\mu/2$, $\Lambda_e = [\Lambda_\mu^2 + 4(m_\mu^2 - m_e^2)]^{1/2} \simeq 15.3\alpha m_\mu/2$, $N = 25$. The mass-squared eigenvalues M_n^2 are expressed in units of m_μ^2.

rated in front form through the inclusion of $|\mu^+\mu^-\gamma\rangle$ states, but can be fully treated only through proper renormalization. Furthermore, Ref. [236] finds the energy shifts arising from the $|\gamma\gamma\rangle$ states to be several times smaller than those from either VP-e-A or vertex corrections. The calculations of Ref. [236] rely upon the asymptotic behavior of the vacuum polarization, which for true muonium is the limit of $m_e/m_\mu \ll 1$. In the cases considered here, $m_e/m_\mu = O(1)$, one might expect significant corrections to the asymptotic behavior. To find the effect of these corrections, one can compute the exact correction due to VP-e-A without the asymptotic approximation. As first shown in [237], the leading-order radiative correction to the QED particle-antiparticle bound-state energy spectrum due to a virtual fermion loop coupling to the electromagnetic field with amplitude φ_0 (which, in the nonrelativistic limit, is just the wave function at the origin) is

$$\Delta E_{\text{VP}} = \frac{\pi\alpha}{m_i^2}\left(1 - \frac{4\alpha}{\pi}\right)\bar{\Pi}^R(4m_i^2)|\varphi_0|^2\langle\boldsymbol{S}^2\rangle + O(\alpha^6)$$

$$= \frac{\alpha^4 m_i}{4n^3}\left(1 - \frac{4\alpha}{\pi}\right)\bar{\Pi}^R(4m_i^2) + O(\alpha^6)\,, \qquad (4.4)$$

where m_i is the mass of the bound fermion, $\bar{\Pi}^R(q^2)$ is the renormalized polarization function, and $\boldsymbol{S}^2$ is the total spin Casimir operator. In the second line, the expression has been specialized to the $n\,^3S_1$ state, for which $|\varphi_0|^2 = m_i^3\alpha^3/8\pi n^3$ is the nonrelativistic squared wave function at the origin, and $\langle\boldsymbol{S}^2\rangle = 2$. The exact form of the one-loop vacuum polarization function at $\mathcal{O}(\alpha)$ is

$$\bar{\Pi}^R(q^2) = \frac{\alpha}{3\pi}\left[-\frac{5}{3} - \frac{4m_f^2}{q^2} + \left(1 + \frac{2m_f^2}{q^2}\right)f(q^2)\right]\,, \qquad (4.5)$$

where m_f is the mass of the loop fermions, and the form of $f(q^2)$ depends upon whether q^2 is spacelike or timelike and its size compared to $4m_f^2$. In the region

$4m_f^2 < q^2$, *e.g.*, for true muonium with electron-loop corrections, one finds

$$f(q^2) = \sqrt{1 - \frac{4m_f^2}{q^2}} \ln \left(\frac{1 + \sqrt{1 - \frac{4m_f^2}{q^2}}}{1 - \sqrt{1 - \frac{4m_f^2}{q^2}}} \right) - i\pi \sqrt{1 - \frac{4m_f^2}{q^2}}, \qquad (4.6)$$

where the imaginary term signals the possibility for decay. Inserting Eqs. (4.5)–(4.6) into Eq. (4.4), taking the $m_e \to 0$ limit, and dropping the $O(\alpha^6)$ terms, reproduces Eq. (26) of [236], which is expressed here slightly differently to allow ease of comparison to the front-form calculations:

$$\Delta E_{\mathrm{VP}}(n^3 S_1) = \frac{m_\mu \alpha^5}{4\pi n^3} \left[\frac{1}{3} \ln \left(\frac{4m_\mu^2}{m_e^2} \right) - \frac{5}{9} - \frac{i\pi}{3} \right. $$
$$\left. + O\left(\frac{m_e^2}{4m_\mu^2}, \alpha \right) \right]. \qquad (4.7)$$

In typical cases considered here ($m_e/m_\mu \sim 0.1$–0.8), this expansion predicts relative corrections to the asymptotic form of order 10%, so the complete formulas [Eqs. (4.4)–(4.6)] are retained for the numerical results.

In order to compare these results to those of instant-form perturbation theory calculations, it is easier to compare shifts in M^2:

$$\Delta M^2 \equiv M_{\mu\mu}^2 - M_0^2$$
$$= (2m_\mu + B + \Delta E)^2 - (2m_\mu + B)^2, \qquad (4.8)$$

where $M_{\mu\mu}^2$ is the squared mass of our model true muonium including the $|e^+ e^-\rangle$ component, while M_0^2 is the squared mass neglecting the electron Fock states, ΔE is the total binding energy due to the presence of the $|e^+ e^-\rangle$ states, and B is the remaining binding energy terms of the atom. We examine how well taking $\Delta E = \Delta E_{\mathrm{VP-e-A}}$, where the latter refers to the original instant-form expression of Eq. (4.4), matches the light-front results.

True muonium presents an extremely intriguing physical situation not typically encountered in light-front studies, and particularly not in light-front positronium

43

studies: In the invariant mass range $4m_e^2 < M^2 < 4m_\mu^2$, the $|\mu^+\mu^-\rangle$ component is bound but the $|e^+e^-\rangle$ component forms a continuum. The invariant mass M_S of the $|e^+e^-\rangle$ state satisfies the constraint

$$M_S^2 = \frac{m_e^2 + \boldsymbol{k}_\perp^2}{x(1-x)}, \tag{4.9}$$

but is otherwise unconstrained. Representing such states in the DLCQ formulation presents interesting numerical challenges, analogous to representing band structures in solid-state systems by closely-spaced discrete energy levels. Even so, since the two flavor sectors can only interact through the single-photon annihilation channel, the only true muonium states in this model affected by the inclusion of $|e^+e^-\rangle$ are those with $|J_z| \leq 1$, as seen in Chapter 3. Denoting the bound-state mass-squared eigenvalue before and after including the e^+e^- states as M_0^2 and $M_{\mu\mu}^2$, respectively, Fig. 4.7 plots the magnitudes of the mass shifts $\Delta M^2 \equiv M_{\mu\mu}^2 - M_0^2$ of $J_z = 0$ true muonium states as a function of m_e in the $n = 1, 2, 3$ energy levels.

Although the results may seem noisy in m_e, one must first note that the shifts ΔM^2 are so small that they at no point lead to a level crossing, and moreover, a trend is clearly visible that suggests the shifts decrease quickly with increasing principal quantum number n (approximately as $1/n^3$, see below). For the $J_z = 0$ case, $n\,^3S_1^0$ are the only states affected by the new sector in a numerically significant way, in agreement with front-form predictions [1]. One finds in the $|J_z| = 1$ cases (not plotted here) the P states are also affected, but at a much lower level, and that the mass shifts for states differing only in J_z are not the same, reflecting that rotational invariance in the light-front calculation at finite numerical accuracy is not entirely restored.

The reason for the fluctuations in Fig. 4.7 is just as interesting as the results themselves. As indicated above, the $|e^+e^-\rangle$ continuum states near the $|\mu^+\mu^-\rangle$ bound
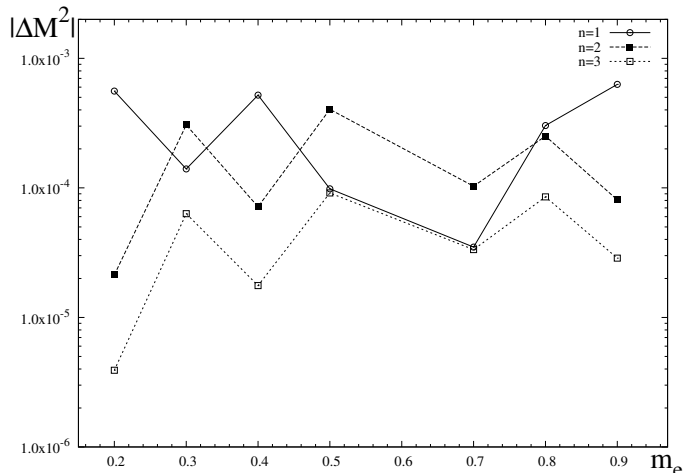
Figure 4.7: Eigenvalue shifts $\Delta M^2 \equiv M_{\mu\mu}^2 - M_0^2$ (in units of m_μ^2) for the $n \leq 3$, $J_z = 0$ triplet states of true muonium as functions of m_e, for $\alpha = 0.3$, $\Lambda_\mu = \alpha m_\mu / 2$, $\Lambda_e = [\Lambda_\mu^2 + 4(m_\mu^2 - m_e^2)]^{1/2} \simeq 11.6\alpha m_\mu / 2$, and values of N are adjusted as described in the text. From top to bottom, the states are $1\,^3S_1^0$, $2\,^3S_1^0$, and $3\,^3S_1^0$.

states, (which lie just below $M^2 = 4m_\mu^2$) are simulated numerically in DLCQ as clusters of discrete energy levels rather than a true continuum. The location in M^2 of these clusters is determined by μ, which to remind the reader has a non-trivial relation to x and $\boldsymbol{k}_\perp$ given by:

$$\frac{m_i^2 + \boldsymbol{k}_\perp^2}{x(1-x)} = 4(\mu^2 + m_i^2)\,. \tag{4.10}$$

The number of such clusters and the size of gaps between them determined are largely by N_μ. The density of energy levels within each cluster is determined by N_θ, but we also note that the spacing of the levels within each cluster is not entirely uniform, being more dense at larger values of M^2.

One might expect that simply increasing the values of N_μ and N_θ in the simulations must eventually suppress the numerical artifacts associated with the discretization. However, for the moderate values (N_μ, $N_\theta < 50$) studied in this work, several features

make the analysis more complicated: First, the larger value of the cutoff Λ_e compared to Λ_μ allows for a substantial phase space to be available to the $|e^+e^-\rangle$ continuum states, only some of which overlap with the $|\mu^+\mu^-\rangle$ bound states, and this issue is exacerbated as Λ_e increases; in other words, only some of the $|e^+e^-\rangle$ clusters overlap with the $|\mu^+\mu^-\rangle$ states, and simply increasing N_μ does not directly alleviate this fact. Related to this point is the nonlinear nature of the mapping used in the numerics,

$$f(\mu) = \frac{1}{1+\mu} , \tag{4.11}$$

which was designed to guarantee a sufficient sampling of points up to $\mu = \frac{\Lambda_e}{2}$, but does not necessarily suitably sample the region near the $|\mu^+\mu^-\rangle$ bound states. It is this highly non-trivial dependence of continuum clusters that has motivated the implementation of multiple discretization schemes into TMSWIFT. This flexibility results in different points being sampled for different methods, allowing tests of observables' dependence on continuum clusters from a different direction than simply increasing N_μ or N_θ.

The discrete sampling of these continuum states has a noticeable effect on the shifts ΔM^2. Quite generally, a given $|\mu^+\mu^-\rangle$ bound state prior to the inclusion of electrons is found to undergo a shift in ΔM^2 toward the energy levels of the $|e^+e^-\rangle$ states in the nearest clusters. Clearly, such an effect is a numerical artifact, since the true $|e^+e^-\rangle$ spectrum is continuous, and the shift can be pronounced if the numerical simulation is such as to produce no cluster of $|e^+e^-\rangle$ states near the original $|\mu^+\mu^-\rangle$ bound state. Only results from simulations in which the $|\mu^+\mu^-\rangle$ state lies within an $|e^+e^-\rangle$ cluster are reported here (clearly this determination requires some subjective determination of what data to include); guaranteeing that this scenario occurs requires a delicate balancing of the parameters m_e, Λ_e, N_μ, and attention to the nature of the mapping function $f(\mu)$. Even in the case that a $|\mu^+\mu^-\rangle$ state lies neatly within an

$|e^+e^-\rangle$ cluster, one must note that not every $|e^+e^-\rangle$ state has the same quantum numbers as the $|\mu^+\mu^-\rangle$ state and can mix with it. All of these effects must be taken into account in understanding the nature of results like Fig. 4.7; nevertheless, the fact remains that broad trends of definite physical significance can still be identified.

For example, the addition of the $|e^+e^-\rangle$ component should lead to a modification of the Lamb shift (by which is meant the sum of all radiative corrections) proportional to a power of the principal quantum number n. While the quantitative values of these shifts show some sensitivity to the inputs, one might expect their ratios for different states for any given set of simulation parameters m_e, Λ_e, and N to be less sensitive. To study the Lamb shift modifications, the ratio of the mass shifts for different n for $^3S_1$ states, $r_{nn'}$, for $n' > n$ is defined via

$$r_{nn'} \equiv \frac{\Delta M_n^2}{\Delta M_{n'}^2} \ . \tag{4.12}$$

Taking the average of $r_{nn'}$ over all m_e values used for the computations, we determine the leading-order dependence $\Delta M_n^2 \propto n^{-\beta}$ from the relation

$$\ln(r_{nn'}) = -\beta \ln\left(\frac{n}{n'}\right) \ . \tag{4.13}$$

The results are presented in Table 4.1. That $\beta \approx 3$ for $^3S_1$ states agrees with instant-form perturbation theory calculations of Lamb shifts [238].

As discussed in above, one can compare the results of the simulations to the predictions of nonrelativistic instant-form results through Eqs.(4.4)–(4.8). Consider, for example, ΔM^2 of $1^3S_1^0$. Even though the individual simulations at particular fixed choices of $N_{\mu,\theta}$ for a given m_e do not rapidly converge to a single fixed value at the moderate values of $N_{\mu,\theta}$ used here, if one restricts to simulations in which the $|\mu^+\mu^-\rangle$ state lies within a $|e^+e^-\rangle$ cluster for the given m_e, the eigenvalue shifts then lie in constrained ranges and one may extract meaningful results by statistically

$^{2S+1}L_J^{J_z}$	β		
n, n'	1, 2	1, 3	2, 3
$^3S_1^0$	2.97 ± 0.09	3.3 ± 0.3	3.3 ± 0.3
$^3S_1^{-1}$	3.2 ± 0.2	3.3 ± 0.2	3.6 ± 0.4

Table 4.1: The exponent β defined in Eq. (4.13) for different states over the range $0.1 \leq m_e/m_\mu \leq 0.9$. Errors are estimated from the variation in m_e and N.

averaging over the results of these simulations, as exhibited in Fig. 4.8. These light-front numerical results are seen in fact to agree fairly well with the instant-form result, with a few important caveats: First, the uncertainties become much larger for the smallest values of m_e (specifically seen in $m_e = 0.2m_\mu$ in Fig. 4.8). Second, the tiny uncertainties at $m_e = 0.5m_\mu$ and $0.7m_\mu$ reflect the accidental tendency of $|e^+e^-\rangle$ clusters to appear in the region of the $1\,^3S_1^0$ $|\mu^+\mu^-\rangle$ state. Moreover, from the formal point of view, the instant-form and light-front calculations have three significant differences.

First, the instant-form result here represents only the real part of the energy shift due to vacuum polarization and ignores, for example, vertex corrections. In front form, all of these effects are combined together when one includes explicit $|e^+e^-\rangle$ and $|e^+e^-\gamma\rangle$ states. Second, vacuum polarization diagrams in instant form contribute to the renormalization of the coupling constant, an effect not taken into account in this simple model. Finally, a result like Eq. (4.7) uses only the simplest expression for the nonrelativistic wave function; instant-form calculations that improve upon the nonrelativistic wave function result appear in, $e.g.$, Refs. [239, 240]. Nevertheless, the level of agreement in Fig. 4.8 is gratifying.
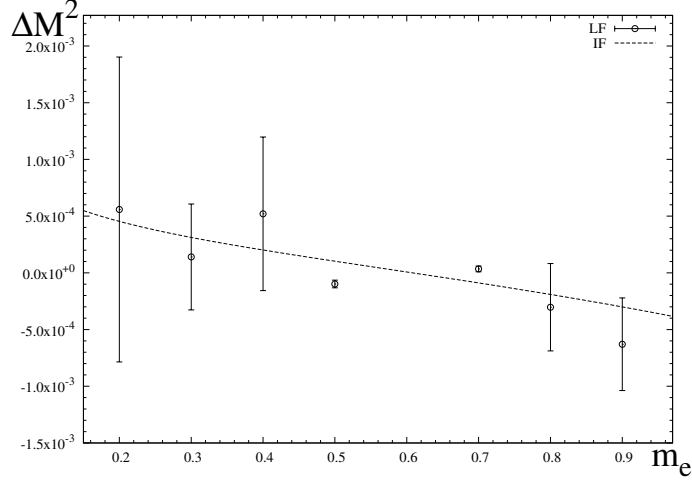
Figure 4.8: Eigenvalue shifts $\Delta M^2 \equiv M_{\mu\mu}^2 - M_0^2$ (in units of m_μ^2) for $1\,^3S_1^0$. The dashed line IF is the instant-form prediction from Eq. (4.8), using the nonrelativistic wave function, while the light-front (LF) points are obtained by taking $\alpha = 0.3$, $\Lambda_\mu = \alpha m_\mu/2$, $\Lambda_e^2 = [\Lambda_\mu^2 + 4(m_\mu^2 - m_e^2)]^{1/2} \simeq 11.6\alpha m_\mu/2$, and averaging over the results using several suitable values of N, as described in the text.

4.5   Decay Constants

Beyond the invariant mass, the decay constants offer an interesting observable that can be extracted from the wave functions. They also serve as an good test bed for understanding how the properties of the wave function are affected by regularization and renormalization. The decay constants in the vector V and pseudoscalar P channels are defined by

$$\langle 0|\bar{\psi}\gamma^\mu\psi|V(p),\lambda\rangle = \epsilon_\lambda^\mu m_V f_V$$

$$\langle 0|\bar{\psi}\gamma^\mu\gamma^5\psi|P(p)\rangle = ip^\mu f_P \tag{4.14}$$

where $e_\lambda^\mu(p)$ is the spin vector for the boson and $\lambda = 0, \pm1$. In front-form field theory, the decay constants can be computed directly from the $+$ components of

these currents, which following Ref. [241, 174] are given for QED bound states by

$$f_{V(P)} = \int \frac{\mathrm{d}x}{\sqrt{x(1-x)}} \frac{\mathrm{d}^2 \boldsymbol{k}_\perp}{(2\pi)^3} \left[\psi_{J_z=0}^J(\boldsymbol{k}_\perp, x, \uparrow\downarrow) \mp \psi_{J_z=0}^J(\boldsymbol{k}_\perp, x, \downarrow\uparrow) \right] \qquad (4.15)$$

where the vector (pseudoscalar) decay constant is given by the difference (sum) of the two terms in the equation. Taking the component wave function from TMSWIFT calculations, it is possible to obtain f_V for the singlet state and f_P for the triplet state as a function of α. Like the invariant masses, the decay constants are found to be well-fit to Eq. (4.3), and therefore an infinite cutoff limit value for them can be obtained. These results can be found in Table 4.2.

4.6 α Dependence

The decreased computational time awarded by TMSWIFT's parallelization allows for computing the α dependence of observables. Focusing on the ground state, the fit-function in Eq. 4.3 was applied to the singlet- and triplet-state invariant mass and decay constant for single-flavor true muonium, which are tabulated in Tab. 4.2 for a range of α.

With these values, it is possible to study the approach to the perturbative regime of α. The leading-order M^2 is given by the Bohr spectrum:

$$M^2 = \left(2m - \frac{m\alpha^2}{4} \right)^2. \qquad (4.16)$$

Since $m_\mu = 1$ in TMSWIFT, to test the agreement of this formula with the singlet and triplet state separately, a fit can be performed to

$$M^2(\alpha) = \left(M_0 + N\alpha^\beta \right)^2. \qquad (4.17)$$

The results of this fit are found in Tab. 4.3.

Comparing the results to the anticipated Bohr spectrum values indicates that, while $\alpha \geq 0.1$ may be too large to trust the leading-order calculation, for both states

Table 4.2: Extrapolated results for the invariant mass squared M^2 in units of m_μ^2 and the decay constants f_V, f_P in units of m_μ for a range of α. The sixth column is the computed hyperfine coefficient C_{HF} from Eq. (4.18). The seventh column is the instant-form prediction for C_{HF} from Eq. (4.19).

α	$M^2(1^1S_0)$	$f_S(1^1S_0)$	$M^2(1^3S_1)$	$f_P(1^3S_1)$	$C_{\text{hf,LF}}$	$C_{\text{hf,ET}}$
0.3	3.8953(4)	$8.54(10) \times 10^{-3}$	3.91607(9)	$3.11(8) \times 10^{-3}$	0.65(2)	0.6735
0.2	3.9575(5)	$3.825(5) \times 10^{-3}$	3.961647(5)	$2.131(4) \times 10^{-3}$	0.65(8)	0.6204
0.1	3.9898788(2)	$1.2669(3) \times 10^{-3}$	3.9901451(5)	$9.76(3) \times 10^{-4}$	0.666(2)	0.5922
0.07	3.99507099(9)	$7.379(2) \times 10^{-4}$	3.9951383(4)	$6.199(8) \times 10^{-4}$	0.701(4)	0.5877
0.05	3.99749231(6)	$4.456(2) \times 10^{-4}$	3.9975107(2)	$3.945(4) \times 10^{-4}$	0.735(6)	0.5855
0.04	3.99839701(3)	$3.1933(4) \times 10^{-4}$	3.99840478(3)	$2.905(4) \times 10^{-4}$	0.759(4)	0.5847
0.03	3.99909908(2)	$2.0777(8) \times 10^{-4}$	3.99910158(2)	$1.942(3) \times 10^{-4}$	0.772(8)	0.5841
0.02	3.999599843(9)	$1.1344(7) \times 10^{-4}$	3.999600344(9)	$1.0864(10) \times 10^{-4}$	0.78(2)	0.5837
0.01	3.999900036(5)	$4.0239(2) \times 10^{-5}$	3.999900067(5)	$3.945(3) \times 10^{-5}$	0.78(15)	0.5834

the fit parameters are in decent agreement. Looking more closely at these results, it can also be seen that the singlet state is approaching the perturbative values from below, while the triplet is approaching them from above, indicating that a hyperfine splitting is produced in these results. One can check the reproduction of the instant-form predictions by considering the hyperfine coefficient, which is defined as

$$C_{\text{HF}} = \frac{E_{\text{HFS}}}{m_\mu \alpha^4} = \frac{\sqrt{M^2(1^3S_1)} - \sqrt{M^2(1^1S_0)}}{m_\mu \alpha^4} \tag{4.18}$$

If there were no Fock-space truncation, then the best comparison to instant form would be the state-of-the-art $\mathcal{O}(\alpha^7)$ instant-form prediction for E_{HFS} found in Ref. [3]. But because of the Fock-state truncation, there is a mismatch in the higher-order contributions. The model considered here should correctly resum relativistic corrections from the single-photon exchange and annihilation diagrams. Therefore in addition to $\mathcal{O}(\alpha^7)$ calculation, the results found here are also compared to the value of C_{HFS}

51

Table 4.3: Fit parameters of Eq. (4.17) for the singlet and triplet states of true muonium as a function of α for two ranges. The leading-order perturbative predictions are $M_0 = 2, N = -\frac{1}{4}, \beta = 2$.

E_n	α	M_0	N	β
1^1S_0	[0.01,0.3]	1.99990(5)	-0.38(2)	2.22(3)
	[0.01,0.1]	1.9999985(8)	-0.263(2)	2.017(3)
1^3S_1	[0.01,0.3]	2.0000004(2)	-0.240(3)	1.989(3)
	[0.01,0.1]	2.00000027(10)	-0.242(2)	1.991(2)

given by the exact Dirac-Coulomb solutions[242]:

$$C_{\mathrm{HF}} = \frac{1}{m_\mu \alpha^4} \left(\frac{E_F}{\sqrt{1 - \alpha^2}[2\sqrt{1 - \alpha^2} - 1]} \right). \tag{4.19}$$

where $E_F = (7/12)m_\mu \alpha^4$ is the Fermi Energy of true muonium, but the full annihilation channel hasn't been resummed. The comparison is found graphically in Figure 4.9, and numerical results are found for the Dirac-Coulomb solutions in Table. 4.2.

Clearly, the there is a large amount of disagreement between the two instant-form predictions and the results on the light-front. Further, the agreement seems to worsen with decreased α. Previously, many authors[160, 163, 1] have pointed out that the correct value of the HFS is found for $\Lambda \approx m\alpha$, and the results from TMSWIFT agree with this point of view. Unfortunately, the divergences spoil this agreement at larger Λ, necessitating renormalization. How this occurs can be understood thusly: although the regularization procedure developed in Chapter 3 allows for extrapolation to $\Lambda \to \infty$, the Λ dependences of the singlet and triplet states are different, as can be seen in Fig. 4.1, leading to an asymptotic HFS that disagrees. Additionally, why
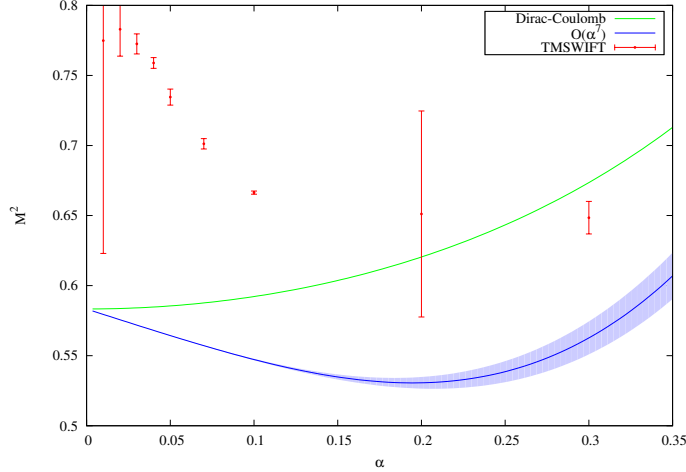
Figure 4.9: C_{HF} as a function of α compared to the Dirac-Coulomb solution (green line) and the $\mathcal{O}(\alpha^7)$ instant form prediction (blue line) of [3]. The error in the computed values is only from fitting, while the error in the instant-form calculation is estimated by an $\mathcal{O}(\alpha^8)$ correction with coefficient 1.

there is an α dependence of C_{HFS} might seem strange at first. But, as has been alluded to before, this seems to be related to the changing large-$\boldsymbol{k}_\perp$ tail of the wave function. Before discussing the wave functions though, the decay constants can check the perturbative limit by comparing the results of the approach to the anticipated form. For the decay constants, $f_i \propto |\psi(0)|/M_i^2$, indicating a $\alpha^{3/2}$ power law at leading order. To check this prediction, a fit is performed to the function

$$f_i(\alpha) = N\alpha^\beta \tag{4.20}$$

and the results are found in Tab. 4.4. Similar to the invariant masses, the decay constants seem to reproduce the perturbative form, with values of $\alpha > 0.1$ still indicating a larger discrepancy.

Table 4.4: Fit parameters of Eq. (4.20) for the vector decay constant of the singlet state and the pseudoscalar decay constant of the triplet state for two ranges of α. The leading-order perturbative prediction is $\beta = 3/2$.

f_i	α	N	β
f_S	[0.01,0.3]	0.0396(3)	1.496(2)
	[0.01,0.1]	0.0395(2)	1.4959(9)
f_P	[0.01,0.3]	0.021(3)	1.35(3)
	[0.01,0.1]	0.028(2)	1.42(2)

INCLUDING THE $|\gamma\gamma\rangle$ STATE

For a more accurate model, two critical sets of Fock states are the most urgently
needed to be included: $|\gamma\gamma\rangle$, which dominates the decay of singlet states of true muo-
nium (and in particular should have a pronounced effect on ${}^1S_0$ wave functions), and
the states $|\ell^+\ell^-\ell'^+\ell'^-\rangle$ (where $\ell \neq \ell'$ are allowed), which provide crucial contributions
to the vacuum polarization corrections and insure the gauge invariance of the $|\gamma\gamma\rangle$
Fock state. In this chapter, a derivation of the effective interaction between the $|\gamma\gamma\rangle$
state and the $|\ell^+\ell^-\rangle$ will be performed. This chapter starts with a development of the
notation needed to perform these calculations and understand the diagrams. Next,
the full set of diagrams in the $|\gamma\gamma\rangle$ sector are combined to yield an integral equation.
Finally, the set of diagrams in the $|\ell^+\ell^-\ell'^+\ell'^-\rangle$ sector needed to regain gauge invari-
ance is derived. In the concluding section, the remaining work in this on-going effort
is discussed.

For the complete calculation, there are 19 time-ordered diagrams that need to be
computed. All of them correspond to Fig 5.1 with different time orderings with 0,1,
or 2 instantaneous particles.
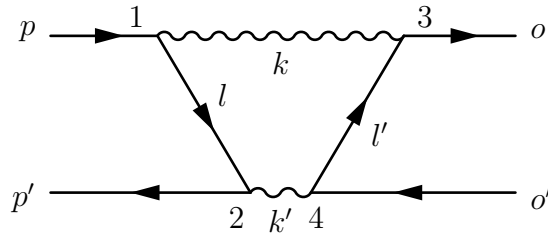
Figure 5.1: $|\gamma\gamma\rangle$ intermediate state contribution to the interaction.

In order to succinctly denote the diagrams that need to be computed, the following convention is used throughout this chapter. Since all diagrams have the same vertices, each vertex is assigned a number (e.g., 1,2,3,4), as in Fig 5.1. Since the diagrams must have time-ordered vertices, each diagram is labeled by a four-digit number determined by the order in which the vertices are time ordered. For example, Fig. 5.1 would be defined as 1243. In addition, the notation is used that a pair of numbers in parenthesis indicates an instantaneous interaction (e.g. Fig. 5.2 would be labeled 1(24)3).
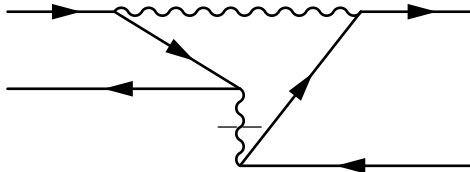
Figure 5.2: 1(24)3: A diagram with an instantaneous particle, in this case a photon

Additionally, the same labels are used for the momenta in all diagrams: p and p' indicate incoming momenta, o and o' indicate outgoing momenta, k and k' indicate the photon momentum, and l and l' indicate internal fermion momenta. For diagrams where the internal lines are anti-fermions, e.g. 2134, we will use the momenta n and n' although as will be shown below, these momenta are easily related to l and l'.

5.1   Computing the $|\gamma\gamma\rangle$ Elements

To begin, the 11 uncrossed diagrams will be computed that contain either two dynamical photons or singly-instantaneous particle diagrams that either involve two dynamical photons or are needed to cancel terms arising from them. In the case of the singly-instantaneous diagrams, there is a natural decomposition into the diagrams including instantaneous photons and instantaneous fermions which we will treat in separate subsections.

5.1.1 Fully Dynamical Diagrams

As a warmup, the simplest set of diagrams consist of the fully dynamical diagrams, in which none of the internal lines are instantaneous. These diagrams are 1243, 2143, 1234, 2134. Starting with 1243, the rules found in Appendix C from Ref. [2] are applied, and this diagram can be expressed as

$$
\begin{aligned}
V_{1243} = \int_k \int_{k'} \int_l \int_{l'} & \theta(k^+)\theta((k')^+)\theta(l^+)\theta((l')^+)\delta^3(P-k-k')\delta^3(P-k-l-p') \\
& \times \delta^3(P-k-l'-o')\left(\frac{e}{\sqrt{2}(2\pi)^{3/2}}\right)^4 \\
& \times \frac{\bar{u}_1 \not{\epsilon}_7 u_5}{\sqrt{k^+p^+l^+}} G_{\ell+\ell-\gamma} \frac{\bar{u}_5 \not{\epsilon}_8 v_2}{\sqrt{(k')^+(p')^+l^+}} G_{\gamma\gamma} \frac{(-\bar{v}_4)\not{\epsilon}_8^* u_6}{\sqrt{(k')^+(o')^+(l')^+}} G'_{\ell+\ell-\gamma} \frac{\bar{u}_6 \not{\epsilon}_7^* u_3}{\sqrt{k^+o^+(l')^+}}
\end{aligned}
$$

(5.1)

In this expression, a number of nonstandard notation has been employed.First, integral measures are given by

$$
\int_k \equiv \int \mathrm{d}^2 k_\perp \mathrm{d}k^+.
$$

(5.2)

To express three-component momentum conservation, the abbreviation used is

$$
\delta^3(P) = \delta(P^+)\delta(\boldsymbol{P}_\perp).
$$

(5.3)

Further, the non-perturbative propagators G_i have been introduced like those used for the exchange and annihilation channels in the vein of Ref. [226], and that will be defined by including the necessary terms such that the instantaneous diagrams are canceled. Collecting all the prefactors, summing over the internal propagators, and using the delta functions, we can simplify this expression to

$$
\begin{aligned}
V_{1243} = \int_k & \Theta_k \Theta_{-k} \Theta_p \Theta_o \\
& \times \left(\frac{e}{\sqrt{2}(2\pi)^{3/2}}\right)^4 \frac{-G_{\ell+\ell-\gamma}G_{\gamma\gamma}G'_{\ell+\ell-\gamma}}{\sqrt{p^+o^+(o')^+(p')^+}} \frac{\bar{u}_1\gamma^\mu(\not{l}+m)\gamma^\sigma v_2 \bar{v}_4 \gamma^\rho(\not{l}'+m)\gamma^\nu u_3}{|k^+||P^+-k^+||p^+-k^+||o^+-k^+|} d_{\mu\nu} d_{\sigma\rho},
\end{aligned}
$$

(5.4)

Since time-ordered perturbation theory will always result in the use of step functions, the compact theta functions are defined as

$$\Theta_k = \theta(k^+), \tag{5.5}$$

$$\Theta_{-k} = \theta((P-k)^+), \tag{5.6}$$

where P^+ is the total $+$ component at any time. For terms that involve the external momenta,

$$\Theta_{\pm i} = \theta(\pm(i-k)^+), \tag{5.7}$$

$$\Theta_{i-j} = \theta((i-k)^+)\theta(-(j-k)^+), \tag{5.8}$$

where k is always the k^μ photon's $+$ component. The photon polarization sums are given by

$$d_{\mu\nu}(k) = -g_{\mu\nu} + \frac{\eta_\mu k_\nu + \eta_\mu k_\nu}{k^+}, \tag{5.9}$$

where η^μ has been defined in Appendix A and l, l' are no longer independent variables, but instead defined by

$$l^\mu = \eta^\mu \frac{L_{17} + L_{28}}{4} + \frac{p^\mu - k^\mu - (p')^\mu + (P-k)^\mu}{2}, \tag{5.10}$$

$$(l')^\mu = \eta^\mu \frac{L'_{84} + L'_{73}}{4} + \frac{(P-k)^\mu - (o')^\mu + o^\mu - k^\mu}{2}, \tag{5.11}$$

where $\tilde{l}$ is defined as the second term in these expressions and the L_{ij} terms are defined by

$$L_{ij} = l^- - (i^- - j^-). \tag{5.12}$$

As a final piece of notation for the future, a slightly different propagator is defined:

$$\Delta_i = \left(\frac{e}{\sqrt{2}(2\pi)^{3/2}}\right)^4 \frac{G_i}{\sqrt{p^+ o^+ (o')^+ (p')^+}}, \tag{5.13}$$

where $i = \gamma\gamma, 4\ell, 0$ is an index indicating the sector, and 0 indicates neither of the two sectors. $G_0 = 1$ appears for diagram with instantaneous terms. The other three

dynamical diagrams can be obtained by exchanging $l \leftrightarrow n$ and $l' \leftrightarrow n'$ because the time-ordered diagrams with fermions and antifermions are different. To see how these diagrams differ from 1243, we can consider 2134 (Fig. 5.3). Writing out the
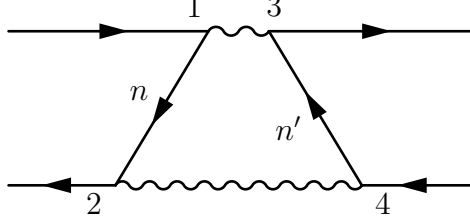
Figure 5.3: 2134, an alternative time ordering

diagram, it is found that to exchange the internal fermion propagators for anti-fermion propagators ,$u_i \bar{u}_i \rightarrow -v_i \bar{v}_i$ is required. With this substitution, the n, n'-dependent delta functions are

$$\propto \delta^3(P - p - k' - n)\delta^3(P - o - k' - n'). \tag{5.14}$$

From these constraints, the momentum relations $n^\mu = [p' - k']^\mu$ and $(n')^\mu = [o' - k']^\mu$ are found, where the notation such as $[p - k]^\mu$ indicates that the momenta inside the brackets must be treated together in the $-$ component. Using the remaining delta functions and the external particle conditions, it is found that $n^\mu = -l^\mu$, so any exchange of a fermion for antifermion in the numerator results in $(\slashed{l} + m) \rightarrow (\slashed{n} - m) = -(-\slashed{l} - m)$, therefore the numerator remains unchanged. Further, since the denominators are always absolute values of momenta, they remain unchanged as well. Using the relations derived, a change the variables in the theta functions can also be performed. Using all of these properties, diagram 2134 is given by

$V_{2134} =$

$$\int_k \Theta_k \Theta_{-k} \Theta_{-p} \Theta_{-o}(-G_{\ell^+\ell^-\gamma}\Delta_{\gamma\gamma}G'_{\ell^+\ell^-\gamma})\frac{\bar{u}_1\gamma^\mu(\slashed{l} + m)\gamma^\sigma v_2 \bar{v}_4\gamma^\rho(\slashed{l}' + m)\gamma^\nu u_3}{|k^+||P^+ - k^+||p^+ - k^+||o^+ - k^+|}d_{\mu\nu}d_{\sigma\rho}.$$

$$\tag{5.15}$$

59

Comparing Eqs. (5.4) and (5.15), it is seen that the effect of exchanging an internal fermion for antifermion in time ordered front-form diagrams is an exchange of $\theta(l^+)$ for $\theta(-l^+)$, as might be anticipated from the necessary agreement with instant form calculations. With this property, the sum of the fully dynamical diagrams 1234, 1243, 2143, and 2134 removes the positivity restrictions on l^+ and $(l')^+$, yielding a final result for the dynamical diagrams

$$V_{dyn} = \int_k \Theta_k \Theta_{-k} (-G_{\ell+\ell-\gamma} \Delta_{\gamma\gamma} G'_{\ell+\ell-\gamma}) \frac{\bar{u}_1 \gamma^\mu (\displaystyle{\not}l + m) \gamma^\sigma v_2 \bar{v}_4 \gamma^\rho (\displaystyle{\not}l' + m) \gamma^\nu u_3}{|k^+||P^+ - k^+||p^+ - k^+||o^+ - k^+|} d_{\mu\nu} d_{\sigma\rho},$$

(5.16)

where the reader is reminded that l^μ and $(l')^\mu$ are not free variables, but defined by Eqs. (5.10) and (5.11).

5.1.2 Singly-Instantaneous Fermion Diagrams

There are four singly-instantaneous fermion diagrams: (12)34, (12)43, 12(34), and 21(34). From the results of the previous section, it can be anticipated that summing each pair should result in the removal of the positivity restriction on the dynamical fermion, so only two example diagrams, (12)34 and 12(34), need be studied. For diagram (12)34:

$$S_{(12)34} = \int_k \int_{k'} \int_{n'} \theta(k^+)\theta((k')^+)\theta((n')^+)\delta^3(P - k - k')\delta^3(P - k' - n' - o)$$
$$\frac{1}{2}\Delta_{\gamma\gamma} G'_{\ell+\ell-\gamma} \frac{\bar{u}_1 {\not}\epsilon_7 \gamma^+ {\not}\epsilon_7 v_2 (-\bar{v}_4){\not}\epsilon_8^* v_6 (-\bar{v}_6){\not}\epsilon_7^* u_3}{|k^+||(k')^+||(p-k)^+||(n')^+|}.$$

(5.17)

Summing over the internal propagators, using the delta functions and the external particle conditions, the diagram simplifies to

$$S_{(12)34} = \int_k \Theta_k \Theta_{-k} \Theta_{-o} \frac{1}{2}(-\Delta_{\gamma\gamma} G'_{\ell+\ell-\gamma}) \frac{\bar{u}_1 \gamma^\mu \gamma^+ \gamma^\sigma v_2 \bar{v}_4 \gamma^\rho (\displaystyle{\not}l' + m)\gamma^\nu u_3}{|k^+||(P-k)^+||(p-k)^+||(o-k)^+|} d_{\mu\nu} d_{\sigma\rho}.$$

(5.18)

Adding in the second diagram, (12)43, the final result for the singly-early instantaneous fermion diagrams is

$$S_{early} = \int_k \Theta_k \Theta_{-k} \frac{1}{2} (-\Delta_{\gamma\gamma} G'_{\ell+\ell-\gamma}) \frac{\bar{u}_1 \gamma^\mu \gamma^+ \gamma^\sigma v_2 \bar{v}_4 \gamma^\rho (\slashed{l}' + m) \gamma^\nu u_3}{|k^+||(P-k)^+||(p-k)^+||(o-k)^+|} d_{\mu\nu} d_{\sigma\rho}. \quad (5.19)$$

Using the exact same process as for the previous diagrams, the expression for the singly-late instantaneous-fermion diagrams can be worked out:

$$S_{late} = \int_k \Theta_k \Theta_{-k} \frac{1}{2} (-G_{\ell+\ell-\gamma} \Delta_{\gamma\gamma}) \frac{\bar{u}_1 \gamma^\mu (\slashed{l} + m) \gamma^\sigma v_2 \bar{v}_4 \gamma^\rho \gamma^+ \gamma^\nu u_3}{|k^+||(P-k)^+||(p-k)^+||(o-k)^+|} d_{\mu\nu} d_{\sigma\rho}. \quad (5.20)$$

5.1.3 Singly-Instantaneous Photon Diagrams

For the case of the instantaneous-photon diagrams in the $|\gamma\gamma\rangle$ sector, there are only two diagrams: 2(13)4 and 1(24)3 (the latter seen in Fig. 5.2). Due to this similarity in these two graphs with the previous worked out examples, the expressions are stated without proof. For the first diagram,

$$S_{2(13)4} = \int_k \Theta_k \Theta_p \Theta_o \Delta_0 G_{e^+e^-\gamma} G'_{e^+e^-\gamma} \frac{\bar{u}_1 \gamma^\mu (\slashed{l} + m) \gamma^+ v_2 \bar{v}_4 \gamma^+ (\slashed{l}' + m) \gamma^\nu u_3}{|k^+||(P-k)^+|^2|(p-k)^+||(o-k)^+|} d_{\mu\nu}. \quad (5.21)$$

For diagram 1(24)3, it should be noted that both internal fermions are exchanged for anti-fermions, and the momentum k is not involved in the problem. To facilitate the cancellations in defining G_i, the momentum $k^\mu = [P - k']^\mu$ is defined as it would be for a dynamical photon. A change of variables in the integral via $\mathrm{d}^3(\mathrm{k}') = -\mathrm{d}^3\mathrm{k}$ is then performed, all the k' terms shift, and the diagram is given by

$$S_{1(24)3} = -\int_k \Theta_{-k} \Theta_{-p} \Theta_{-o} \Delta_0 G_{e^+e^-\gamma} G'_{e^+e^-\gamma} \frac{\bar{u}_1 \gamma^+ (\slashed{l} + m) \gamma^\sigma v_2 \bar{v}_4 \gamma^\rho (\slashed{l}' + m) \gamma^+ u_3}{|(P-k)^+||(k)^+|^2|(p-k)^+||(o-k)^+|} d_{\sigma\rho}.$$
$$(5.22)$$

5.1.4 Doubly-Instantaneous Fermion Diagrams

Only one uncrossed doubly-instantaneous fermion diagram exists: (12)(34), and it can trivially be seen to be

$$S_{(12)(34)} = \int_k \Theta_k \Theta_{-k} \frac{1}{4} (-\Delta_{\gamma\gamma}) \frac{\bar{u}_1 \gamma^\mu \gamma^+ \gamma^\sigma v_2 \bar{v}_4 \gamma^\rho \gamma^+ \gamma^\nu u_3}{|k^+||(P-k)^+||(p-k)^+||(o-k)^+|} d_{\mu\nu} d_{\sigma\rho}. \quad (5.23)$$

61

5.1.5 Full Expression

Summing Eqs. (5.16), (5.19), (5.20), (5.21), (5.22), and (5.23), a full expression for the $|\gamma\gamma\rangle$ sector is obtained. With a few rearrangements, the cancellations of the γ^+ components can be made more obvious. Noting that any term of the form $\gamma^+\gamma^+ = 0$, the freedom exists to add terms with both an instantaneous fermion and photon since these will always vanish. The full expression before solving for the G_i's is then

$$H_{\gamma\gamma} =$$

$$\int_k (-\Delta_{\gamma\gamma} G_{\ell^+\ell^-\gamma} G'_{\ell^+\ell^-\gamma}) \frac{\bar{u}_1 \gamma^\mu \left(\not{l} + m + \frac{\gamma^+}{2G_{\ell^+\ell^-\gamma}} \right) \gamma^\sigma v_2 \bar{v}_4 \gamma^\rho \left(\not{l}' + m + \frac{\gamma^+}{2G'_{\ell^+\ell^-\gamma}} \right) \gamma^\nu u_3}{|k^+||P^+ - k^+||p^+ - k^+||o^+ - k^+|}$$

$$\times \left(d_{\mu\nu} d_{\sigma\rho} \Theta_k \Theta_{-k} + \frac{\eta_{\mu\nu} d_{\sigma\rho}}{G_{\gamma\gamma}|k^+|} \Theta_k \Theta_{-p} \Theta_{-o} - \frac{d_{\mu\nu} \eta_{\sigma\rho}}{G_{\gamma\gamma}|(P-k)^+|} \Theta_{-k} \Theta_p \Theta_o \right). \tag{5.24}$$

5.2 Computing the $|\ell\bar{\ell}\ell\bar{\ell}\rangle$ Elements

In order to construct a fully gauge-invariant interaction, it is anticipated that the non-vacuum polarization interactions in the $|\ell^+\ell^-\ell^+\ell^-\rangle$ sector must be included in the calculations. Furthermore, whereas the $|\gamma\gamma\rangle$ sector allowed for the internal lines to both be fermion or anti-fermion, the $|\ell^+\ell^-\ell^+\ell^-\rangle$ sector restricts the internal lines to be one fermion and one anti-fermion. Due to these restrictions, there are only 8 uncrossed diagrams: the fully dynamical (1324 and 2413), the singly-instantaneous photon ((13)24, 24(13), (24)13, and 13(24)), and the doubly-instantaneous photons ((24)(13) and (13)(24)).

Similar to the way in which the four dynamical diagrams in the $|\gamma\gamma\rangle$ sector combine to remove the step function constrains internal momenta, the sum of the two dynamical diagrams in the $|\ell^+\ell^-\ell^+\ell^-\rangle$ sector will be shown to remove some of the constraints. To show how this diagram can be worked out, it is best to start by investigating diagram 1324. Following the Feynman rules, this diagram is expressed

by

$$
V_{1324} = \int_k \int_{k'} \int_l \int_{n'} \theta(k^+)\theta((k')^+)\theta(l^+)\theta((n')^+)
$$

$$
\delta^3(P - p' - l - n' - o)\delta^3(P - p' - l - k)\delta^3(P - o - n' - k')
$$

$$
\times (-G_{\ell+\ell-\gamma}\Delta_{4\ell}G'_{\ell+\ell-\gamma})\frac{\bar{u}_1\gamma^\mu(\slashed{l} + m)\gamma^\sigma v_2 \bar{v}_4 \gamma^\rho(-\slashed{n}' + m)\gamma^\nu u_3}{|k^+||(k')^+||l^+||(n')^+|}d_{\mu\nu}d_{\sigma\rho}. \quad (5.25)
$$

Using the last two delta functions delivers the momentum relations: $l^\mu = [p - k]^\mu$, and $(n')^\mu = [(o') - (k')]^\mu$ as before. With these, the final two step functions become

$$
\theta((p - k)^+)\theta((o' - k')^+). \quad (5.26)
$$

Then, from the external-particle conditions, the remaining delta function can be rewritten as

$$
\delta^3(P - p' - l - n' - o) = \delta^3(-P + k + k'). \quad (5.27)
$$

Using these expressions, performing the integration over k' leads to the final expression for 1324. Noting that, as in the $|\gamma\gamma\rangle$ sector, the exchange of a fermion for an anti-fermion only changes the step functions, the sum of the dynamical diagrams can be written as

$$
V_{dyn} = \int_k \Theta_k \Theta_{-k} \left(\Theta_p \Theta_{-o} + \Theta_{-p} \Theta_o \right) (-G_{\ell+\ell-\gamma}\Delta_{4\ell}G'_{\ell+\ell-\gamma})
$$

$$
\times \frac{\bar{u}_1\gamma^\mu(\slashed{l} + m)\gamma^\sigma v_2 \bar{v}_4 \gamma^\rho(\slashed{l}' - m)\gamma^\nu u_3}{|k^+||(P - k)^+||(p - k)^+||(o - k)^+|}d_{\mu\nu}d_{\sigma\rho}. \quad (5.28)
$$

5.2.1 Singly-Instantaneous Photon Diagrams

In this section, work is begun by explicitly working out diagram (13)24. For this diagram, the k-momentum photon is instantaneous and it is created and annihilated before the creation of the k'-photon. This diagram is expressed by

$$
F_{(13)24} = \int_{k'} \int_l \int_{n'} \theta(l^+)\theta((n')^+)\theta((k')^+)\delta^3(P - l - n' - p' - o)\delta^3(P - n' - k' - o)
$$

$$
\times \Delta_{4\ell}G'_{\ell+\ell-\gamma}\frac{\bar{u}_1\gamma^+(\slashed{l} + m)\gamma^\sigma v_2 \bar{v}_4 \gamma^\rho(-\slashed{n}' + m)\gamma^+ u_3}{|(l - p)^+|^2|l^+||(n')^+||(k')^+|}d_{\sigma\rho}. \quad (5.29)
$$

63

Integrating over the internal fermions, and applying the shifts $(k')^\mu = [P - k]^\mu$ and $(n')^\mu = -(l')^\mu$ as before,

$$F_{(13)24} = \int_k \Theta_{-k}\Theta_p\Theta_{-o}(-\Delta_{4\ell}G'_{\ell+\ell-\gamma})\frac{\bar{u}_1\gamma^+(\slashed{l} + m)\gamma^\sigma v_2\bar{v}_4\gamma^\rho(\slashed{l}' + m)\gamma^+u_3}{|k^+|^2|(p - k)^+||(o - k)^+||(P - k)^+|}d_{\sigma\rho}. \quad (5.30)$$

In analogy with the previous sections, to obtain the diagram 24(13), where the instantaneous k photon occurs after the annihilation of the k' photon, exchanging $G'_{\ell+\ell-\gamma} \to G_{\ell+\ell-\gamma}$ and take flip the sign inside the Θ_p and Θ_{-o} allows one to arrive at the sum of the two diagrams of:

$$F_{inst-k} = \int_k \Theta_{-k}\left(G'_{\ell+\ell-\gamma}\Theta_p\Theta_{-o} + G_{\ell+\ell-\gamma}\Theta_{-p}\Theta_o\right)(-\Delta_{4\ell})$$
$$\times \frac{\bar{u}_1\gamma^+(\slashed{l} + m)\gamma^\sigma v_2\bar{v}_4\gamma^\rho(\slashed{l}' + m)\gamma^+u_3}{|k^+|^2|(p - k)^+||(o - k)^+||(P - k)^+|}d_{\sigma\rho}. \quad (5.31)$$

For the other two singly-instantaneous photon diagrams, 13(24) and (24)13, analogous results are obtained, without requiring the change of variables from k' to k. Working through these diagrams, the final result is:

$$F_{inst-k'} = \int_k \Theta_k\left(G'_{\ell+\ell-\gamma}\Theta_{-p}\Theta_o + G_{\ell+\ell-\gamma}\Theta_p\Theta_{-o}\right)\Delta_{4\ell}$$
$$\times \frac{\bar{u}_1\gamma^\mu(\slashed{l} + m)\gamma^+v_2\bar{v}_4\gamma^+(\slashed{l}' + m)\gamma^\nu u_3}{|(P - k)^+|^2|k^+||(p - k)^+||(o - k)^+|}d_{\mu\nu}. \quad (5.32)$$

5.2.2 Doubly-Instantaneous Photon Diagrams

There are two doubly-instantaneous photon diagrams, corresponding to the two time orderings that the instantaneous photons can have. For the instantaneous-k photon first, the diagram is $(13)(24)$, whereas for the instantaneous-k' photon first, the diagram is $(24)(13)$. Working with this diagram first,

$$F_{(24)(13)} = \int_n \int_{l'} \theta(n^+)\theta((l')^+)\delta^3(P - l' - n - p - o')$$
$$\times (-\Delta_{4\ell})\frac{\bar{u}_1\gamma^+(-\slashed{n} + m)\gamma^+v_2\bar{v}_4\gamma^+(\slashed{l}' + m)\gamma^+u_3}{|(l')^+||n^+||(p' - n)^+|^2|(o - l')^+|^2}. \quad (5.33)$$

Integrating over n allows for a change of variables $(l')^\mu \to [o - k]^\mu$. Using this substitution, the differential is $\mathrm{d}^3(l') = -\mathrm{d}^3\mathrm{k}$. As a final change, applying the external on-shell particle condition to leads to

$$F_{(24)(13)} = \int_k \Theta_{-p}\Theta_o \Delta_{4\ell} \frac{\bar{u}_1\gamma^+(\slashed{l} + m)\gamma^+ v_2 \bar{v}_4 \gamma^+(\slashed{l}' + m)\gamma^+ u_3}{|(P-k)^+|^2|k^+|^2|(p-k)^+||(o-k)^+|}. \tag{5.34}$$

The other diagram is trivially obtained by again exchanging internal fermions for anti-fermions, so for the sum of the doubly-instantaneous photon diagrams is obtained:

$$F_{(24)(13)} = \int_k \left(\Theta_{-p}\Theta_o + \Theta_p\Theta_{-o}\right) \Delta_{4\ell} \frac{\bar{u}_1\gamma^+(\slashed{l} + m)\gamma^+ v_2 \bar{v}_4 \gamma^+(\slashed{l}' + m)\gamma^+ u_3}{|(P-k)^+|^2|k^+|^2|(p-k)^+||(o-k)^+|}. \tag{5.35}$$

5.2.3 Full Expression

Putting together Eqs. (5.28), (5.31), (5.32),and (5.35), the full $|4\ell\rangle$ sector expression is

$$\begin{aligned}
H_{4\ell} = \int_k &\left(-\Delta_{4\ell}G_{\ell+\ell-\gamma}G'_{\ell+\ell-\gamma}\right) \frac{\bar{u}_1\gamma^\mu(\slashed{l} + m)\gamma^\sigma v_2 \bar{v}_4 \gamma^\rho(\slashed{l}' - m)\gamma^\nu u_3}{|k^+||(P-k)^+||(p-k)^+||(o-k)^+|} \\
&\times \left(\left[d_{\mu\nu}d_{\sigma\rho}\Theta_k\Theta_{-k} + \frac{\eta_{\mu\nu}d_{\sigma\rho}}{G_{\ell+\ell-\gamma}|k^+|} - \frac{d_{\mu\nu}\eta_{\sigma\rho}}{G'_{\ell+\ell-\gamma}|(P-k)^+|}\right.\right. \\
&\qquad\left.- \frac{\eta_{\mu\nu}\eta_{\sigma\rho}}{G_{\ell+\ell-\gamma}G'_{\ell+\ell-\gamma}|(P-k)^+||k^+|}\right]\Theta_p\Theta_{-o} \\
&\quad+ \left[d_{\mu\nu}d_{\sigma\rho}\Theta_k\Theta_{-k} + \frac{\eta_{\mu\nu}d_{\sigma\rho}}{G'_{\ell+\ell-\gamma}|k^+|} - \frac{d_{\mu\nu}\eta_{\sigma\rho}}{G_{\ell+\ell-\gamma}|(P-k)^+|}\right. \\
&\qquad\left.\left.- \frac{\eta_{\mu\nu}\eta_{\sigma\rho}}{G_{\ell+\ell-\gamma}G'_{\ell+\ell-\gamma}|(P-k)^+||k^+|}\right]\Theta_{-p}\Theta_o\right). \tag{5.36}
\end{aligned}$$

5.3 Discussion

Eqs. (5.24) and (5.36) represent the final results of this chapter. On-going work is being performed to find a set for G_i's similar to those found in Chapter 3 for the single-photon exchange and annihilation channels. The intricate interplay between the two equations, and ensuring the necessary complicated cancellations is certainly

more non-trivial than in the other sectors. With a definition of $G_{\gamma\gamma}$ and $G_{4\ell}$, it would be possible to derive effective helicity elements, and TMSWIFT would allow for implementing these elements easily. The numerical effort needed for these diagrams remains unclear for two reasons: first, unlike the other Fock-states, the $|\gamma\gamma\rangle$ has an infrared divergence that must be treated, and a suggested implementation like a photon mass would require a increased number of calculations to ensure that the limit of $m_\gamma = 0$ is correctly reached. Additionally, these interactions also require an integral over the internal momenta, which may be possible only numerically. This would increase the needed time to perform a calculation.

Chapter 6

CONCLUDING AND LOOKING FORWARD

In this thesis, non-perturbative light-front bound-state calculations have been developed to tackle the problem of relativistic true muonium. To do this, the positronium model developed by Trittmann[1, 94, 95] has been extended to include multiple flavors that mix through the annihilation channel. With this multiple flavor model, it has been possible to explore the effect of both lighter (e) and heavier (τ) particles on the spectrum of the non-pertubative true muonium. In addition to the spectrum, this thesis has produced decay constants for a non-perturbative QED system for the first time. An additional limitation that has been overcome in this work is numerical. Through the development of the parallel code TMSWIFT, it is possible to calculate the bound states of much larger Fock spaces than previously possible.

For this thesis, a fully regularized effective integral equation has been derived for the first time. The better large-$\boldsymbol{k}_\perp$ behavior of this model has made it possible for the first time to extrapolate to the $N, \Lambda \to \infty$ limit. From these results, it has been seen in Chapter 4 that renormalization will play a larger role than previously anticipated in the bound-state problem, given that the scale $\Lambda \approx m\alpha$ seems to reproduce the perturbative instant-form calculations best.

The inclusion of lighter flavors has presented a particularly difficult challenge, due to the need to numerical sample a large range of continuum states in order to accurately determine their effect on the true muonium state. At present, initial results produced here have indicated that it is possible to acheive reasonabe agreement with the instant-form prediction, albeit with large numerical effort. On the other hand, inclusion of heavier flavors seems much simpler, but the agreement with theory is

poorer.

Beyond merely calculating for a single value of α, in this thesis a systematic investigation of varying α has been undertaken. The regularized spectrum and decay constants, while not agreeing with the instant-form values, does exhibit the correct α-dependence. Further, following the work of Krautgärtner, the large-$\boldsymbol{k}_\perp$ scaling as a function of α has been studied to understand both the effect of regularization and to pin-point the origin of the $\log \Lambda$ divergences that appear in the energy levels.

In order to proceed further, part of this thesis has been devoted to the derivation of the effective interaction by including the $|\gamma\gamma\rangle$. To properly include this interaction and preserve gauge invariance, it has been seen that the $|\ell^+\ell^-\ell^+\ell^-\rangle$ should partially be included. The necessary integrals for each sector have been derived, but the derivation of the correct non-perturbative propagators to fully cancel the instantenous diagrams remains for future work. With these, it should be possible to study both QED and QCD at a new level of precision.

As emphasized by the regularized results obtained in this thesis, renormalization is a critical issue that remains to be solved. With TMSWIFT, the computational limitations have been dramatically decreased. This presents the opportunity to investigate a number of different renormalization techniques that have been discussed in the literature[221, 222, 201, 202, 203, 205, 208].

Despite the issue of renormalization, it has been shown here that consistent results for relativistic wave functions are have been produced. These can be directly applied now to the question of true muonium production cross sections at the upcoming fixed-target experiments. Further, the methods and code developed in this thesis can be pushed further, and applied to QCD, or perhaps more excitingly, to the spectrum for beyond standard model theories.

In conclusion, this thesis has presented an important step forward in the development of non-perturbative quantum field theory methods. The work undertaken here has improved the understanding of light-front techniques as well as developed software tools necessary to make predictions of the true muonium bound state, and other QED states.

REFERENCES

[1] Uwe Trittmann and Hans-Christian Pauli. Quantum electrodynamics at strong couplings. 1997.

[2] Stanley J. Brodsky, Hans-Christian Pauli, and Stephen S. Pinsky. Quantum chromodynamics and other field theories on the light cone. *Phys. Rept.*, 301:299–486, 1998.

[3] Henry Lamm. Electroweak corrections to the true muonium hyperfine splitting. *Phys. Rev. D*, 91:073008, Apr 2015.

[4] G. W. Bennett et al. Measurement of the negative muon anomalous magnetic moment to 0.7 ppm. *Phys. Rev. Lett.*, 92:161802, 2004.

[5] G.W. Bennett et al. Final Report of the Muon E821 Anomalous Magnetic Moment Measurement at BNL. *Phys. Rev.*, D73:072003, 2006.

[6] Michel Davier, Andreas Hoecker, Bogdan Malaescu, and Zhiqing Zhang. Reevaluation of the Hadronic Contributions to the Muon $g-2$ and to $\alpha(M_Z)$. *Eur. Phys. J.*, C71:1515, 2011. [Erratum: Eur. Phys. J.C72,1874(2012)].

[7] Fred Jegerlehner. Leading-order hadronic contribution to the electron and muon $g-2$. 2015.

[8] Bipasha Chakraborty, C. T. H. Davies, P. G. de Oliviera, J. Koponen, and G. P. Lepage. The hadronic vacuum polarization contribution to a_μ from full lattice QCD. 2016.

[9] Thomas Blum, Achim Denig, Ivan Logashenko, Eduardo de Rafael, B. Lee Roberts, Thomas Teubner, and Graziano Venanzoni. The Muon $(g-2)$ Theory Value: Present and Future. 2013.

[10] Tatsumi Aoyama, M. Hayakawa, Toichiro Kinoshita, and Makiko Nio. Tenth-Order Electron Anomalous Magnetic Moment — Contribution of Diagrams without Closed Lepton Loops. *Phys. Rev.*, D91(3):033006, 2015.

[11] David W. Hertzog. Next Generation Muon $g-2$ Experiments. In *Workshop on Flavour changing and conserving processes 2015 (FCCP2015) Anacapri, Capri Island, Italy, September 10-12, 2015*, 2015.

[12] Stanley J. Brodsky and S. D. Drell. The Anomalous Magnetic Moment and Limits on Fermion Substructure. *Phys. Rev.*, D22:2236, 1980.

[13] Takeo Moroi. The Muon anomalous magnetic dipole moment in the minimal supersymmetric standard model. *Phys. Rev.*, D53:6565–6575, 1996. [Erratum: Phys. Rev.D56,4424(1997)].

[14] Carl E. Carlson and Michael Freid. Extending theories on muon-specific interactions. *Phys. Rev.*, D92(9):095024, 2015.

70

[15] Peter J. Mohr, David B. Newell, and Barry N. Taylor. CODATA Recommended Values of the Fundamental Physical Constants: 2014. 2015.

[16] Aldo Antognini, Francois Nez, Karsten Schuhmann, Fernando D. Amaro, Francois Biraben, et al. Proton Structure from the Measurement of $2S - 2P$ Transition Frequencies of Muonic Hydrogen. *Science*, 339:417–420, 2013.

[17] Randolf Pohl, Aldo Antognini, Francois Nez, Fernando D. Amaro, Francois Biraben, et al. The size of the proton. *Nature*, 466:213–216, 2010.

[18] David Tucker-Smith and Itay Yavin. Muonic hydrogen and MeV forces. *Phys. Rev.*, D83:101702, 2011.

[19] Joerg Jaeckel and Sabyasachi Roy. Spectroscopy as a test of Coulomb's law: A Probe of the hidden sector. *Phys. Rev.*, D82:125020, 2010.

[20] Vernon Barger, Cheng-Wei Chiang, Wai-Yee Keung, and Danny Marfatia. Proton size anomaly. *Phys.Rev.Lett.*, 106:153001, 2011.

[21] S.G. Karshenboim. Precision physics of simple atoms and constraints on a light boson with ultraweak coupling. *Phys. Rev. Lett.*, 104:220406, 2010.

[22] S.G. Karshenboim. HFS interval of the $2s$ state of hydrogen-like atoms and a constraint on a pseudovector boson with mass below $1\,\mathrm{keV}/c^2$. *Phys. Rev.*, A83:062119, 2011.

[23] U. D. Jentschura. Lamb Shift in Muonic Hydrogen. II. Analysis of the Discrepancy of Theory and Experiment. *Annals Phys.*, 326:516–533, 2011.

[24] Vernon Barger, Cheng-Wei Chiang, Wai-Yee Keung, and Danny Marfatia. Constraint on parity-violating muonic forces. *Phys.Rev.Lett.*, 108:081802, 2012.

[25] Brian Batell, David McKeen, and Maxim Pospelov. New Parity-Violating Muonic Forces and the Proton Charge Radius. *Phys. Rev. Lett.*, 107:011803, 2011.

[26] Carl E. Carlson and Benjamin C. Rislow. New Physics and the Proton Radius Problem. *Phys.Rev.*, D86:035013, 2012.

[27] Savely G. Karshenboim, David McKeen, and Maxim Pospelov. Constraints on muon-specific dark forces. *Phys. Rev.*, D90(7):073004, 2014.

[28] Li-Bang Wang and Wei-Tou Ni. Proton radius puzzle and large extra dimensions. *Mod.Phys.Lett.*, A28:1350094, 2013.

[29] Roberto Onofrio. Proton radius puzzle and quantum gravity at the Fermi scale. *Europhys.Lett.*, 104:20002, 2013.

[30] U. D. Jentschura. Light sea Fermions in electron-proton and muon-proton interactions. *Phys. Rev.*, A88(6):062514, 2013.

[31] André H. Gomes, Alan Kostelecký, and Arnaldo J. Vargas. Laboratory tests of Lorentz and CPT symmetry with muons. *Phys. Rev.*, D90(7):076009, 2014.

[32] Philippe Brax and Clare Burrage. Explaining the Proton Radius Puzzle with Disformal Scalars. *Phys.Rev.*, D91(4):043515, 2015.

[33] Henry Lamm. Can Galileons solve the muon problem? *Phys. Rev.*, D92(5):055007, 2015.

[34] A. Antognini et al. Experiments towards resolving the proton charge radius puzzle. 2015.

[35] Roel Aaij et al. Test of lepton universality using $B^+ \rightarrow K^+ \ell^+ \ell^-$ decays. *Phys. Rev. Lett.*, 113(15):151601, 2014.

[36] CMS Collaboration. Search for Lepton Flavour Violating Decays of the Higgs Boson. *CMS-PAS-HIG-14-005*, 2014.

[37] V.W. Hughes and B. Maglic. *Bull. Am. Phys. Soc.*, 16:65, 1971.

[38] Henry Lamm. True muonium: the atom that has it all. 2015.

[39] A. Badertscher, P. Crivelli, W. Fetscher, U. Gendotti, S. Gninenko, V. Postoev, A. Rubbia, V. Samoylenko, and D. Sillou. An Improved Limit on Invisible Decays of Positronium. *Phys. Rev.*, D75:032004, 2007.

[40] L.L. Nemenov. Atomic decays of elementary particles. *Yad. Fiz.*, 15:1047–1050, 1972.

[41] J.W. Moffat. Does a Heavy Positronium Atom Exist? *Phys. Rev. Lett.*, 35:1605, 1975.

[42] Egil Holvik and Haakon A. Olsen. Creation of Relativistic Fermionium in Collisions of Electrons with Atoms. *Phys. Rev.*, D35:2124, 1987.

[43] G.A. Kozlov. On the problem of production of relativistic lepton bound states in the decays of light mesons. *Sov. J. Nucl. Phys.*, 48:167–171, 1988.

[44] I.F. Ginzburg, U.D. Jentschura, Savely G. Karshenboim, F. Krauss, V.G. Serbo, et al. Production of bound $\mu^+\mu^-$ systems in relativistic heavy ion collisions. *Phys. Rev.*, C58:3565–3573, 1998.

[45] N. Arteaga-Romero, C. Carimalo, and V.G. Serbo. Production of bound triplet $\mu^+\mu^-$ system in collisions of electrons with atoms. *Phys. Rev.*, A62:032501, 2000.

[46] Stanley J. Brodsky and Richard F. Lebed. Production of the Smallest QED Atom: True Muonium ($\mu^+\mu^-$). *Phys. Rev. Lett.*, 102:213401, 2009.

[47] Yibiao Chen and Pengfei Zhuang. Dimuonium ($\mu^+\mu^-$) Production in a Quark-Gluon Plasma. 2012.

[48] Andrzej Banburski and Philip Schuster. The Production and Discovery of True Muonium in Fixed-Target Experiments. *Phys. Rev.*, D86:093007, 2012.

[49] S.C. Ellis and J. Bland-Hawthorn. On the possibility of observable signatures of leptonic onium atoms from astrophysical sources. 2015.

[50] Andrea Celentano. The Heavy Photon Search experiment at Jefferson Laboratory. *J. Phys. Conf. Ser.*, 556(1):012064, 2014.

[51] Angela Benelli. DIRAC experiment at CERN. *EPJ Web Conf.*, 37:01011, 2012.

[52] P.V. Chliapnikov. Numbers of $\mu^{\pm}\pi^{\mp}$, $\mu^{+}\mu^{-}$ and $K^{+}K^{-}$ atoms and Coulomb pairs in the DIRAC experiment. *DIRAC-NOTE-2014-05*, 2014.

[53] L. L. Nemenov and V. D. Ovsyannikov. DC field control of decay processes in a (pi+ pi-) atom: A possibility to measure the energy splitting between 2s- and 2p-states. *Phys. Lett.*, B514:247–252, 2001.

[54] John L. Richardson. The Heavy Quark Potential and the Υ, J/Ψ Systems. *Phys. Lett.*, B82:272, 1979.

[55] W. Buchmuller and S. H. H. Tye. Quarkonia and Quantum Chromodynamics. *Phys. Rev.*, D24:132, 1981.

[56] S. Godfrey and Nathan Isgur. Mesons in a Relativized Quark Model with Chromodynamics. *Phys. Rev.*, D32:189–231, 1985.

[57] Gunnar S. Bali. QCD forces and heavy quark bound states. *Phys. Rept.*, 343:1–136, 2001.

[58] Michael Creutz. Confinement and the Critical Dimensionality of Space-Time. *Phys. Rev. Lett.*, 43:553–556, 1979. [Erratum: Phys. Rev. Lett.43,890(1979)].

[59] John B. Kogut and Junko Shigemitsu. Crossover From Weak to Strong Coupling in SU(N) Lattice Gauge Theories. *Phys. Rev. Lett.*, 45:410, 1980. [Erratum: Phys. Rev. Lett.45,1217(1980)].

[60] Kenneth G. Wilson. Confinement of Quarks. *Phys. Rev.*, D10:2445–2459, 1974.

[61] Leonard Susskind. Lattice Fermions. *Phys. Rev.*, D16:3031–3039, 1977.

[62] J. Shigemitsu. Spectrum Calculations in Lattice Gauge Theory Using Wilson's Fermion Method. *Phys. Rev.*, D18:1709, 1978.

[63] H. Hamber and G. Parisi. Numerical Estimates of Hadronic Masses in a Pure SU(3) Gauge Theory. *Phys. Rev. Lett.*, 47:1792, 1981.

[64] Claude W. Bernard, Tom Blum, Carleton E. Detar, Steven A. Gottlieb, Urs M. Heller, James E. Hetrick, Craig McNeile, K. Rummukainen, R. Sugar, and D. Toussaint. Continuum limit of lattice QCD with staggered quarks in the quenched approximation: A Critical role for the chiral extrapolation. *Phys. Rev. Lett.*, 81:3087–3090, 1998.

[65] S. Aoki et al. Quenched light hadron spectrum. *Phys. Rev. Lett.*, 84:238–241, 2000.

[66] S. Durr et al. Ab-Initio Determination of Light Hadron Masses. *Science*, 322:1224–1227, 2008.

[67] Sz. Borsanyi et al. Ab initio calculation of the neutron-proton mass difference. *Science*, 347:1452–1455, 2015.

[68] F. J. Dyson. The S matrix in quantum electrodynamics. *Phys. Rev.*, 75:1736–1755, 1949.

[69] Julian S. Schwinger. On the Green's functions of quantized fields. 1. *Proc. Nat. Acad. Sci.*, 37:452–455, 1951.

[70] Julian S. Schwinger. On the Green's functions of quantized fields. 2. *Proc. Nat. Acad. Sci.*, 37:455–459, 1951.

[71] Craig D. Roberts and Anthony G. Williams. Dyson-Schwinger equations and their application to hadronic physics. *Prog. Part. Nucl. Phys.*, 33:477–575, 1994.

[72] Reinhard Alkofer and Lorenz von Smekal. The Infrared behavior of QCD Green's functions: Confinement dynamical symmetry breaking, and hadrons as relativistic bound states. *Phys. Rept.*, 353:281, 2001.

[73] E. E. Salpeter and H. A. Bethe. A Relativistic equation for bound state problems. *Phys. Rev.*, 84:1232–1242, 1951.

[74] E. E. Salpeter. Wave Functions in Momentum Space. *Phys. Rev.*, 84:1226–1231, 1951.

[75] E. E. Salpeter. Mass corrections to the fine structure of hydrogen - like atoms. *Phys. Rev.*, 87:328–342, 1952.

[76] G. C. Wick. Properties of Bethe-Salpeter Wave Functions. *Phys. Rev.*, 96:1124–1134, 1954.

[77] W. E. Caswell and G. P. Lepage. Effective Lagrangians for Bound State Problems in QED, QCD, and Other Field Theories. *Phys. Lett.*, B167:437, 1986.

[78] Thomas Hilger, Carina Popovici, Maria Gomez-Rocha, and Andreas Krassnigg. Spectra of heavy quarkonia in a Bethe-Salpeter-equation approach. *Phys. Rev.*, D91(3):034013, 2015.

[79] A. Pineda and J. Soto. Effective field theory for ultrasoft momenta in NRQCD and NRQED. *Nucl. Phys. Proc. Suppl.*, 64:428–432, 1998.

[80] Nora Brambilla, Antonio Pineda, Joan Soto, and Antonio Vairo. Potential NRQCD: An Effective theory for heavy quarkonium. *Nucl. Phys.*, B566:275, 2000.

[81] Shoichi Sasaki, Tom Blum, and Shigemi Ohta. Lattice study of the nucleon excited states with domain wall fermions. *Physical Review D*, 65(7):074503, 2002.

[82] Jozef J Dudek, Robert G Edwards, Nilmani Mathur, and David G Richards. Charmonium excited state spectrum in lattice qcd. *Physical Review D*, 77(3):034501, 2008.

[83] Zoltan Fodor and Christian Hoelbling. Light hadron masses from lattice qcd. *Reviews of Modern Physics*, 84(2):449, 2012.

[84] R. A. Briceno et al. Issues and Opportunities in Exotic Hadrons. 2015.

[85] Stephan Dürr, Zoltán Fodor, Christian Hoelbling, Stefan Krieg, Thorsten Kurth, Laurent Lellouch, Thomas Lippert, Rehan Malak, Thibaut Métivet, Antonin Portelli, et al. Lattice qcd at the physical point meets s u (2) chiral perturbation theory. *Physical Review D*, 90(11):114504, 2014.

[86] Georg P Engel, Leonardo Giusti, Stefano Lottini, and Rainer Sommer. Chiral symmetry breaking in qcd with two light flavors. *Physical review letters*, 114(11):112001, 2015.

[87] Gunnar S. Bali, Vladimir M. Braun, Meinulf Göckeler, Michael Gruber, Fabian Hutzler, Andreas Schäfer, Jakob Simeth, Wolfgang Söldner, Andre Sternbeck, and Philipp Wein. Light-cone distribution amplitudes of the baryon octet. 2015.

[88] Adnan Bashir and Alfredo Raya. Gauge symmetry and its implications for the Schwinger-Dyson equations. 2004.

[89] Dennis D. Dietrich, Paul Hoyer, and Matti Jarvinen. Boosting equal time bound states. *Phys. Rev.*, D85:105016, 2012.

[90] Noboru Nakanishi. A General survey of the theory of the Bethe-Salpeter equation. *Prog. Theor. Phys. Suppl.*, 43:1–81, 1969.

[91] Jeff Greensite. An introduction to the confinement problem. *Lect. Notes Phys.*, 821:1–211, 2011.

[92] Paul A. M. Dirac. Forms of Relativistic Dynamics. *Rev. Mod. Phys.*, 21:392–399, 1949.

[93] Hans Christian Pauli and Stanley J. Brodsky. Discretized Light Cone Quantization: Solution to a Field Theory in One Space One Time Dimensions. *Phys. Rev.*, D32:2001, 1985.

[94] Uwe Trittmann. On the role of the annihilation channel in front form positronium. 1997.

[95] U. Trittmann and H. C. Pauli. On rotations in front-form dynamics. *Nucl. Phys. Proc. Suppl.*, 90:161–169, 2000. [,161(2000)].

[96] H. Leutwyler and J. Stern. Relativistic Dynamics on a Null Plane. *Annals Phys.*, 112:94, 1978.

[97] Julian S. Schwinger. Quantum electrodynamics. 2. Vacuum polarization and selfenergy. *Phys. Rev.*, 75:651, 1948.

[98] Julian S. Schwinger. Quantum electrodynamics. I A covariant formulation. *Phys. Rev.*, 74:1439, 1948.

[99] R. P. Feynman. Space - time approach to quantum electrodynamics. *Phys. Rev.*, 76:769–789, 1949.

[100] R. P. Feynman. The Theory of positrons. *Phys. Rev.*, 76:749–759, 1949.

[101] R. P. Feynman. Relativistic cutoff for quantum electrodynamics. *Phys. Rev.*, 74:1430–1438, 1948.

[102] R. P. Feynman. Space-time approach to nonrelativistic quantum mechanics. *Rev. Mod. Phys.*, 20:367–387, 1948.

[103] Sin-Itiro Tomonaga and J. R. Oppenheimer. On Infinite Field Reactions in Quantum Field Theory. *Phys. Rev.*, 74:224–225, 1948.

[104] S. Tomonaga. On a relativistically invariant formulation of the quantum theory of wave fields. *Prog. Theor. Phys.*, 1:27–42, 1946.

[105] Steven Weinberg. Dynamics at infinite momentum. *Phys. Rev.*, 150:1313–1318, 1966.

[106] John B. Kogut and Davison E. Soper. Quantum Electrodynamics in the Infinite Momentum Frame. *Phys. Rev.*, D1:2901–2913, 1970.

[107] N. E. Ligterink and B. L. G. Bakker. Equivalence of light front and covariant field theory. *Phys. Rev.*, D52:5954–5979, 1995.

[108] Shau-Jin Chang, Robert G. Root, and Tung-Mow Yan. Quantum field theories in the infinite momentum frame. 1. Quantization of scalar and Dirac fields. *Phys. Rev.*, D7:1133–1148, 1973.

[109] Tung-Mow Yan. Quantum field theories in the infinite momentum frame 3. Quantization of coupled spin one fields. *Phys. Rev.*, D7:1760–1779, 1973.

[110] Shau-Jin Chang and Tung-Mow Yan. Quantum field theories in the infinite momentum frame. 2. Scattering matrices of scalar and Dirac fields. *Phys. Rev.*, D7:1147–1161, 1973.

[111] Bernard L. G. Bakker, Martin A. DeWitt, Chueng-Ryong Ji, and Yuriy Mishchenko. Restoring the equivalence between the light-front and manifestly covariant formalisms. *Phys. Rev.*, D72:076005, 2005.

[112] Anuradha Misra and Swati Warawdekar. Equivalence of covariant and light front QED at one loop level. *Phys. Rev.*, D71:125011, 2005.

[113] Swati M. Patel and Anuradha Misra. Equivalence of Covariant and Light Front QED: Generating Instantaneous Diagrams. *Phys. Rev.*, D82:125024, 2010.

[114] G. Peter Lepage and Stanley J. Brodsky. Exclusive Processes in Perturbative Quantum Chromodynamics. *Phys. Rev.*, D22:2157, 1980.

[115] Billy D. Jones and Robert J. Perry. The Lamb shift in a light front Hamiltonian approach. *Phys. Rev.*, D55:7715–7730, 1997.

[116] Billy D. Jones, Robert J. Perry, and Stanislaw D. Glazek. Analytic treatment of positronium spin splittings in light front QED. *Phys. Rev.*, D55:6561–6583, 1997.

[117] Billy D. Jones. Singlet - triplet splitting of positronium in light front QED. In *High-energy physics and cosmology. Proceedings, 25th Coral Gables International Conference on Orbis Scientiae, Miami Beach, USA, January 23-26, 1997*, pages 201–207, 1997.

[118] Billy Darwin Jones. *Light front Hamiltonian approach to the bound state problem in quantum electrodynamics*. PhD thesis, Ohio State U., 1997.

[119] Stanislaw D. Glazek, Avaroth Harindranath, Stephen Pinsky, Junko Shigemitsu, and Kenneth Wilson. On the relativistic bound state problem in the light front Yukawa model. *Phys. Rev.*, D47:1599–1619, 1993.

[120] Bernard L. G. Bakker, Jorn K. Boomsma, and Chueng-Ryong Ji. The Box diagram in Yukawa theory. *Phys. Rev.*, D75:065010, 2007.

[121] B. L. G. Bakker, Miranda van Iersel, and F. Pijlman. Comparison of relativistic bound state calculations in front form and instant form dynamics. *Few Body Syst.*, 33:27–47, 2003.

[122] M. Mangin-Brinet, J. Carbonell, and V. A. Karmanov. Relativistic bound states in Yukawa model. *Phys. Rev.*, D64:125005, 2001.

[123] M. Mangin-Brinet, J. Carbonell, and V. A. Karmanov. Two fermion relativistic bound states in light front dynamics. *Phys. Rev.*, C68:055203, 2003.

[124] Prem P. Srivastava and Stanley J. Brodsky. Light-front formulation of the standard model. *Phys. Rev. D*, 66:045019, Aug 2002.

[125] Mikolaj Sawicki. Eigensolutions of the Light Cone Equation for Scalar Field Model. *Phys. Rev.*, D33:1103, 1986.

[126] Mikolaj Sawicki. Solution of the Light Cone Equation for the Relativistic Bound State. *Phys. Rev.*, D32:2666, 1985.

[127] A. Harindranath and J. P. Vary. Solving two-dimensional ϕ^4 theory by discretized light front quantization. *Phys. Rev.*, D36:1141–1147, 1987.

[128] A. Harindranath and J. P. Vary. Stability of the Vacuum in Scalar Field Models in 1 + 1 Dimensions. *Phys. Rev.*, D37:1076–1078, 1988.

[129] A. Harindranath and J. P. Vary. Light Front Hamiltonian Approach to Relativistic Two and Three-body Bound State Problems in (1+1)-dimensions. *Phys. Rev.*, D37:1064–1069, 1988.

[130] Kent Hornbostel, Stanley J. Brodsky, and Hans Christian Pauli. Light Cone Quantized QCD in (1+1)-Dimensions. *Phys. Rev.*, D41:3814, 1990.

[131] Thomas Eller, Hans Christian Pauli, and Stanley J. Brodsky. Discretized Light Cone Quantization: The Massless and the Massive Schwinger Model. *Phys. Rev.*, D35:1493, 1987.

[132] T. Heinzl, S. Krusche, and E. Werner. The Fermionic Schwinger model in light cone quantization. *Phys. Lett.*, B275:410–418, 1992.

[133] Gary McCartor. Light cone gauge Schwinger model. *Z. Phys.*, C52:611–626, 1991.

[134] Gary McCartor. Schwinger model in the light cone representation. *Z. Phys.*, C64:349–354, 1994.

[135] Gary McCartor. Some lessons from the Schwinger model. *Int. J. Mod. Phys.*, A12:1091–1100, 1997.

[136] Yuji Nakawaki and Gary McCartor. Light - cone quantization of the Schwinger model. *Prog. Theor. Phys.*, 103:161–181, 2000.

[137] S. Strauss and M. Beyer. Light front QED(1+1) at finite temperature. *Phys. Rev. Lett.*, 101:100402, 2008.

[138] S. Strauss and M. Beyer. Massive light-front Schwinger model at finite temperature. *Prog. Part. Nucl. Phys.*, 62:535–537, 2009.

[139] Stefan Strauss and Michael Beyer. Low-dimensional light front gauge theory at finite temperature. *Nucl. Phys. Proc. Suppl.*, 199:160–165, 2010.

[140] John R. Hiller. Calculation of R(s) e^+e^- in (1+1) QED: Application of Lanczos tridiagonalization and recursion. *Phys. Rev.*, D43:2418–2424, 1991.

[141] Brett van de Sande. Convergence of discretized light cone quantization in the small mass limit. *Phys. Rev.*, D54:6347–6350, 1996.

[142] Uwe Trittmann. On the bosonic spectrum of QCD(1+1) with SU(N) currents. *Nucl. Phys.*, B587:311–327, 2000.

[143] Uwe Trittmann. On the spectrum of QCD(1+1) with SU(N(c)) currents. *Phys. Rev.*, D66:025001, 2002.

[144] Uwe Trittmann. Towards finding the single-particle content of two-dimensional adjoint QCD. *Phys. Rev.*, D92(8):085021, 2015.

[145] S. Pinsky and U. Trittmann. Antiperiodic boundary conditions in supersymmetric DLCQ. *Phys. Rev.*, D62:087701, 2000.

[146] John R. Hiller, Stephen Pinsky, and Uwe Trittmann. Wave functions and properties of massive states in three-dimensional supersymmetric Yang-Mills theory. *Phys. Rev.*, D64:105027, 2001.

[147] J. R. Hiller, S. S. Pinsky, and U. Trittmann. Simulation of dimensionally reduced SYM Chern-Simons theory. *Phys. Rev.*, D65:085046, 2002.

[148] J. R. Hiller, S. S. Pinsky, and U. Trittmann. Properties of the bound states of super Yang-Mills-Chern-Simons theory. *Phys. Rev.*, D66:125015, 2002.

[149] J. R. Hiller, S. S. Pinsky, and U. Trittmann. Anomalously light states in superyang-Mills Chern-Simons theory. *Phys. Lett.*, B541:396–405, 2002.

[150] J. R. Hiller, S. S. Pinsky, and U. Trittmann. Anomalously light mesons in a (1+1)-dimensional supersymmetric theory with fundamental matter. *Nucl. Phys.*, B661:99–112, 2003.

[151] J. R. Hiller, S. S. Pinsky, and U. Trittmann. Spectrum of N=1 massive superYang-Mills theory with fundamental matter in (1+1)-dimensions. *Phys. Rev.*, D67:115005, 2003.

[152] John R. Hiller, Motomichi Harada, Stephen S. Pinsky, Nathan Salwen, and Uwe Trittmann. Two-dimensional super Yang-Mills theory investigated with improved resolution. *Phys. Rev.*, D71:085008, 2005.

[153] John R. Hiller, Stephen S. Pinsky, Nathan Salwen, and Uwe Trittmann. Direct evidence for the Maldacena conjecture for N=(8,8) super Yang-Mills theory in 1+1 dimensions. *Phys. Lett.*, B624:105–114, 2005.

[154] John R. Hiller, Stephen Pinsky, Yiannis Proestos, Nathan Salwen, and Uwe Trittmann. Spectrum and thermodynamic properties of two-dimensional N=(1,1) super Yang-Mills theory with fundamental matter and a Chern-Simons term. *Phys. Rev.*, D76:045008, 2007.

[155] Uwe Trittmann and Stephen S. Pinsky. Effects of a fundamental mass term in two-dimensional super Yang-Mills theory. *Phys. Rev.*, D80:065005, 2009.

[156] Stephen S. Pinsky and Brett van de Sande. Spontaneous symmetry breaking of (1+1)-dimensional ϕ^4 theory in light front field theory. 2. *Phys. Rev.*, D49:2001–2013, 1994.

[157] Stephen S. Pinsky, Brett van de Sande, and John R. Hiller. Spontaneous symmetry breaking of (1+1)-dimensional ϕ^4 theory in light front field theory. 3. *Phys. Rev.*, D51:726–733, 1995.

[158] Carl M. Bender, Stephen Pinsky, and Brett Van de Sande. Spontaneous symmetry breaking of ϕ^4 in (1+1)-dimensions in light front field theory. *Phys. Rev.*, D48:816–821, 1993.

[159] J. R. Hiller, O. Lunin, S. Pinsky, and U. Trittmann. Towards a SDLCQ test of the Maldacena conjecture. *Phys. Lett.*, B482:409–416, 2000.

[160] Andrew C. Tang, Stanley J. Brodsky, and Hans Christian Pauli. Discretized light cone quantization: Formalism for quantum electrodynamics. *Phys. Rev.*, D44:1842–1865, 1991.

[161] M. Kaluza and H. C. Pauli. Discretized light cone quantization: $e^+e^-(\gamma)$ model for positronium. *Phys. Rev.*, D45:2968–2981, 1992.

[162] F. Wolz. Numerische Losung des Coulomb-Problems in der Impulsdarstellung. Master's thesis, Heidelberg, 1990.

[163] M. Krautgartner, H. C. Pauli, and F. Wolz. Positronium and heavy quarkonia as testing case for discretized light cone quantization. 1. *Phys. Rev.*, D45:3755–3774, 1992.

[164] A. C. Kalloniatis and H. C. Pauli. Bosonic zero modes and gauge theory in discrete light cone quantization. *Z. Phys.*, C60:255–264, 1993.

[165] M. Krautgartner. *Anwendung der DLCQ auf die QED*. PhD thesis, Heidelberg, 1992.

[166] F. Wolz. *Über das Spektrum der Normalmoden in der QCD und die Theorie der effektiven Wechselwirkung nach der Tamm-Dancoff Methode"*. PhD thesis, Heidelberg, 1995.

[167] J. P. Vary, H. Honkanen, Jun Li, P. Maris, S. J. Brodsky, A. Harindranath, G. F. de Teramond, P. Sternberg, E. G. Ng, and C. Yang. Hamiltonian light-front field theory in a basis function approach. *Phys. Rev.*, C81:035205, 2010.

[168] Xingbo Zhao, Heli Honkanen, Pieter Maris, James P. Vary, and Stanley J. Brodsky. Electron Anomalous Magnetic Moment in Basis Light-Front Quantization Approach. *Few Body Syst.*, 52:339–344, 2012.

[169] Pieter Maris, Paul Wiecki, Yang Li, Xingbo Zhao, and James P. Vary. Bound state calculations in QED and QCD using basis light-front quantization. *Acta Phys. Polon. Supp.*, 6:321–326, 2013.

[170] Xingbo Zhao, Anton Ilderton, Pieter Maris, and James P. Vary. Scattering in Time-Dependent Basis Light-Front Quantization. *Phys. Rev.*, D88:065014, 2013.

[171] Xingbo Zhao, Anton Ilderton, Pieter Maris, and James P. Vary. Non-perturbative quantum time evolution on the light-front. *Phys. Lett.*, B726:856–860, 2013.

[172] D. Chakrabarti, X. Zhao, H. Honkanen, R. Manohar, P. Maris, and J. P. Vary. Generalized parton distributions in a light-front nonperturbative approach. *Phys. Rev.*, D89(11):116004, 2014.

[173] Xingbo Zhao, Heli Honkanen, Pieter Maris, James P. Vary, and Stanley J. Brodsky. Electron $g - 2$ in Light-Front Quantization. *Phys. Lett.*, B737:65–69, 2014.

[174] Yang Li, Pieter Maris, Xingbo Zhao, and James P. Vary. Heavy Quarkonium in a Holographic Basis. 2015.

[175] Hans-Christian Pauli, Alex C. Kalloniatis, and Stephen S. Pinsky. Towards solving QCD: The transverse zero modes in light cone quantization. *Phys. Rev.*, D52:1176–1189, 1995.

[176] S. Dalley and B. van de Sande. Transverse lattice QCD in (2+1)-dimensions. *Nucl. Phys. Proc. Suppl.*, 53:827–830, 1997.

[177] Brett van de Sande and Simon Dalley. The Transverse lattice in (2+1)-dimensions. In *Neutrino mass, dark matter, gravitational waves, monopole condensation, and light cone quantization. Proceedings, International Conference, Orbis Scientiae 1996, Miami Beach, USA, January 25-28, 1996*, 1996.

[178] Simon Dalley. Introduction to transverse lattice gauge theory. *AIP Conf. Proc.*, 494:45–64, 1999.

[179] Brett van de Sande and Matthias Burkardt. Tube model for light front QCD. *Phys. Rev.*, D53:4628–4637, 1996.

[180] Martina M. Brisudova, Robert J. Perry, and Kenneth G. Wilson. Quarkonia in Hamiltonian light front QCD. *Phys. Rev. Lett.*, 78:1227–1230, 1997.

[181] Dipankar Chakrabarti and A. Harindranath. Mesons in light front QCD(2+1): Investigation of a Bloch effective Hamiltonian. *Phys. Rev.*, D64:105002, 2001.

[182] Guy F. de Teramond and Stanley J. Brodsky. Light-Front Holography: A First Approximation to QCD. *Phys. Rev. Lett.*, 102:081601, 2009.

[183] Guy F. de Teramond and Stanley J. Brodsky. Light-Front Quantization Approach to the Gauge-Gravity Correspondence and Hadron Spectroscopy. *AIP Conf. Proc.*, 1257:59–68, 2010.

[184] Stanley J. Brodsky, Guy F. de Teramond, and Alexandre Deur. Nonperturbative QCD Coupling and its β-function from Light-Front Holography. *Phys. Rev.*, D81:096010, 2010.

[185] Guy F. de Teramond and Stanley J. Brodsky. Gauge/Gravity Duality and Hadron Physics at the Light-Front. *AIP Conf. Proc.*, 1296:128–139, 2010.

[186] Stanley J. Brodsky, Guy F. De Téramond, and Hans Günter Dosch. Threefold Complementary Approach to Holographic QCD. *Phys. Lett.*, B729:3–8, 2014.

[187] Stanley J. Brodsky, Guy F. de Teramond, Hans Gunter Dosch, and Joshua Erlich. Light-Front Holographic QCD and Emerging Confinement. *Phys. Rept.*, 584:1–105, 2015.

[188] Guy F. de Teramond, Hans Gunter Dosch, and Stanley J. Brodsky. Baryon Spectrum from Superconformal Quantum Mechanics and its Light-Front Holographic Embedding. *Phys. Rev.*, D91(4):045040, 2015.

[189] Stanley J. Brodsky, Alexandre Deur, Guy F. de Téramond, and Hans Günter Dosch. Light-Front Holography and Superconformal Quantum Mechanics: A New Approach to Hadron Structure and Color Confinement. *Int. J. Mod. Phys. Conf. Ser.*, 39:1560081, 2015.

[190] Hans Gunter Dosch, Guy F. de Teramond, and Stanley J. Brodsky. Supersymmetry Across the Light and Heavy-Light Hadronic Spectrum. *Phys. Rev.*, D92(7):074010, 2015.

[191] Hans Gunter Dosch, Guy F. de Teramond, and Stanley J. Brodsky. Superconformal Baryon-Meson Symmetry and Light-Front Holographic QCD. *Phys. Rev.*, D91(8):085016, 2015.

[192] Gary McCartor and David G. Robertson. Bosonic zero modes in discretized light cone field theory. *Z. Phys.*, C53:679–686, 1992.

[193] T. Heinzl, S. Krusche, S. Simburger, and E. Werner. Nonperturbative light cone quantum field theory beyond the tree level. *Z. Phys.*, C56:415–420, 1992.

[194] A. C. Kalloniatis and H. C. Pauli. On zero modes and gauge fixing in light cone quantized gauge theories. *Z. Phys.*, C63:161–168, 1994.

[195] Stanley Mandelstam. Light Cone Superspace and the Ultraviolet Finiteness of the N=4 Model. *Nucl. Phys.*, B213:149–168, 1983.

[196] George Leibbrandt. The Light Cone Gauge in Yang-Mills Theory. *Phys. Rev.*, D29:1699, 1984.

[197] George Leibbrandt. Introduction to Noncovariant Gauges. *Rev. Mod. Phys.*, 59:1067, 1987.

[198] A. Bassetto, M. Dalbosco, I. Lazzizzera, and R. Soldati. Yang-Mills Theories in the Light Cone Gauge. *Phys. Rev.*, D31:2012, 1985.

[199] Kenneth G. Wilson, Timothy S. Walhout, Avaroth Harindranath, Wei-Min Zhang, Robert J. Perry, and Stanislaw D. Glazek. Nonperturbative QCD: A Weak coupling treatment on the light front. *Phys. Rev.*, D49:6720–6766, 1994.

[200] D. Mustaki, S. Pinsky, J. Shigemitsu, and K. Wilson. Perturbative renormalization of null plane QED. *Phys. Rev.*, D43:3411–3427, 1991.

[201] Sophia S. Chabysheva and John R. Hiller. A nonperturbative calculation of the electron's magnetic moment with truncation extended to two photons. *Phys. Rev.*, D81:074030, 2010.

[202] Sophia S. Chabysheva and John R. Hiller. Nonperturbative Pauli-Villars regularization of vacuum polarization in light-front QED. *Phys. Rev.*, D82:034004, 2010.

[203] M. Yu. Malyshev, S. A. Paston, E. V. Prokhvatilov, and R. A. Zubov. Renormalized Light Front Hamiltonian in the Pauli-Villars Regularization. *Int. J. Theor. Phys.*, 54(1):169–184, 2015.

[204] Sophia S. Chabysheva and John R. Hiller. BRST-invariant Pauli-Villars regularization of QCD. 2015.

[205] V. A. Karmanov, J. F. Mathiot, and A. V. Smirnov. Systematic renormalization scheme in light-front dynamics with Fock space truncation. *Phys. Rev.*, D77:085028, 2008.

[206] V. A. Karmanov, J. F. Mathiot, and A. V. Smirnov. Non-perturbative approach in truncated Fock space including antifermion. *Nucl. Phys. Proc. Suppl.*, 199:35–43, 2010.

[207] V. A. Karmanov, J. F. Mathiot, and A. V. Smirnov. Nonperturbative calculation of the anomalous magnetic moment in the Yukawa model within truncated Fock space. *Phys. Rev.*, D82:056010, 2010.

[208] V. A. Karmanov, J. F. Mathiot, and A. V. Smirnov. Ab initio nonperturbative calculation of physical observables in light-front dynamics. Application to the Yukawa model. *Phys. Rev.*, D86:085006, 2012.

[209] Yang Li, V. A. Karmanov, P. Maris, and James P. Vary. Non-Perturbative Calculation of the Scalar Yukawa Theory in Four-Body Truncation. *Few Body Syst.*, 56(6-9):495–501, 2015.

[210] Yang Li, V. A. Karmanov, P. Maris, and J. P. Vary. Ab Initio Approach to the Non-Perturbative Scalar Yukawa Model. *Phys. Lett.*, B748:278–283, 2015.

[211] Anuradha Misra. Coherent states in null plane QED. *Phys. Rev.*, D50:4088–4096, 1994.

[212] Anuradha Misra. Light cone quantization and the coherent state basis. *Phys. Rev.*, D53:5874–5885, 1996.

[213] Anuradha Misra. Coherent states in light front QCD. *Phys. Rev.*, D62:125017, 2000.

[214] Jai D. More and Anuradha Misra. Infra-red Divergences in Light-Front QED and Coherent State Basis. *Phys. Rev.*, D86:065037, 2012.

[215] Jai D. More and Anuradha Misra. Fermion Self Energy Correction in Light-Front QED using Coherent State Basis. *Phys. Rev.*, D87:085035, 2013.

[216] Jai D. More and Anuradha Misra. Cancellation of infrared divergences to all orders in light front QED. *Phys. Rev.*, D89(10):105021, 2014.

[217] S. S. Chabysheva and J. R. Hiller. A Light-Front Coupled-Cluster Method for the Nonperturbative Solution of Quantum Field Theories. *Phys. Lett.*, B711:417–422, 2012.

[218] B. Elliott, S. S. Chabysheva, and J. R. Hiller. Application of the light-front coupled-cluster method to ϕ^4 theory in two dimensions. *Phys. Rev.*, D90(5):056003, 2014.

[219] Brett van de Sande and Stephen S. Pinsky. Renormalization of Tamm-Dancoff integral equations. *Phys. Rev.*, D46:5479–5486, 1992.

[220] Stanislaw D. Glazek and Kenneth G. Wilson. Renormalization of Hamiltonians. *Phys. Rev.*, D48:5863–5872, 1993.

[221] Elena L. Gubankova, Hans-Christian Pauli, and Franz J. Wegner. Light cone Hamiltonian flow for positronium. 1998.

[222] Elena L. Gubankova and Gabor Papp. Light cone Hamiltonian flow for positronium: The Numerical solutions. 1999.

[223] Elena Gubankova, Chueng-Ryong Ji, and Stephen R. Cotanch. Flow equations for quark gluon interactions in light front QCD. *Phys. Rev.*, D62:125012, 2000.

[224] Elena Gubankova, Chueng-Ryong Ji, and Stephen R. Cotanch. Flow equations for gluodynamics in the Coulomb gauge. *Phys. Rev.*, D62:074001, 2000.

[225] Elena Gubankova. Solving QCD Hamiltonian for bound states. In *2001 Joint INF - JLab Workshop on Correlations in Nucleons and Nuclei Seattle, Washington, March 12-16, 2001*, 2002.

[226] H. C. Pauli. Solving gauge field theory by discretized light cone quantization. In *Perspectives of strong coupling gauge theories. Proceedings, International Workshop, SCGT'96, Nagoya, Japan, November 13-16, 1996*, 1997.

[227] H. C. Pauli. On confinement in a light cone Hamiltonian for QCD. *Eur. Phys. J.*, C7:289–303, 1999.

[228] Henry Lamm and Richard F. Lebed. True muonium ($\mu^+\mu^-$) on the light front. *J.Phys.*, G41(12):125003, 2014.

[229] Paul Wiecki, Yang Li, Xingbo Zhao, Pieter Maris, and James P. Vary. Basis Light-Front Quantization Approach to Positronium. *Phys. Rev.*, D91(10):105009, 2015.

[230] Satish Balay, Shrirang Abhyankar, Mark F. Adams, Jed Brown, Peter Brune, Kris Buschelman, Lisandro Dalcin, Victor Eijkhout, William D. Gropp, Dinesh Kaushik, Matthew G. Knepley, Lois Curfman McInnes, Karl Rupp, Barry F. Smith, Stefano Zampini, and Hong Zhang. PETSc users manual. Technical Report ANL-95/11 - Revision 3.6, Argonne National Laboratory, 2015.

[231] Satish Balay, William D. Gropp, Lois Curfman McInnes, and Barry F. Smith. Efficient management of parallelism in object oriented numerical software libraries. In E. Arge, A. M. Bruaset, and H. P. Langtangen, editors, *Modern Software Tools in Scientific Computing*, pages 163–202. Birkhäuser Press, 1997.

[232] Vicente Hernandez, Jose E. Roman, and Vicente Vidal. SLEPc: A scalable and flexible toolkit for the solution of eigenvalue problems. *ACM Trans. Math. Software*, 31(3):351–362, 2005.

[233] Henry Lamm. https://github.com/operabed/tmswift.git, 2016.

[234] V. A. Karmanov, J. Carbonell, and M. Mangin-Brinet. Stability of bound states in the light front Yukawa model. *AIP Conf. Proc.*, 603:271–274, 2001. [,271(2001)].

[235] J. Carbonell, M. Mangin-Brinet, and V. A. Karmanov. Two-body bound states in light front dynamics. In *14th International School on Nuclear Physics, Neutron Physics and Nuclear Energy Varna, Bulgaria, September 25-30, 2001*, 2002.

[236] U.D. Jentschura, G. Soff, V.G. Ivanov, and Savely G. Karshenboim. The Bound $\mu^+\mu^-$ system. *Phys. Rev.*, A56:4483, 1997.

[237] Robert Karplus and Abraham Klein. Electrodynamics displacement of atomic energy levels. 3. The Hyperfine structure of positronium. *Phys. Rev.*, 87:848–858, 1952.

[238] C. Itzykson and J. B. Zuber. *Quantum Field Theory*. International Series In Pure and Applied Physics. McGraw-Hill, New York, 1980.

[239] Dolors Eiras and Joan Soto. Light fermion finite mass effects in non-relativistic bound states. *Phys. Lett.*, B491:101–110, 2000.

[240] Vladimir G. Ivanov, Evgeny Yu. Korzinin, and Savely G. Karshenboim. Second-order corrections to the wave function at the origin in muonic hydrogen and pionium. *Phys. Rev.*, D80:027702, 2009.

[241] Tanja Branz, Thomas Gutsche, Valery E. Lyubovitskij, Ivan Schmidt, and Alfredo Vega. Light and heavy mesons in a soft-wall holographic approach. *Phys. Rev.*, D82:074022, 2010.

[242] G Breit. *Phys. Rev.*, 35:1477, 1930.

[243] blarg. blarg. *blarg*, blarg.

[244] James L. Anderson and Peter G. Bergmann. Constraints in covariant field theories. *Phys. Rev.*, 83:1018–1025, 1951.

[245] Kurt Sundermeyer. Constrained dynamics with applications to yang-mills theory, general relativity, classical spin, dual string model. 1982.

[246] Andrew Chun-Nien Tang. *Discretized light cone quantization: Application to quantum electrodynamics*. PhD thesis, Stanford U., Phys. Dept., 1990.

[247] V. A. Karmanov. Relativistic Deuteron Wave Function on Light Front. *Nucl. Phys.*, A362:331, 1981.

[248] Evert J Nyström. Über die praktische auflösung von integralgleichungen mit anwendungen auf randwertaufgaben. *Acta Mathematica*, 54(1):185–204, 1930.

[249] I. Tamm. Relativistic interaction of elementary particles. *J. Phys.(USSR)*, 9:449, 1945.

[250] S. M. Dancoff. Nonadiabatic meson theory of nuclear forces. *Phys. Rev.*, 78:382–385, 1950.

APPENDIX A

NOTATION

In this appendix is compiled the notation used in this work. Throughout, the convention used will be that of Lepage and Brodsky (LB)[243]

<center>Coordinates</center>

The *light-front coordinates* are defined by the relation

$$x^{\pm} \equiv (x^0 \pm x^3), \tag{A.1}$$

where x^+ is referred to as light-front time, and x^- is light-front position. The light-front metric used is

$$g^{\mu\nu} = \begin{pmatrix} 0 & 2 & 0 & 0 \\ 2 & 0 & 0 & 0 \\ 0 & 0 & -1 & 0 \\ 0 & 0 & 0 & -1 \end{pmatrix} \quad \text{and} \quad g_{\mu\nu} = \begin{pmatrix} 0 & \frac{1}{2} & 0 & 0 \\ \frac{1}{2} & 0 & 0 & 0 \\ 0 & 0 & -1 & 0 \\ 0 & 0 & 0 & -1 \end{pmatrix}, \tag{A.2}$$

where here and throughout this thesis are used the running of the Greek indices $(+, -, 1, 2)$. Latin indices $(i = 1, 2)$ are used to indicate the transverse directions. For the momentum coordinates in the same scheme $p^{\mu} = (p^+, p^-, \boldsymbol{p}_{\perp})$, where p^- is the so-called *light-front energy* of the particle. The scalar product is defined to be

$$x \cdot y = x^{\mu} y_{\mu} = x^+ y_+ + x^- y_- + x^1 y_1 + x^2 y_2 = \frac{1}{2}(x^+ y^- + x^- y^+) - \boldsymbol{x}_{\perp} \boldsymbol{y}_{\perp}. \tag{A.3}$$

In order to remove the overall momentum, the *relative momentum coordinates* are defined via

$$x_i \equiv \frac{p_i^+}{P^+} \quad \text{and} \quad \boldsymbol{k}_{\perp} = x_i \boldsymbol{P}_{\perp} - \boldsymbol{p}_{\perp,i}, \tag{A.4}$$

which are called, respectively, the *longitudinal momentum fraction* and the *transverse momentum fraction*. Assuming that $\boldsymbol{P}_{\perp} = 0$, which is done throughout this work, the following relations are satisfied:

$$\sum_i x_i = 1 \quad \text{and} \quad \sum_i \boldsymbol{k}_i = 0. \tag{A.5}$$

<center>Dirac Matrices</center>

The 4×4 Dirac matrices γ^{μ} are defined, independent of metric, by the relation

$$\gamma^{\mu}\gamma^{\nu} + \gamma^{\nu}\gamma^{\mu} = 2g^{\mu\nu}. \tag{A.6}$$

For the traditional instant-form matrices, γ^0 is a Hermitean matrix, while γ^k are anti-Hermitean. The standard combinations of $\beta = \gamma^0$ and $\alpha^k = \gamma^0 \gamma^k$, in addition to

$$\sigma^{\mu\nu} = \frac{1}{2}i[\gamma^{\mu}, \gamma^{\nu}], \quad \text{and} \quad \gamma^5 = \gamma_5 = i\gamma^0\gamma^1\gamma^2\gamma^3, \tag{A.7}$$

find some uses even in front-form quantization. These matrices are expressed in terms of the 2×2 *Pauli matrices*:

$$\mathbb{I} = \begin{pmatrix} 1 & 0 \\ 0 & 1 \end{pmatrix}, \quad \sigma^1 = \begin{pmatrix} 0 & 1 \\ 1 & 0 \end{pmatrix}, \quad \sigma^2 = \begin{pmatrix} 0 & -i \\ i & 0 \end{pmatrix}, \quad \text{and} \quad \sigma^3 = \begin{pmatrix} 1 & 0 \\ 0 & -1 \end{pmatrix}. \tag{A.8}$$

<center>88</center>

With Pauli matrices, we can represent the Dirac matrices in the *Dirac representation*

$$\gamma^0 = \begin{pmatrix} \mathbb{I} & 0 \\ 0 & -\mathbb{I} \end{pmatrix}, \quad \gamma_i = \begin{pmatrix} 0 & \sigma^i \\ -\sigma^i & 0 \end{pmatrix}, \quad \gamma_5 = \begin{pmatrix} 0 & \mathbb{I} \\ \mathbb{I} & 0 \end{pmatrix}. \tag{A.9}$$

These can be used to build up *projection operators* which are Hermitean matrices

$$\Lambda_\pm \equiv \frac{1}{2}\gamma^0\gamma^\pm = \frac{1}{2}\gamma^0(\gamma^0 \pm \gamma^3), \tag{A.10}$$

that have the properties

$$\Lambda_+ + \Lambda_- = \mathbb{I}, \quad \Lambda_+\Lambda_- = 0, \quad \Lambda_\pm^2 = \Lambda_\pm, \tag{A.11}$$

and can be explicitly written as

$$\Lambda_\pm = \frac{1}{2} \begin{pmatrix} 1 & 0 & \pm 1 & 0 \\ 0 & 1 & 0 & \mp 1 \\ \pm 1 & 0 & 1 & 0 \\ 0 & \mp 1 & 0 & 1 \end{pmatrix}. \tag{A.12}$$

On the light front, we introduce the new Dirac matrices

$$\gamma^\pm = \gamma^0 \pm \gamma^3, \tag{A.13}$$

which have the properties
$$\gamma^+\gamma^+ = \gamma^-\gamma^- = 0, \tag{A.14}$$
and alternating sets of these matrices simplify via

$$\gamma^+\gamma^-\gamma^+ = 4\gamma^+ \quad \text{and} \quad \gamma^-\gamma^+\gamma^- = 4\gamma^-. \tag{A.15}$$

Spinors, Polarization Vectors, and Projection Operators

The *Dirac spinors* $u_\alpha(p, \lambda)$ and $v_\alpha(p, \lambda)$ are solutions to the Dirac equation

$$(\not{p} - m)u(p, \lambda) = 0, \quad (\not{p} + m)v(p, \lambda) = 0, \tag{A.16}$$

which are orthonormal and complete:

$$\bar{u}(p, \lambda)u(p, \lambda') = -\bar{v}(p, \lambda')v(p, \lambda) = 2m\delta_{\lambda,\lambda'}, \tag{A.17}$$

$$\sum_\lambda u(p, \lambda)\bar{u}(p, \lambda) = \not{p} + m, \quad \sum_\lambda v(p, \lambda)\bar{v}(p, \lambda) = \not{p} - m. \tag{A.18}$$

The fermion fields can be separated into two different helicity eigenstates by

$$\psi_\pm = \Lambda_\pm\psi, \tag{A.19}$$

where the projection operators are defined above. The projected spinors in this work are defined as $u_+(\lambda) \equiv \chi(\lambda)$, while $v_+(\lambda) \equiv \chi(-\lambda)$. The spinors are

$$\chi(\uparrow) = \frac{1}{\sqrt{2}} \begin{pmatrix} 1 \\ 0 \\ 1 \\ 0 \end{pmatrix} \quad \text{and} \quad \chi(\downarrow) = \frac{1}{\sqrt{2}} \begin{pmatrix} 0 \\ 1 \\ 0 \\ -1 \end{pmatrix}. \tag{A.20}$$

These spinors then obey the relations

$$\chi^\dagger(\lambda)\chi(\lambda) = \delta_{\lambda,\lambda'} \tag{A.21}$$

$$\sum_\lambda \chi_\alpha(\lambda)\chi_\beta(\lambda') = \Lambda^+_{\alpha\beta}. \tag{A.22}$$

which form an orthonormal, complete set. Using these, the free-fermion field is given by

$$u(k,\lambda) = \frac{1}{\sqrt{k^+}}(k^+ + \beta m_f + \boldsymbol{\alpha}_\perp \cdot \boldsymbol{k}_\perp)\chi(\lambda) \tag{A.23}$$

$$v(k,\lambda) = \frac{1}{\sqrt{k^+}}(k^+ + \beta m_f + \boldsymbol{\alpha}_\perp \cdot \boldsymbol{k}_\perp)\chi(-\lambda) \tag{A.24}$$

$$\tag{A.25}$$

The *photon polarization vectors* $\epsilon_\mu(p,\lambda)$ can be labelled by their spin projection, $\lambda = \pm 1$. They have the properties of

$$\epsilon^\mu(p,\lambda)\epsilon^*_\mu(p,\lambda') = -\delta_{\lambda\lambda'} \quad \text{and} \quad p^\mu \epsilon_\mu(p,\lambda) = 0. \tag{A.26}$$

The polarization sum $d_{\mu\nu}(p)$ is

$$d_{\mu\nu}(p) = \sum_\lambda \epsilon_\mu(p,\lambda)\epsilon^*_\nu(p,\lambda) = -g_{\mu\nu} + \frac{\eta_\mu p_\nu + \eta_\nu p_\mu}{p^\kappa \eta_\kappa} \tag{A.27}$$

where the null vector $\eta^\mu \eta_\mu = 0$ and is given by $(0, 2, \boldsymbol{0}_\perp)$. The spin-projected polarization vectors are given by

$$\epsilon(\uparrow) = \frac{-1}{\sqrt{2}} \begin{pmatrix} 1 \\ i \end{pmatrix} \quad \text{and} \quad \epsilon(\downarrow) = \frac{1}{\sqrt{2}} \begin{pmatrix} 1 \\ -i \end{pmatrix}, \tag{A.28}$$

which are also complete and orthonormal:

$$\epsilon^*(\lambda)\epsilon(\lambda') = \delta_{\lambda,\lambda'}, \tag{A.29}$$

$$\sum_\lambda \epsilon_i(\lambda)\epsilon^*_j(\lambda') = \delta_{ij}. \tag{A.30}$$

Using these, the full polarization four-vector is given by

$$\epsilon^\mu(\lambda) = \begin{pmatrix} 0 \\ 2\frac{\boldsymbol{\epsilon}_\perp \cdot \boldsymbol{k}_\perp}{k^+} \\ \boldsymbol{\epsilon}_\perp(\lambda). \end{pmatrix} \tag{A.31}$$

Commutation Relations

Defining the commutation relations in light-front quantization has to be done more carefully than in instant-form. According to [244, 245], they can be derived for constrained dynamics from the Dirac-Bergmann algorithm:

$$\{\psi_{+\alpha}(x), \psi_{+\beta}^\dagger(y)\}_{x^+=x_0^+} = \frac{1}{2}\Lambda_{+\alpha\beta}\delta(x^- - y^-)\delta^2(\boldsymbol{x}_\perp - \boldsymbol{y}_\perp), \tag{A.32}$$

$$[A^i(x), \partial^+ A^j_{+\beta}(y)]_{x^+=x_0^+} = \frac{i}{2}\delta^{ij}\delta(x^- - y^-)\delta^2(\boldsymbol{x}_\perp - \boldsymbol{y}_\perp), \tag{A.33}$$

where $\psi(x)$ is a fermionic field, and $A^\mu(x)$ is a bosonic field. The expansion of the fields into Fourier modes give for the operator-valued coefficients relations:

$$\{b_{\lambda,n}, b_{\lambda',m}^\dagger\} = \{d_{\lambda,n}, d_{\lambda',m}^\dagger\} = \delta_{\lambda,\lambda'}\delta_{n^+,m^+}\delta^2_{\boldsymbol{n}_\perp,\boldsymbol{m}_\perp}, \tag{A.34}$$

$$[a_{\lambda,n}, a_{\lambda',m}^\dagger] = \delta_{\lambda,\lambda'}\delta_{n^+,m^+}\delta^2_{\boldsymbol{n}_\perp,\boldsymbol{m}_\perp}, \tag{A.35}$$

and any other commutators and anti-commutators vanish.

$|\gamma\gamma\rangle$ Interaction

In an effort to make the expressions needed to derive the full-sector integrals for the $|\gamma\gamma\rangle$ effective interaction, a number of non-standard notational simplfications are made, which are cataloged in this section. First, integral measures are given by

$$\int_k \equiv \int \mathrm{d}^2 k_\perp \mathrm{d}k^+. \tag{A.36}$$

To express three-component momentum conservation, the abbreviation used is

$$\delta^3(P) = \delta(P^+)\delta(\boldsymbol{P}_\perp). \tag{A.37}$$

Since time-ordered perturbation theory always results in the use of step functions, the compact theta functions are defined as

$$\Theta_k = \theta(k^+), \tag{A.38}$$

$$\Theta_{-k} = \theta((P-k)^+), \tag{A.39}$$

where P^+ is the total $+$ component at any time. For terms that involve the external momenta,

$$\Theta_{\pm i} = \theta(\pm(i-k)^+), \tag{A.40}$$

$$\Theta_{i-j} = \theta((i-k)^+)\theta(-(j-k)^+), \tag{A.41}$$

where k is always the k^μ photon's $+$ component. For the $\eta^\mu\eta^\nu$ products is introduced the tensor $\eta_{\mu\nu}$, which is zero except for the $\eta_{++} = 1$ component. A set of compact notation for the non-perturbative propagators together with some constant factors is defined as

$$\Delta_i = \left(\frac{e}{\sqrt{2}(2\pi)^{3/2}}\right)^4 \frac{G_i}{\sqrt{p^+ o^+ (o')^+ (p')^+}}, \tag{A.42}$$

where $i = \gamma\gamma, 4\ell, 0$ is an index indicating its sector, and 0 indicates neither of the two sectors. $G_0 = 1$ terms appears because the particular diagram has instantaneous terms.

For the case where pairs of momentum cannot be separated in the $-$ component, the bracket notation is utilized

$$[p - k]^\mu = (p^+ - k^+, \frac{m_q^2 + (\boldsymbol{p}_\perp - \boldsymbol{k}_\perp)^2}{p^+ - k^+}, \boldsymbol{p}_\perp - \boldsymbol{k}_\perp). \tag{A.43}$$

APPENDIX B

QUANTUM ELECTRODYNAMICS IN FRONT FORM

In this appendix, the Hamiltonian operator for QED$_{3+1}$ in the front form will be derived. The start for this is the *Lagrangian density* given by

$$\mathcal{L}_{QED} = -\frac{1}{4}F_{\mu\nu}F^{\mu\nu} + \bar{\psi}\left(i\slashed{D} - m_\ell\right)\psi. \tag{B.1}$$

In this density, the *covariant derivative* is define by

$$D_\mu \equiv \partial_\mu + ieA_\mu. \tag{B.2}$$

The slash notation $\slashed{p} = \gamma^\mu p_\mu$ has been utilized, and the Abelian $U(1)$ *field strength tensor* is defined by

$$F^{\mu\nu} \equiv \partial^\mu A^\nu - \partial^\nu A^\mu. \tag{B.3}$$

From the Lagrangian density, it is possible to derive the classical equations of motion. For the gauge field, these equation of motion are the Maxwell equations:

$$\partial_\mu F^{\mu\nu} = e\bar{\psi}\gamma^\nu\psi, \tag{B.4}$$

and for the leptons the equations of motion are given by the *Dirac equation*:

$$(i\slashed{D} - m_\ell)\psi = 0. \tag{B.5}$$

Before proceeding to quantize, the variables used are changed to light-front coordinates described in appendix A. The scalar products that are in the Lagrangian density, as well as the eventual terms in the Hamiltonian operator, will be represented using $\gamma^\pm$ and γ^i. Also, it is useful to use the helicity-projected fields $\psi_\pm$. As explained in Chapter 2, a Hamiltonian formalism requires gauge fixing, and throughout this thesis the light-cone gauge is used:

$$A^+ = A^0 + A^3 = 0. \tag{B.6}$$

With these specifications, the derivation of the the *light-cone energy* P^- can be performed, and in this appendix the traditional derivation of Tang will be followed[246]. For this, first, the expression for the canonical momenta of generic fields ϕ is defined as

$$\pi_\phi = \frac{\partial\mathcal{L}}{\partial(\partial_+\phi)}. \tag{B.7}$$

For each of the fields, the canonical momenta are easily found from the Lagrangian density. For the fermions, they are

$$\pi_{\psi_+} = i\psi_+^\dagger, \quad \pi_{\psi_+^\dagger} = -i\psi_+, \quad \pi_{\psi_-} = 0, \quad \pi_{\psi_-^\dagger} = 0. \tag{B.8}$$

In the case of the gauge fields, the momenta are

$$\pi_{A_i} = -\partial^+ A^i, \quad \pi_{A_+} = 0. \tag{B.9}$$

From the expressions, it can be seen that there are fields without canonical momenta. This indicates that the dynamics of the system are constrained and that these fields need to be removed from the theory. This is done by solving the classical equations

94

of motion for each of these $\pi_\phi = 0$ fields and then replacing them throughout the Hamiltonian by the derived expressions. The equations of motion can be obtained in the usual way from the Euler-Lagrange equation,

$$\partial_\mu \frac{\partial \mathcal{L}}{\partial(\partial_\mu \phi)} = \frac{\partial \mathcal{L}}{\partial \phi}. \tag{B.10}$$

Applying these for the fields of concern:

$$i\partial^+ \psi_- = \left(-i\overleftarrow{\partial}_i \alpha_i + gA_i\alpha^i + \beta m_\ell\right)\psi_+,$$

$$i\partial^+ \psi_-^\dagger = \psi_+^\dagger \left(i\overleftarrow{\partial}_i \alpha_i + gA_i\alpha^i + \beta m_\ell\right),$$

$$(i\partial^+)^2 A^- = 2\partial^+ \partial_i A^i + 4g\psi_+^\dagger \psi_+, \tag{B.11}$$

where the symbol $\overleftarrow{\partial}_i$ indicates a derivative acting to the left. Formally, these equations can now be inverted by defining a term $\phi = (\frac{1}{\partial^+})f$ which is the solution of $\partial^+ \phi = f$ (where f is a function). Doing this, expressions for each of the fields can be obtained

$$\psi_- = \frac{1}{i\partial^+}\left(-i\overleftarrow{\partial}_i \alpha_i + gA_i\alpha^i + \beta m_\ell\right)\psi_+,$$

$$\psi_-^\dagger = \frac{1}{i\partial^+}\psi_+^\dagger \left(i\overleftarrow{\partial}_i \alpha_i + gA_i\alpha^i + \beta m_\ell\right),$$

$$A^- = \frac{2}{(i\partial^+)^2}\partial^+ \partial_i A^i + \frac{4g}{(i\partial^+)^2}\psi_+^\dagger \psi_+. \tag{B.12}$$

While formally these expression are true, the reader should be troubled by the seemingly ill-defined operator $\frac{1}{\partial^+}$. Once boundary conditions have been imposed, these terms can be show to be simply Green's functions (albeit non-unique ones). With these solutions, the only independent degrees of freedom that exist are ψ_+ and the physical, transverse photons $\boldsymbol{A}_\perp$. Expressing $\mathcal{P}^- = 2\sum_\phi \pi_\phi \partial_+ \phi - 2\mathcal{L}$ in terms of these independent fields and the light-front variables gives

$$\mathcal{P}^- = \mathcal{P}_0^- + g\mathcal{P}_1^- + g^2\mathcal{P}_2^-, \tag{B.13}$$

where each of the terms is given by

$$
\begin{aligned}
\mathcal{P}_0^- =& \partial^i A^j \partial^i A^j - \partial^i A^j \partial^j A^i + \left\{ i\partial^+ i\partial_i A^i \frac{1}{(i\partial^+)^2} i\partial^+ i\partial_j A^j \right\}_{\text{sym}} \\
& + 2 \left\{ \psi_+^\dagger [-i\partial_i \alpha^i + \beta m_\ell] \frac{1}{i\partial^+} [-i\partial_j \alpha^j + \beta m_\ell] \psi_+ \right\}_{\text{sym}}, \\
\mathcal{P}_1^- =& - 2 \left\{ \psi_+^\dagger A^i \alpha^i \frac{1}{i\partial^+} [-i\partial_i \alpha^i + \beta m_\ell] \psi_+ \right\} \\
& - 2 \left\{ \psi_+^\dagger \left[i\overleftarrow{\partial_i} \alpha^i + \beta m_e \right] \frac{1}{i\partial^+} A^i \alpha^j \psi_+ \right\} \\
& - 4 \left\{ \psi_+^\dagger \psi_+ \frac{1}{(i\partial^+)^2} i\partial^+ i\partial_i A^i \right\}_{\text{sym}}, \\
\mathcal{P}_2^- =& 2 \left\{ \psi_+^\dagger A^i \alpha^i \frac{1}{i\partial^+} A^j \alpha^j \psi_+ \right\}_{\text{sym}} + 4 \left\{ \psi_+^\dagger \psi_+ \frac{1}{(i\partial^+)^2} \psi_+^\dagger \psi_+ \right\}_{\text{sym}}. \quad \text{(B.14)}
\end{aligned}
$$

The so-called symmetric brackets are defined by

$$
\begin{aligned}
\left\{ A \frac{1}{i\partial^+} B \right\}_{sym} &\equiv \frac{1}{2} \left[A \frac{1}{i\partial^+} B - \left(\frac{1}{i\partial^+} A \right) B \right], \\
\left\{ A \frac{1}{(i\partial^+)^2} B \right\}_{sym} &\equiv A \frac{1}{(i\partial^+)^2} B + \left(\frac{1}{i\partial^+} A \right) \left(\frac{1}{i\partial^+} B \right) + \left(\frac{1}{(i\partial^+)^2} A \right) B. \quad \text{(B.15)}
\end{aligned}
$$

With the system fully specified now, it can be quantized by imposing the canonical commutation relations found in Appendix A, which can be consistently derived from Dirac's method for constrained Hamiltonians. A bilinear term that couples to the gauge fields forces them to have periodic boundary conditions in order to properly define the $1/\partial^+$ operation. In contrast, the fermionic fields have no particular constraint on them, but are generally taken to be anti-periodic since this forces the zero-modes in the longitudinal fermionic field to be zero. The fields themselves can be given by an expansion in Fourier modes:

$$
\psi_+(x) = \frac{1}{\sqrt{2(2\pi)^3}} \sum_\lambda \int_0^\infty \frac{dk^+}{\sqrt{k^+}} \int_{-\infty}^\infty d^2 k_\perp \left[b(\boldsymbol{k}, \lambda) u_+(\lambda) e^{-i\boldsymbol{k}\cdot\boldsymbol{x}} + d^\dagger(\boldsymbol{k}, \lambda) u_+(\lambda) e^{i\boldsymbol{k}\cdot\boldsymbol{x}} \right],
$$
$$
\text{(B.16)}
$$
$$
A^i(x) = \frac{1}{\sqrt{2(2\pi)^3}} \sum_\lambda \int_0^\infty \frac{dk^+}{\sqrt{k^+}} \int_{-\infty}^\infty d^2 k_\perp \left[a(\boldsymbol{k}, \lambda) \epsilon^i(\lambda) e^{-i\boldsymbol{k}\cdot\boldsymbol{x}} + a^\dagger(\boldsymbol{k}, \lambda) \epsilon^{*i}(\lambda) e^{i\boldsymbol{k}\cdot\boldsymbol{x}} \right].
$$
$$
\text{(B.17)}
$$

where the spinors $u_+(\lambda)$ and the polarization vectors $\epsilon^i(\lambda)$ were defined in Appendix A. From this, and the field commutation relations, it is possible to derive the operator commutation relations also found in Appendix A. With these relations and $\mathcal{P}^-$, it is straight forward to derive the operators found in Appendix C.

APPENDIX C

MATRIX ELEMENTS OF LIGHT-CONE GAUGE QED

As discussed in Chapter 2, the Hamiltonian can be described by the sum of a kinetic operator T and various types of interactions: *seagulls* S [and their normal-ordered *contractions* C], which do not change particle number, *vertices* V, which change particle number by one, and *forks* F, which change particle number by two:

$$H_{\text{LC}} = T + V + S + C + F \,. \tag{C.1}$$

The kinetic operator T is given by the sum of over each of the particles in the state:

$$T = \sum_i \frac{m_{\ell,i}^2 + \boldsymbol{k}_{\perp,i}^2}{x_i} (b_i^\dagger b_i + d_i^\dagger d_i) + \sum_j \frac{\boldsymbol{k}_{\perp,j}}{x_j} a_j^\dagger a_j \,. \tag{C.2}$$

In this thesis, the creation operators are defined to create plane waves for the fermions and photons. These particles are determined by their quantum numbers, $x, \boldsymbol{k}_\perp$, and λ. The matrix elements in this thesis follow the standard convention. Solid lines with arrows indicate fermions and anti-fermions, depending on the direction of their arrow with respect to time. Wavy lines indicate a photon.

Although the total Hamiltionian involves fork operators, in the limited Fock space considered in the $\ell^+\ell^-$ model, there is no need to include them. Therefore they are absent from the tables in this appendix. For their expressions, consult Ref. [2].

Feynman Diagram	Matrix Element	Helicity

$$V_{\ell^-\to\ell^-\gamma} = bg\frac{m_\ell}{\sqrt{x_3}}\left(\frac{1}{x_2}-\frac{1}{x_1}\right) \qquad\qquad \times\,\delta^{\lambda_1}_{\lambda_2}\delta^{\lambda_1}_{\lambda_3}$$

$$+\,bg\sqrt{\frac{2}{x_3}}\,\boldsymbol{\epsilon}_\perp(\lambda_3)\left(\frac{\boldsymbol{k}_{\perp,3}}{x_3}-\frac{\boldsymbol{k}_{\perp,2}}{x_2}\right) \qquad \times\,\delta^{\lambda_1}_{\lambda_2}\delta^{\lambda_1}_{-\lambda_3}$$

$$+\,bg\sqrt{\frac{2}{x_3}}\,\boldsymbol{\epsilon}_\perp(\lambda_3)\left(\frac{\boldsymbol{k}_{\perp,3}}{x_3}-\frac{\boldsymbol{k}_{\perp,1}}{x_1}\right) \qquad \times\,\delta^{\lambda_1}_{-\lambda_2}\delta^{\lambda_1}_{\lambda_3}$$

$$V_{\gamma\to\ell^+\ell^-} = bg\frac{m_\ell}{\sqrt{x_1}}\left(\frac{1}{x_2}+\frac{1}{x_3}\right) \qquad\qquad \times\,\delta^{\lambda_1}_{\lambda_2}\delta^{\lambda_1}_{\lambda_3}$$

$$-\,bg\sqrt{\frac{2}{x_1}}\,\boldsymbol{\epsilon}_\perp(\lambda_1)\left(\frac{\boldsymbol{k}_{\perp,1}}{x_1}-\frac{\boldsymbol{k}_{\perp,3}}{x_3}\right) \qquad \times\,\delta^{\lambda_1}_{\lambda_2}\delta^{\lambda_1}_{-\lambda_3}$$

$$-\,bg\sqrt{\frac{2}{x_1}}\,\boldsymbol{\epsilon}_\perp(\lambda_1)\left(\frac{\boldsymbol{k}_{\perp,1}}{x_1}-\frac{\boldsymbol{k}_{\perp,2}}{x_2}\right) \qquad \times\,\delta^{\lambda_1}_{-\lambda_2}\delta^{\lambda_1}_{\lambda_3}$$

$$V = \sum_{\text{all QN}}\left(b_1^\dagger b_2 a_3 - d_1^\dagger d_2 a_3\right) V_{\ell^-\to\ell^-\gamma}(1;2,3)$$

$$+\sum_{\text{all QN}}\left(a_3^\dagger b_2^\dagger b_1 - a_3^\dagger d_2^\dagger d_1\right) V^*_{\ell^-\to\ell^-\gamma}(1;2,3)$$

$$+\sum_{\text{all QN}}\left[a_1^\dagger b_2 d_3 V^*_{g\to\ell^+\ell^-}(1;2,3) + d_3^\dagger b_2^\dagger a_1 V_{\gamma\to\ell^+\ell^-}(1;2,3)\right]$$

Table C.1: Matrix elements for the vertex interactions. It should be noted that the $V_{\ell^-\to\ell^-\gamma}$ element given here corrects an error in [1].

Feynman Diagram	Matrix Element	Helicity
	$$S^{(s)}_{\ell^+\ell^-\to\ell^+\ell^-} = \tilde{g}^2 \frac{2}{(x_1-x_3)^2}$$	$\times\delta^{\lambda_1}_{\lambda_3}\delta^{\lambda_2}_{\lambda_4}$
	$$S^{(a)}_{\ell^+\ell^-\to\ell^+\ell^-} = \tilde{g}^2 \frac{-2}{(x_1+x_2)^2}$$	$\times\delta^{\lambda_1}_{-\lambda_2}\delta^{\lambda_3}_{-\lambda_4}$
	$$S^{(a)}_{\ell^-\gamma\to\ell^-\gamma} = \tilde{g}^2 \frac{1}{x_1+x_2}\frac{1}{\sqrt{x_2 x_4}}$$	$\times\delta^{\lambda_1}_{-\lambda_2}\delta^{\lambda_1}_{\lambda_3}\delta^{\lambda_1}_{-\lambda_4}$
	$$S^{(s)}_{\ell^-\gamma\to\ell^-\gamma} = \tilde{g}^2 \frac{1}{x_1-x_4}\frac{1}{\sqrt{x_2 x_4}}$$	$\times\delta^{\lambda_1}_{\lambda_2}\delta^{\lambda_1}_{\lambda_3}\delta^{\lambda_1}_{\lambda_4}$

$$S = \sum_{\text{all QN}} b_1^\dagger d_2^\dagger b_3 d_4 \left[S^{(s)}_{\ell^+\ell^-\to\ell^+\ell^-}(1,2;3,4) + S^{(a)}_{\ell^+\ell^-\to\ell^+\ell^-}(1,2;3,4) \right]$$

$$+ \sum_{\text{all QN}} \left(b_1^\dagger a_2^\dagger b_3 a_4 + d_1^\dagger a_2^\dagger d_3 a_4 \right) \left[S^{(s)}_{\ell^-\gamma\to\ell^-\gamma}(1,2;3,4) + S^{(a)}_{\ell^-\gamma\to\ell^-\gamma}(1,2;3,4) \right]$$

Table C.2: Matrix elements of the seagull interactions used in the true muonium model. The exhaustive table of seagull diagrams can by found in [2]. It should be noted that the $S^{(a)}_{\ell^+\ell^-\to\ell^+\ell^-}$ element given here corrects for an error in [1].

Feynman Diagram	Matrix Element
	$$C_{\ell^-}^{(\gamma)}(1) = \tilde{g}^2 \sum_{x',\boldsymbol{k}'_\perp}^{\infty} \left(\frac{1}{(x_1 - x')^2} - \frac{1}{(x_1 + x')^2} \right)$$
	$$C_{\ell^-}^{(\ell^-)}(1) = \tilde{g}^2 \sum_{x',\boldsymbol{k}'_\perp}^{\infty} \left(\frac{1}{x'(x_1 + x')} + \frac{1}{x'(x_1 - x')} \right)$$
	$$C_{\gamma}^{(\ell^-)}(1) = -\tilde{g}^2 \sum_{x',\boldsymbol{k}'_\perp}^{\infty} \left(\frac{1}{x_1(x' + x_1)} + \frac{1}{x_1(x' - x_1)} \right)$$

$$C = \sum_{\text{all QN}} \left[\left(b_1^\dagger b_1 - d_1^\dagger d_1 \right) \left(C_{\ell^-}^{(\gamma)}(1) + C_{\ell^-}^{(\ell^-)}(1) \right) + a_1^\dagger a_1 C_{\gamma}^{(\ell^-)}(1) \right]$$

Table C.3: Matrix elements for the contractions.

APPENDIX D

EFFECTIVE MATRIX ELEMENTS FOR $\ell\ell$ MODEL

In this appendix are derived effective matrix elements $F_n(x, \boldsymbol{k}_\perp, x', \boldsymbol{k}'_\perp; \lambda_1, \lambda_2)$. Although there are sixteen of these functions in the exchange channel and another sixteen in the annihilation channel, they can be expressed by four helicity-independent functions, $F_i(x, \boldsymbol{k}_\perp; x', \boldsymbol{k}'_\perp)$, in each channel. After deriving these functions, we will tabulate them into helicity tables for use in computing the spectrum.

Calculation of Elements

In order to extract the helicity interaction elements, one starts with the interaction operators given in Appendix C. Combining all the elements for the dynamical-exchange interaction with both time orderings, and the splitting them based on their γ^μ-structure, Table D.1 is derived.

$\mathcal{M}$	$\dfrac{1}{\sqrt{k^+ k'^+}} \bar{u}(k, \lambda) \mathcal{M} u(k', \lambda')$
γ^+	$2\delta^\lambda_{\lambda'}$
γ^-	$\dfrac{2}{k^+ k'^+} \left[\left(m^2 + k_\perp k'_\perp e^{i\lambda'(\varphi - \varphi')} \right) \delta^\lambda_{\lambda'} + m\lambda' \left(k_\perp e^{+i\lambda'\varphi} - k'_\perp e^{+i\lambda'\varphi'} \right) \delta^\lambda_{-\lambda'} \right]$
γ_1	$\left(\dfrac{k_\perp}{k^+} e^{-i\lambda'\varphi} + \dfrac{k'_\perp}{k^{+'}} e^{+i\lambda'\varphi'} \right) \delta^\lambda_{\lambda'} - m\lambda' \left(\dfrac{1}{k^+} - \dfrac{1}{k^{+'}} \right) \delta^\lambda_{-\lambda'}$
γ_2	$-i\lambda' \left(\dfrac{k_\perp}{k^+} e^{-i\lambda'\varphi} - \dfrac{k'_\perp}{k^{+'}} e^{+i\lambda'\varphi'} \right) \delta^\lambda_{\lambda'} - im \left(\dfrac{1}{k^+} - \dfrac{1}{k^{+'}} \right) \delta^\lambda_{-\lambda'}$

Table D.1: Matrix elements of the Dirac spinors.

The definition of a general matrix element of the Hamiltonian for the exchange diagram is is

$$F_n(x, \boldsymbol{k}_\perp, x', \boldsymbol{k}'_\perp; \lambda_1, \lambda_2) = \frac{\langle x, \vec{k}_\perp; \lambda_1, \lambda_2 | j(l_e)^\mu j(l_{\bar{e}}) | x', \vec{k}'_\perp; s'_1, s'_2 \rangle}{\sqrt{xx'(1-x)(1-x')}} = \langle \mathcal{M}_e \mathcal{M}_{\bar{e}} \rangle, \quad \text{(D.1)}$$

which, from the definition of the γ^μ elements, is

$$\langle \mathcal{M}_e \mathcal{M}_{\bar{e}} \rangle = \frac{1}{2} \left(\frac{1}{2} \langle \gamma^+_e \gamma^-_{\bar{e}} \rangle + \frac{1}{2} \langle \gamma^-_e \gamma^+_{\bar{e}} \rangle - \langle \gamma^1_e \gamma^1_{\bar{e}} \rangle - \langle \gamma^2_e \gamma^2_{\bar{e}} \rangle \right). \quad \text{(D.2)}$$

Notation

For a function, $F_i(x, \boldsymbol{k}_\perp; x', \boldsymbol{k}'_\perp)$, the following operations are defined: an asterisk denotes a permutation of the particle and the antiparticle

$$F_3^*(x, \boldsymbol{k}_\perp; x', \boldsymbol{k}'_\perp) = F_3(1 - x, -\boldsymbol{k}_\perp; 1 - x', -\boldsymbol{k}'_\perp), \quad \text{(D.3)}$$

and a tilde represents the exchange operation of $J_z \to -J_z$

$$\tilde{F}_i(n) = F_i(-n) \tag{D.4}$$

From the φ-dependent elements, we integrate to obtain the J_z-index elements.

General helicity table for the exchange channel

final : initial	$(\lambda_1', \lambda_2') = \uparrow\uparrow$	$(\lambda_1', \lambda_2') = \uparrow\downarrow$	$(\lambda_1', \lambda_2') = \downarrow\uparrow$	$(\lambda_1', \lambda_2') = \downarrow\downarrow$
$(\lambda_1, \lambda_2) = \uparrow\uparrow$	$E_1(\vec{k}, \vec{k}')$	$E_3^*(\vec{k}, \vec{k}')$	$E_3(\vec{k}, \vec{k}')$	0
$(\lambda_1, \lambda_2) = \uparrow\downarrow$	$\tilde{E}_3^*(\vec{k}', \vec{k})$	$E_2(\vec{k}, \vec{k}')$	$E_4(\vec{k}, \vec{k}')$	$-E_3(\vec{k}', \vec{k})$
$(\lambda_1, \lambda_2) = \downarrow\uparrow$	$\tilde{E}_3(\vec{k}', \vec{k})$	$E_4(\vec{k}, \vec{k}')$	$\tilde{E}_2(\vec{k}, \vec{k}')$	$-E_3^*(\vec{k}', \vec{k})$
$(\lambda_1, \lambda_2) = \downarrow\downarrow$	0	$-\tilde{E}_3(\vec{k}, \vec{k}')$	$-\tilde{E}_3^*(\vec{k}, \vec{k}')$	$\tilde{E}_1(\vec{k}, \vec{k}')$

Table D.2: General helicity table of the effective interaction in the exchange channel.

The functions $E_i(\vec{k}, \vec{k}') := E_i(x, \boldsymbol{k}_\perp; x', \boldsymbol{k}_\perp')$ read

$$E_1(x, \vec{k}; x', \vec{k}') = \frac{\alpha}{2\pi^2} G_{\ell+\ell-\gamma} \left[m_\ell^2 \left(\frac{1}{xx'} + \frac{1}{(1-x)(1-x')} \right) \right.$$
$$\left. + \frac{k_\perp k_\perp'}{xx'(1-x)(1-x')} e^{-i(\varphi-\varphi')} \right], \tag{D.5}$$

$$E_2(x, \vec{k}; x', \vec{k}') = \frac{\alpha}{2\pi^2} G_{\ell+\ell-\gamma} \left(m_\ell^2 + k_\perp k_\perp' e^{-i(\varphi+\varphi')} \right) \left(\frac{e^{2i\varphi'}}{xx'} + \frac{e^{2i\varphi}}{(1-x)(1-x')} \right) \tag{D.6}$$

$$+ \frac{\alpha}{2\pi^2} G_{\ell+\ell-\gamma} \left(\frac{k_\perp^2}{x(1-x)} + \frac{k_\perp'^2}{x'(1-x')} \right), \tag{D.7}$$

$$E_3(x, \vec{k}; x', \vec{k}') = -\frac{\alpha}{2\pi^2} G_{\ell+\ell-\gamma} \frac{m_\ell}{xx'} \left(k_\perp' e^{-i\varphi'} - k_\perp \frac{1-x'}{1-x} e^{-i\varphi} \right), \tag{D.8}$$

$$E_4(x, \vec{k}; x', \vec{k}') = -\frac{\alpha}{2\pi^2} G_{\ell+\ell-\gamma} m_\ell^2 \frac{(x'-x)^2}{xx'(1-x')(1-x)}. \tag{D.9}$$

where the non-perturbative propagator $G_{\ell+\ell-\gamma}$ is given explicitly by

$$G_{\ell+\ell-\gamma}^{-1} \equiv -(x-x')^2 \frac{m_\ell^2}{2} \left(\frac{1}{xx'} + \frac{1}{(1-x)(1-x')} \right) + 2k_\perp k_\perp' \cos(\varphi-\varphi') \tag{D.10}$$

$$- \left(k_\perp^2 + k_\perp'^2 \right) + (x-x') \left[\frac{k_\perp'^2}{2} \left(\frac{1}{1-x'} - \frac{1}{x'} \right) - \frac{k_\perp^2}{2} \left(\frac{1}{1-x} - \frac{1}{x} \right) \right]. \tag{D.11}$$

The helicity table for the exchange channel for J_z

From the table in the previous section, we can obtain the exchange elements for $J_z = n$. Following the description in Chapter 3, one obtains the helicity table in Table D.3.

final : initial	$(\lambda_1', \lambda_2') =\uparrow\uparrow$	$(\lambda_1', \lambda_2') =\uparrow\downarrow$	$(\lambda_1', \lambda_2') =\downarrow\uparrow$	$(\lambda_1', \lambda_2') =\downarrow\downarrow$
$(\lambda_1, \lambda_2) =\uparrow\uparrow$	$G_1(1,2)$	$G_3^*(1,2)$	$G_3(1,2)$	0
$(\lambda_1, \lambda_2) =\uparrow\downarrow$	$G_3^*(2,1)$	$G_2(1,2)$	$G_4(1,2)$	$-\tilde{G}_3(2,1)$
$(\lambda_1, \lambda_2) =\downarrow\uparrow$	$G_3(2,1)$	$G_4(1,2)$	$\tilde{G}_2(1,2)$	$-\tilde{G}_3^*(2,1)$
$(\lambda_1, \lambda_2) =\downarrow\downarrow$	0	$-\tilde{G}_3(1,2)$	$-\tilde{G}_3^*(1,2)$	$\tilde{G}_1(1,2)$

Table D.3: Helicity table of the effective interaction for $J_z = \pm n$, $x > x'$.

The functions $G_i(1,2) = G_i(x, k_\perp; x', k_\perp')$ are given by

$$
G_1(x, k_\perp; x', k_\perp') = m_\ell^2 \left(\frac{1}{xx'} + \frac{1}{(1-x)(1-x')} \right) Int(|1-n|)
$$
$$
+ \frac{k_\perp k_\perp'}{xx'(1-x)(1-x')} Int(|n|), \tag{D.12}
$$

$$
G_2(x, k_\perp; x', k_\perp') = \left[m_\ell^2 \left(\frac{1}{xx'} + \frac{1}{(1-x)(1-x')} \right) + \frac{k_\perp^2}{x(1-x)} + \frac{k_\perp'^2}{x'(1-x')} \right] Int(|n|)
$$
$$
+ k_\perp k_\perp' \left[\frac{Int(|1-n|)}{xx'} + \frac{Int(|1+n|)}{(1-x)(1-x')} \right] + \left\{ \frac{2}{x + x' - 2xx'} \delta_{J_z,0} \right\}, \tag{D.13}
$$

$$
G_3(x, k_\perp; x', k_\perp') = - m_\ell \frac{1}{xx'} \left[k_\perp' Int(|1+n|) - k_\perp \frac{1-x'}{1-x} Int(|n|) \right], \tag{D.14}
$$

$$
G_4(x, k_\perp; x', k_\perp') = - m_\ell^2 \frac{(x-x')^2}{xx'(1-x')(1-x)} Int(|n|). \tag{D.15}
$$

In $G_2(x, k_\perp; x', k_\perp')$, the final term in braces is a regularization term used to stabilize the $k_\perp \to \infty$ limit. The derivation of the term is found in Chapter 3. The function $Int(n)$ is defined as

$$
Int(n) = \frac{\alpha}{\pi}(-A)^{-n+1} \left(\frac{B}{k_\perp k_\perp'} \right)^n. \tag{D.16}
$$

In these expressions we use the variables:

$$
a = (x-x')^2 \frac{m_\ell^2}{2} \left(\frac{1}{xx'} + \frac{1}{(1-x)(1-x')} \right) + k_\perp^2 + k_\perp'^2 \tag{D.17}
$$
$$
- \frac{1}{2}(x-x') \left[k_\perp'^2 \left(\frac{1}{1-x'} - \frac{1}{x'} \right) - k_\perp^2 \left(\frac{1}{1-x} - \frac{1}{x} \right) \right], \tag{D.18}
$$

105

and

$$A = \frac{1}{\sqrt{a^2 - 4k_\perp^2 k_\perp'^2}}, \tag{D.19}$$

$$B = \frac{1}{2}\left(1 - aA\right). \tag{D.20}$$

The helicity table for the annihilation channel for J_z

In contrast to the exchange channel, the annihilation channel has φ dependence only through the phase, and therefore these integrals can be done trivially. The results are shown in Table D.4.

$\ell\bar{\ell} : \ell'\bar{\ell}'$	$(\lambda_1', \lambda_2') =\uparrow\uparrow$	$(\lambda_1', \lambda_2') =\uparrow\downarrow$	$(\lambda_1', \lambda_2') =\downarrow\uparrow$	$(\lambda_1', \lambda_2') =\downarrow\downarrow$
$(\lambda_1, \lambda_2) =\uparrow\uparrow$	$I_1(1,2)$	$I_3(2,1)$	$I_3^*(2,1)$	0
$(\lambda_1, \lambda_2) =\uparrow\downarrow$	$I_3(1,2)$	$I_2^*(1,2)$	$I_4(2,1)$	0
$(\lambda_1, \lambda_2) =\downarrow\uparrow$	$I_3^*(1,2)$	$I_4(1,2)$	$I_2(1,2)$	0
$(\lambda_1, \lambda_2) =\downarrow\downarrow$	0	0	0	0

Table D.4: Helicity table of the annihilation graph for $J_z = 0, 1$ where the $\ell'\bar{\ell}'$ is the initial state and $\ell\bar{\ell}$ is the final state.

For this table, we have the matrix elements

$$I_1(x, k_\perp; x', k_\perp') := \frac{2\alpha}{\pi} G_\gamma m_{\ell'} m_\ell \left(\frac{1}{x} + \frac{1}{1-x}\right)\left(\frac{1}{x'} + \frac{1}{1-x'}\right)\delta_{|J_z|,1}, \tag{D.21}$$

$$I_2(x, k_\perp; x', k_\perp') := \frac{2\alpha}{\pi}\left[G_\gamma \frac{k_\perp k_\perp'}{xx'}\delta_{|J_z|,1} + 2\delta_{J_z,0}\right], \tag{D.22}$$

$$I_3(x, k_\perp; x', k_\perp') := \frac{2\alpha}{\pi} G_\gamma m_\ell \lambda_1 \left(\frac{1}{x} + \frac{1}{1-x}\right)\frac{k_\perp'}{1-x'}\delta_{|J_z|,1}, \tag{D.23}$$

$$I_4(x, k_\perp; x', k_\perp') := -\frac{2\alpha}{\pi}\left[G_\gamma \frac{k_\perp k_\perp'}{x'(1-x)}\delta_{|J_z|,1} - 2\delta_{J_z,0}\right]. \tag{D.24}$$

To obtain the elements $\langle\ell'\bar{\ell}'|\gamma|\ell\bar{\ell}\rangle$, only the inversion of $m_{\ell'} \leftrightarrow m_\ell$ need be performed, because the complex phases have been integrated out. The table for $J_z = -1$ is obtained by inverting *all* helicities. Note that the table has non-vanishing matrix elements for $|J_z| \leq 1$ only. This restriction is due to the angular momentum of the photon. For these elements, the non-perturbative propagator G_γ is given by only the inverse of the symmetric mass:

$$G_\gamma^{-1} = \frac{1}{2}\left(\frac{m_\ell^2 + k_\perp^2}{x(1-x)} + \frac{m_{\ell'}^2 + k_\perp'^2}{x'(1-x')}\right). \tag{D.25}$$

APPENDIX E

NUMERICAL IMPLEMENTATION

In order to solve the effective integral equation found in Chapter 2, several numerical improvements are implemented. These techniques are described in this appendix.

Change of Variables

As expressed in Appendix A, the relative momentum of the particle and antiparticle in the system are given by

$$\sum_i \boldsymbol{p}_i = \boldsymbol{p}_\ell + \boldsymbol{p}_{\ell'} = 0. \tag{E.1}$$

Instead of using the Cartesian variables, $(x, \boldsymbol{k}_\perp)$, it is numerically superior to use the polar coordinates utilized initially by Karmanov[247] to study a toy model of deuteron and followed upon by Sawicki[126, 125] in studying relativistic scalar field bound states on the light front. These coordinates are defined by

$$\boldsymbol{p} = (\mu \sin\theta \cos\varphi, \mu \sin\theta \sin\varphi, \mu \cos\theta). \tag{E.2}$$

The $+$ momentum component of the particle and antiparticle are

$$p_\ell^+ = E + p_z \qquad \text{and} \qquad p_{\ell'}^+ = E - p_z, \tag{E.3}$$

where $E = \sqrt{m_\ell^2 + \boldsymbol{p}^2}$. Using these, the light-front coordinates $(x, \boldsymbol{k}_\perp)$ can be related to the coordinates (μ, θ, φ) by

$$x = \frac{1}{2}\left(1 + \frac{\mu \cos\theta}{\sqrt{m_\ell^2 + \mu^2}}\right), \tag{E.4}$$

$$\boldsymbol{k}_\perp = (\mu \sin\theta \cos\varphi, \mu \sin\theta \sin\varphi). \tag{E.5}$$

The inverse relations can be trivially derived from these, giving

$$\mu = \sqrt{\frac{k_\perp^2 + m_\ell^2(2x-1)^2}{1 - (2x-1)^2}}, \tag{E.6}$$

$$\cos\theta = (1 - 2x)\sqrt{\frac{k_\perp^2 + m_\ell^2}{k_\perp^2 + m_\ell^2(2x-1)^2}}. \tag{E.7}$$

With these new coordinates, it is necessary to have the Jacobian between them and the original coordinates,

$$J(\mu, \theta, \varphi) = \frac{1}{2}\frac{m_\ell^2 + \mu^2(1 - \cos^2\theta)}{(m_\ell^2 + \mu^2)^{3/2}}\mu^2 \sin\theta. \tag{E.8}$$

The integration measure for the effective integral is then

$$\int_1^0 \mathrm{d}x \int_{-\infty}^{+\infty} \mathrm{d}^2 k_\perp = \int_0^{2\pi} \mathrm{d}\varphi \int_0^{+\infty} \mathrm{d}\mu \int_{-1}^{1} \mathrm{d}\cos\theta \frac{\mu^2}{2}\frac{m_\ell^2 + \mu^2(1 - \cos^2\theta)}{(m_\ell^2 + \mu^2)^{3/2}}. \tag{E.9}$$

Physical intuition for μ can be developed by thinking of it as an *off-shell mass* of the particle-antiparticle state. This can be seen from the relation

$$\sum_i p_i^- = \frac{m_\ell^2 + k_\perp^2}{x} + \frac{m_\ell^2 + (-k_\perp)^2}{1 - x} = \frac{m_\ell^2 + k_\perp^2}{x(1-x)} = 4(m_\ell^2 + \mu^2) \tag{E.10}$$

Discretization Methods

In order improve the efficiency of his eigenvalue solver Mesonix, Trittmann[1] choses instead of using a uniform grid in μ, θ to discretize via Gauss-Legendre polynomials, since the wave functions should be better represented by this basis. This allowed him to use a smaller number of discrete points and therefore better leverage the computational resource he had on hand. For TMSWIFT, the discretization routines have been generalized, allowing for flexibility in choosing the scheme. In addition to Trittmann's use of Gauss-Legendre, TMSWIFT has implemented the capacity to solve for a uniform grid (but it isn't recommended), as well as the Clenshaw-Curtis method, the Gauss-Chebyshev-of-the-first-kind method, and the Gauss-Laguerre method. Each of these methods chooses the discrete points based on the optimal representation for a given polynomial basis.

The reason for this multiplicity of options is two-fold. First, even with the parallel implementation of TMSWIFT, the full problem of light-front quantum field theory is prohibitively complicated, and therefore investigations of optimal basis sets should be undertaken. In fact, this is the entire premise of the BLFQ techniques being developed: that a smart choice of basis states may dramatically improve the tractability of the the bound-state problem. Secondly, in order to correctly account for the continuum states of $|e^+e^-\rangle$ that mix with the true muonium bound states, sampling needs to be done on highly localized states. A portion of this thesis was devoted to determining how these states could be sampled accurately. It was found that using a method like Clenshaw-Curtis, which reuses some points from lower N discretizations in larger N ones, allows one to discriminate between actual physical effects of these states and numerical artifacts.

The techniques all have a similar structure for how they are implemented. For a given set of basis functions, an integral is approximated by

$$\int_a^b \mathrm{d}x f(x) = \int_a^b \mathrm{d}x w(x) g(x) \approx \sum_i w_i g(x_i), \tag{E.11}$$

where the points x_i are selected to optimize some criteria. For most cases they are the roots of the basis polynomial and are optimized to reduce the numerical error over a class of functions most rapidly. In addition to the numerical integration, it is necessary to remap the coordinates. The reason for this is that the domain of $\mu = (0, \Lambda \to \infty)$. To make this semi-infinite range tractable, the mapping function $f(\mu)$ is introduced such that

$$f(\mu) = \frac{1}{1 + \mu} \tag{E.12}$$

Restoring the Symmetries

In the previous sections, it was explained how numerically it is more efficent to use the coordinates $(\mu, \cos(\theta))$. Unfortunately, this initial numerical improvement in performing the necessary integrals is essentially wiped out in a naive implementation. This is because the effective Hamiltonian is no longer symmetric in the new variables, and the computational efficiency for solving eigenvalue problems for unsymmetric

matrices is dramatically worse. To repair this deficiency, a redefinition of the wave function that is used in TMSWIFT is necessary. First, in discrete variables, the Jacobian can be expressed as

$$J_{ij} = \frac{1}{2} \frac{m_\ell^2 + \mu_i^2(1 - \cos^2 \theta_j)}{(m_\ell^2 + \mu_i^2)^{3/2}} \mu_i^2 \sin \theta_j. \tag{E.13}$$

Further, because discrete points chosen are not uniform but instead fixed by a Gauss quadrature, there is a weight function w_i or w_j associated with the coordinates. Using these factors together, one defines a wave function

$$\phi(\mu_i, \theta_j) = \sqrt{w_i w_j J_{ij}} \psi(\mu_i, \theta_j), \tag{E.14}$$

where throughout TMSWIFT this asymmetry-fixing term is a vector `asy[]`. This modification can be used to express the effective, discretized integral equation in the form:

$$[4(m_\ell^2 + \mu_i^2) - M_n^2] \frac{\phi(\mu_i, \theta_j, \lambda_1, \lambda_2)}{\sqrt{w_i w_j J_{ij}}} =$$
$$- \frac{g^2}{16\pi^3} \sum_{\lambda_3, \lambda_4} \sum_{k,l} w_k w_l J_{kl} \langle i, j, 1, 2 | V | k, l, 3, 4 \rangle \frac{\phi(\mu_k, \theta_l, \lambda_3, \lambda_4)}{\sqrt{w_k w_l J_{kl}}}. \tag{E.15}$$

Performing a minor amount of algebra, this expression can be put into a manifestly symmetric form:

$$[4(m_\ell^2 + \mu_i^2) - M_n^2] \phi(\mu_i, \theta_j, \lambda_1, \lambda_2) =$$
$$- \frac{g^2}{16\pi^3} \sum_{\lambda_3, \lambda_4} \sum_{k,l} \sqrt{w_i w_j w_k w_l J_{kl} J_{ij}} \langle i, j, 1, 2 | V | k, l, 3, 4 \rangle \phi(\mu_k, \theta_l, \lambda_3, \lambda_4). \tag{E.16}$$

Using the Coulomb Trick

In attempting to treat the bound-state problem of Yukawa theories, QED, QCD, and many others, there is an inherently difficult numerical problem that must be addressed. This problem even surfaces in simple, non-relativistic, instant-form problems. The problem is singularities. To be specific, it is good to consider the example of the Coulomb-Schrödinger equation and its integrable singularity (especially since the light-front effective Hamiltonian can be shown to have this equation as the non-relativistic limit, as shown by [163]). While analytical methods have no problem with solving problems with integrable singularities, when a numerical method tries to sample integration points approaching the singularity, it will often fail because the exact point of the singularity can't be represented numerically.

To avoid this issue, Wölz developed the so-called Coulomb trick[162]. In the numerical methods and mathematics community, the generalized idea of this method is called the Nyström method[248]. In this section, the S-wave hydrogen atom in

momentum representation and how the problem of integrable singularities can be solved will be discussed, this is the problem first tackled by Wölz in his thesis. For this problem, the Schrödinger equation is given by

$$\left(\frac{\boldsymbol{p}^2}{2m} - E\right)\psi(\boldsymbol{p}) = \frac{\alpha}{2\pi^2}\int \mathrm{d}^3\boldsymbol{p}' \frac{\psi(\boldsymbol{p}')}{(\boldsymbol{p} - \boldsymbol{p}')^2}. \tag{E.17}$$

By considering only the S-wave states, the rotational invariance is manifest in each state. This makes it trivial to integrate the angular variables to arrive at the Hamiltonian equation with a single degree of freedom, p:

$$\left(\frac{p^2}{2m} - E\right)\psi(p) = \frac{\alpha}{\pi}\int \mathrm{d}p' \frac{p'}{p}\ln\left(\frac{(p - p')^2}{(p + p')^2}\right)\psi(p'). \tag{E.18}$$

Discretizing this equation with a particular choice of approximation exchanges the single integral for a weighted sum, i.e.,

$$\left(\frac{p_i^2}{2m} - E\right)\psi(p_i) = \frac{\alpha}{\pi}\sum_j^N w_j \frac{p_j}{p_i}\ln\left(\frac{(p_i - p_j)^2}{(p_i + p_j)^2}\right)\psi(p_j). \tag{E.19}$$

While analytically it is possible to solve this equation exactly, the numerical solution will find difficulty around the singularity $p_i = p_j$. The crux of the Coulomb trick is to add and subtract a term that in the continuum limit is the same, one that is discrete and one that is analytical:

$$\left(\frac{p_i^2}{2m} - E\right)\psi(p_i) = \frac{\alpha}{\pi}\sum_j^N w_j \frac{p_j}{p_i}\ln\left(\frac{(p_i - p_j)^2}{(p_i + p_j)^2}\right)[\psi(p_j) - g(p_i, p_j)\psi(p_i)]$$

$$+ \frac{\alpha}{\pi}\int \mathrm{d}p' \frac{p'}{p_i}\ln\left(\frac{(p_i - p')^2}{(p_i + p')^2}\right)g(p_i, p')\psi(p_i) \tag{E.20}$$

where essentially any function form of $g(p_i, p_j)$ can be chosen as long as it satisfies the constraint of $g(p_i, p_i) = 1$. This constraint ensures that the numerical and analytical expressions are the same in the limit $N \to \infty$. With this expression, the numerical issues from the diagonal $p_i = p_j$ has been moved to a continuum problem. In his thesis, Wölz found that if the ground state is desired, then an acceptable functional form of $g(p_i, p_j)$ is

$$g(p_i, p_j) = \frac{(1 + p^2)^2}{(1 + (p')^2)^2}. \tag{E.21}$$

For this particular choice, the analytical integral can be performed, yielding $-\alpha\pi(1 + p_i)$. As was found by Trittmann[1], this method can still work for the full effective Hamiltonian. The complications arise in that, even for simple forms of $g(p_i, p_j)$, the analytical integral cannot be obtained. Instead, this integral, which for a judicious choice of $g(p_i, p_j)$ will still soften the singularity, is treated numerically, but with specialized integrators using much higher precision only over a small range around the singularity. In TMSWIFT, this procedure is included in the files `coulomb_cont.cpp` and `coulomb_discrete.cpp` for the exchange interactions. In the annihilation channel, there is no concern for singularities and therefore there is no need for implementation.

APPENDIX F

EFFECTIVE INTERACTIONS

As explained in Chapter 2, the infinite Fock space must be truncated in order to make the problem tractable. In this appendix, the method of iterated resolvents will be described. This method allows for the reduction of the effective degrees of freedom in the Hamiltonian at the expense of introducing a redundant parameter, ω.

Method of Iterated Resolvents

Consider a Hamiltonian matrix $H|\Psi\rangle = E|\Psi\rangle$ of size $N \times N$. The rows and columns of this matrix can be decomposed with a pair of projection operators, $P = \sum_j^n |j\rangle\langle j|$ with $1 < n < N$, and $Q = 1 - P$. With these, the Hamiltonian can be rewritten in terms of block matrices:

$$\begin{pmatrix} \langle P|H|P\rangle & \langle P|H|Q\rangle \\ \langle Q|H|P\rangle & \langle Q|H|Q\rangle \end{pmatrix} = \begin{pmatrix} \langle P|\Psi\rangle \\ \langle Q|\Psi\rangle \end{pmatrix} = E \begin{pmatrix} \langle P|\Psi\rangle \\ \langle Q|\Psi\rangle \end{pmatrix}. \tag{F.1}$$

The second line can algebraically be rewritten as

$$\langle Q|E - H|Q\rangle\langle Q|\Psi\rangle = \langle Q|H|Q\rangle\langle P|\Psi\rangle \tag{F.2}$$

Inverting this equation, it is possible to express the Q sector as a function of the P sector. The difficulty lies in the unknown values of E. To move beyond this, the redundant parameter ω is introduced. For any value of ω, the equation can then be solved, but only when imposing the additional constraint of $E(\omega) = \omega$ are the values $E(\omega)$ actually the true eigenvalues. With ω, one can define the propagator, or resolvent, of the Q-space:

$$G_Q(\omega) = \frac{1}{\langle Q|\omega - H|Q\rangle}. \tag{F.3}$$

Using the resolvent, the entire Hamiltonian can be expressed in only the P-space as

$$\langle P|H_{\text{eff}}(\omega)|P\rangle = \langle P|H|P\rangle + \langle P|H|Q\rangle G_Q(\omega)\langle Q|H|P\rangle. \tag{F.4}$$

With the resolvent introduced, it is possible to approximate it in ways that can simplify the numerics. Consider two resolvents, one with and one without off-diagonal elements in H. To connect with the eventual physical problem, the diagonal terms will suggestively be defined as T and the off-diagonal as V. The two resolvents are

$$G_Q(\omega) = \frac{1}{\langle Q|\omega - T - U|Q\rangle} \quad \text{and} \quad G_0(\omega) = \frac{1}{\langle Q|\omega - T|Q\rangle}. \tag{F.5}$$

Formally, these two are related by

$$\begin{aligned} G_Q(\omega) &= G_0(\omega) + G_0(\omega)UG_Q(\omega) \\ &= G_0(\omega) + G_0(\omega)UG_0(\omega) + G_0(\omega)UG_0(\omega)UG_0(\omega) + \dots. \end{aligned} \tag{F.6}$$

Therefore, it is seen that the full resolvent is an infinite series of free resolvents with U interactions between them. Why is this useful? $G_0(\omega)$ can be trivially inverted since the matrix in the denominator is completely diagonal. The Tamm-Dancoff method corresponds to truncating the series at the first term[249, 250], and is common

in many-body physics. Unfortunately, this truncation generally introduces a severe singularity and in fact the series diverges order by order. Even more problematic is that in a gauge theory, this truncation general breaks gauge invariance.

The formalism developed is trivially expanded to system of n sectors. For the Hamiltonian

$$\sum_i^n \langle i|H_n(\omega)|j\rangle\langle j|\Psi(\omega)\rangle = E(\omega)\langle i|\Psi(\omega)\rangle \tag{F.7}$$

the resolvent in each sector can be defined as

$$G_n(\omega) = \frac{1}{\langle n|\omega - H|n\rangle} \tag{F.8}$$

Using these, an effective Hamiltonian in $n-1$ sectors can be written via

$$H_{n-1}(\omega) = H_n(\omega) + H_n(\omega)G_n(\omega)H_n(\omega). \tag{F.9}$$

Recursively applying this mechanism, it is possible to reduce an n-sector bare Hamiltonian to an effective Hamiltonian in any number of fewer sectors, including a single one. The only restriction is that n must be finite. Given a finite initial n, the entire problem is reduced to chains like $HG_iHG_mHG_lH$ (where $i, m, l \leq n$). The total number of resolvents in a particular term is determined by n.

A number of important features should be pointed out about these chains. First, $H_n(\omega)$ never contains a resolvent for the n-sector, therefore the system never falls back into a state of $k < n$ through one of these chains. Another way of phrasing this is that the chains will form Russian nesting doll-like structures, e.g.,

$$H_n(\omega)G_n(\omega)H_{n+1}(\omega)G_{n+1}(\omega)H_{n+2}(\omega)G_{n+2}(\omega)H_{n+2}(\omega)G_{n+1}(\omega)H_{n+1}(\omega)G_n(\omega)H_n(\omega). \tag{F.10}$$

While these chains in a gauge theory might seem daunting, it is important to remember that many interactions $\langle l|H|j\rangle$ in the chain are zero. This sparsity in chains arises from the Hamiltonian operators in QED and QCD only changing particle number by at most 2. Moving beyond these expressions requires some finesse in choosing approximations for ω such that a searching through all values of ω isn't required. How these approximations are made is discussed in Chapter 3.

QED with Iterated Resolvents

For the case of interest in this thesis, the effective $\ell^+\ell^-$ Hamiltonian can be written in a relatively compact form due to the aforementioned limits of Hamiltonian operators,

$$H_{\ell^+\ell^-,\text{eff}} = T_{\ell^+\ell^-} + VG_{\ell^+\ell^-\gamma}V + VG_\gamma V + VG_{\gamma\gamma}VG_{\ell^+\ell^-\gamma}V, \tag{F.11}$$

where it is implied in this equation that for each chain, the corresponding diagonal seagull or fork diagram would also be included. Equation (F.11) is formally correct, independent of the Fock-space truncation. This is because hiding in $G_\gamma, G_{\ell^+\ell^-\gamma}$, and $G_{\gamma\gamma}$ are each another chain of all higher states they are coupled to. These chains will continue to build, including higher and higher Fock states until the highest Fock

state is reached. At that point, the resolvent will contain no off-diagonal elements, and therefore can trivially be solved, ending the chain. One approximation, called *in-medium perturbation theory*, relies upon the notion that in the resolvent, interactions can be split into spectator and non-spectator interactions, as was discussed in Chapter 3. In the same way that G_n is related to G_0, G_n can be related to the spectator interaction-only resolvent $\bar{G}_n$. These resolvents are given by

$$\bar{G}_n = \frac{1}{\omega - T_n - \bar{U}_n}, \quad G_n = \frac{1}{\omega - T_n - \bar{U}_n - \tilde{U}_n}, \qquad (\text{F.12})$$

the splitting into $\bar{U}_n$ and $\tilde{U}_n$ being based on recognizing that not all interaction terms change the Fock state. Unlike the Tamm-Dancoff approximation, which splits all non-diagonal elements off into U, the in-medium idea is to instead split off only those non-*block*-diagonal elements into $\tilde{U}_n$. An example of how this works can be considered in the $\ell^+\ell^-\gamma$ sector. The seagull diagrams between $\ell^+\ell^-$ particles would be considered part of $\bar{U}_{\ell^+\ell^-\gamma}$ since the particle content remains the same. In contrast, the element $VG_{\ell^+\ell^-\ell^+\ell^-}V$, which corresponds to a vacuum polarization correction, would be considered part of $\tilde{U}_n$. In this series expansion of G_n, the divergences are found to be less severe, and for smartly chosen forms of ω can produce reasonable results.